Functional Extensions of Optical Coherence Tomography for Biomedical Imaging Applications

By

Priyanka Sharma

Enrolment No. PHYS03201304001

Raja Ramanna Centre for Advanced Technology,

Indore-452013, India

A thesis submitted to the

Board of Studies in Physical Sciences

In partial fulfillment of requirements

for the Degree of

DOCTOR OF PHILOSOPHY

of

HOMI BHABHA NATIONAL INSTITUTE

August, 2018

Homi Bhabha National Institute

Recommendations of the Viva Voce Committee

As members of the Viva Voce Committee, we certify that we have read the dissertation prepared by Priyanka Sharma entitled "Functional Extensions of Optical Coherence Tomography for Biomedical Imaging Applications" and recommend that it may be accepted as fulfilling the thesis requirement for the award of Degree of Doctor of Philosophy.

For Arup Banerjee Date: 12/02/2019
Chairman: Dr. K. S. Bindra

Date: 12/2/19
Guide/Convener: Dr. K. D. Rao

Date: 12 - Feb - 2019
External Examiner: Dr. R. M. Vasu

Date: 12/02/19
Member (External): Dr. J. T. Andrews

S R Mishra Date: 12/2/19
Member 1: Dr. S. R. Mishra

Date: 12/2/19
Member 2: Dr. S. K. Majumder

Anand Moorti Date: 12/2/19.
Member 3: Dr. A. Moorti

Date: 12/2/19
Member 4: Dr. P. K. Mukhopadhyay Pranab K. Mukherjee

Date: 12/2/19
Member 5: Dr. C. Mukherjee C. Mukherjee

Final approval and acceptance of this thesis is contingent upon the candidate's submission of the final copies of the thesis to HBNI.
I hereby certify that I have read this thesis prepared under my direction and recommend that it may be accepted as fulfilling the thesis requirement.

Date: 12th February, 2019

Place: RRCAT, Indore

Dr. K. D. Rao
Guide

STATEMENT BY AUTHOR

This dissertation has been submitted in partial fulfillment of requirements for an advanced degree at Homi Bhabha National Institute (HBNI) and is deposited in the Library to be made available to borrowers under rules of the HBNI.

Brief quotations from this dissertation are allowable without special permission, provided that accurate acknowledgement of source is made. Requests for permission for extended quotation from or reproduction of this manuscript in whole or in part may be granted by the Competent Authority of HBNI when in his or her judgment the proposed use of the material is in the interests of scholarship. In all other instances, however, permission must be obtained from the author.

Sharma
12.02.19
Priyanka Sharma

DECLARATION

I, hereby declare that the investigation presented in the thesis has been carried out by me. The work is original and has not been submitted earlier as a whole or in part for a degree / diploma at this or any other Institution / University.

Bharma
12.02.19
Priyanka Sharma

List of publications arising from the thesis

Journal

1. "Feasibility of speckle variance OCT for imaging cutaneous microvasculature regeneration during healing of wounds in diabetic mice", **P. Sharma**, J. Kumawat, S. Kumar, K. Sahu, Y. Verma, P. K. Gupta and K. D. Rao, *Laser Physics,* **2018,** 28, 025601.

2. "Noninvasive assessment of cutaneous alterations in mice exposed to whole body gamma irradiation using optical imaging techniques", **P. Sharma**, K. Sahu, P. K. Kushwaha, S. Kumar, M. K. Swami, J. Kumawat, H. S. Patel, S. Kher, P. K. Sahani, G. Haridas and P. K. Gupta, *Lasers in Medical Science,* **2017,** 32, 1535-1544.

3. "Human ex-vivo oral tissue imaging using spectral domain polarization sensitive optical coherence tomography", **P. Sharma**, Y. Verma, K. Sahu, S. Kumar, A. V. Varma, J. Kumawat, P. K. Gupta, *Lasers in Medical Science,* **2017**, 32, 143–150.

4. "Absolute velocity measurement using three-beam spectral-domain Doppler optical coherence tomography", **P. Sharma**, Y. Verma, S. Kumar, P.K. Gupta, *Applied Physics B,* **2015,** 120, 539–543.

5. "Single detector-based absolute velocity measurement using spectral domain Doppler optical coherence tomography", S. Kumar, Y. Verma, **P. Sharma**, R. Shrimali, P. K. Gupta, *Applied Physics B,* **2014**, 117, 395-399.

Conferences

1. "Imaging of cutaneous microvasculature regeneration during healing of wound in diabetic mice using swept source based optical coherence tomography", **P. Sharma,** Y. Verma, K. Sahu, S. Kumar, J. Kumawat, P. K. Gupta, *DAE-BRNS National Laser Symposium (NLS-25), KIIT, Bhubaneswar, December 20-23, 2016.*

2. "Studies on use of optical imaging and spectroscopy for the assessment of cutaneous alterations in mice exposed to whole body gamma irradiation", K. Sahu, **P. Sharma**, M. K. Swami, S. Kumar, J. Kumawat, P. K. Kushwaha, H. S. Patel, S. Kher, M. Sharma, A. Dube, P. K. Gupta, *DAE-BRNS National Laser Symposium (NLS-25), KIIT, Bhubaneswar, December 20-23, 2016.*

3. "Three Dimensional Velocity Vector Measurement Using Three Beam based Spectral Domain Doppler Optical Coherence Tomography", **P. Sharma,** S. Kumar, Y. Verma, P. K. Gupta, *DAE-BRNS National Laser Symposium (NLS-23), Sri Venkateswara University, Tirupati, December 3-6, 2014.*

4. "Imaging of normal and cancerous hamster cheek pouch using polarization sensitive optical coherence tomography", **P. Sharma,** Y. Verma, A. Dube, S. Kumar, P. K.

Gupta, *DAE-BRNS National Laser Symposium (NLS-22), Manipal University, Manipal, January 8-11, 2014.*

5. "Dual beam based absolute velocity measurement using single detector spectral domain Doppler optical coherence tomography", S. Kumar, Y. Verma, **P. Sharma**, R. Shrimali, P. K. Gupta, *DAE-BRNS National Laser Symposium (NLS-22), Manipal University, Manipal, January 8-11, 2014.*

P Sharma
12.02.19
Priyanka Sharma

I dedicate this work to

my Parents

"Radhe-Krishna"

ACKNOWLEDGEMENTS

I would like to take this opportunity to express my sincere thanks to all those who have helped me with various aspects of my PhD research.

First of all, I would like to express my profound gratitude to my guide Dr. K. D. Rao for his guidance and valuable suggestions. I am grateful to him for critically reviewing this thesis. I am grateful to the doctoral committee members Prof. K. S. Bindra, Prof. S.R. Mishra, Prof. S.K. Majumder, Prof. A. Moorti, Prof. P.K. Mukhopadhyay and Prof. C. Mukherjee for their time, encouragement and insightful comments.

I would also like to thank my ex-guide Dr. P. K. Gupta and the members of previous doctoral committee Dr. D.K. Palit, Dr. I. Priyadarshini, Dr. N. K. Sahoo, Dr. A. Dube, Dr. K. Das and Dr. Ramachari for their time, encouragement and insightful comments.

My sincere thanks to my division head Shri A. S. Joshi and my lab head Dr.Sendhil Raja S. for always helping and motivating me. Their support and encouragement has been instrumental in completion of the PhD work.

I also thank Dr. Yogesh Verma for his suggestions and support in the planning of experiments and analysis of the experimental data.

I also thank Shri H. S. Patel and Dr. M. K. Swami for always being there with their support and guidance. Discussions with them have been really important.

Also, it is my pleasure to express my sincere thanks to my lab members Sh. Sudhir Kumar, Ms. Jyoti Kumawat and Sh.Vishwamitra Sharma for creating pleasant and friendly environment at the workplace and providing me the much needed help and co-operation during all my experiments.

I would also like to thank Dr. K. Sahu for providing biological support and active participation in some of the the works discussed herein.

I also take this opportunity to thank Smt. Sunita Ahlawat, Sh. R. S. Verma and Pankaj Kushwaha for their help and support.

Thanks are also due to Sh. Anupam Chowdhury and Sh. Nitin Kumar for their help and participation.

I would also like to thank Dr. Jogy George and Sh. Sudhir Kumar for proof reading the thesis and their valuable comments.

I would also like to acknowledge all those associated directly or indirectly; association and timely help from them has benefited me in one way or the other.

A special thanks to my family - the ultimate support system and driving force for me. Words cannot express my special gratitude to my parents for their love and endless support to help me reach this point; my loving husband Rajesh for his selfless love, understanding and encouragement; my doting in-laws; my nephews and niece for being the joy of my life; and my brother and sister for their constant care and moral support.

Last and certainly not least, I thank God, the Almighty for providing me this beautiful life and giving me the opportunity and capability to proceed successfully.

Table of Contents

Homi Bhabha National Institute

SYNOPSIS OF Ph. D. THESIS

1. **Name of the Student: Priyanka Sharma**
2. **Name of the Constituent Institution: Raja Ramanna Centre for Advanced Technology**
3. **Enrolment No. : PHYS03201304001 dated 01.09.2013**
4. **Title of the Thesis: Functional extensions of Optical Coherence Tomography for biomedical imaging applications**
5. **Board of Studies: Physical Sciences**

Synopsis

Image guided diagnosis forms an important part of modern health care practice. The current frontline imaging techniques like X-ray, ultrasound, MRI, etc have led to a phenomenal improvement in patient health care but these also have some drawbacks like use of ionizing radiation, relatively poor resolution, high cost of the equipment, etc. In the past decades, optical imaging techniques have attracted a lot of research interest as these can address some of these limitations. However, while optical imaging can be performed with ease for thin samples such as cell culture and thin tissue sections, multiple scattering of light, arising due to the spatial fluctuation of refractive index in the tissue, poses a major challenge for thick biological turbid tissues. Several approaches can be used to filter out the image corrupting multiple scattered photons. These include time gating, polarization gating and/or coherence gating techniques [1]. Coherence of the light is a

property which gets altered due to multiple scattering and after a few scattering events, the scattered photon can no longer interfere with the unscattered photons. Optical coherence tomography is one of the most successful implementation of coherence gating and has grown tremendously since its inception in 1990's. Optical Coherence Tomography (OCT) is a low coherence interferometry based non-invasive non-contact biomedical imaging modality which can provide real time, depth resolved 3D imaging of tissue morphology with resolution of few micrometers [2,3]. Owing to its attractive features, OCT has found widespread applications in ophthalmology, dermatology, dentistry, cardiovascular imaging, etc. While the first generation OCT systems were time domain in nature and required relatively larger imaging time, the advancements in source and detector technology have made possible the development of second generation Fourier domain OCT (FDOCT) systems that offer improved sensitivity and greater imaging speed over the time domain setups [4,5]. FDOCT is implemented in two ways: spectral domain OCT (SDOCT) where a broadband source is used and the interferogram is spectrally dispersed on a linear detector array, and a Swept Source based OCT (SSOCT) where a rapidly tunable swept source is used and the interference fringes are detected by a photodetector.

Conventional OCT systems exploit the intrinsic variation in tissue refractive index to distinguish various tissue microstructures and generate a depth resolved image of tissue reflectivity. In early stage of disease, differences between scattering from normal and diseased tissue are subtle. Moreover two tissues differing in their type or pathology may also have similar scattering properties. Similar to the histological examination where different stains are used to highlight different features, other tissue properties like flow, polarization altering properties, mechanical properties, presence of wavelength dependent scattering and/or absorption can be exploited for enhancing image contrast in OCT. This additional contrast can help in better differentiation of tissue types/pathology. Several

functional extensions of OCT have been developed to provide insight on the physiological information of tissue in addition to morphological information. Polarization sensitive OCT, Doppler OCT, elastographic OCT and spectroscopic OCT are some major functional extensions that allow monitoring of tissue properties like birefringence, blood flow velocity, elasticity, wavelength dependent scattering and absorption [6-10]. The additional information provided by these functional variants of OCT may be intimately related to functional disturbances, which usually precede morphological changes and could be useful for early diagnosis of diseases.

Polarization sensitive OCT is an important and widely used functional variant of OCT that provides additional contrast and specificity in identifying various tissues by measuring the change in polarization state of backreflected light. Depolarization, diattenuation, optical activity and retardance are the important phenomena that can change the polarization of light. While the multiple scattered photons (which cause depolarization) lose their coherence and are hence filtered out by OCT, the effect of optically active tissue components, if any, gets cancelled because of the round trip propagation. Further, the effect of diattenuation and optical rotation are very small for biological tissues and hence can be ignored. Therefore, in biological tissues, birefringence is the main tissue property that leads to change in polarization of light. There are several biological tissues like tendon, muscle, bone, teeth, cartilage, etc that exhibit birefringence. PSOCT has found many important applications like monitoring of wound healing, detection of cancer, estimation of burn depth and detection of caries.

Doppler OCT is another important functional extension of OCT that allows simultaneous imaging of tissue morphology and microcirculation with high resolution in a depth resolved manner. DOCT has the potential to be used for early diagnosis and proper management of several conditions like cancer, diabetic retinopathy, wounds and burn injury where the blood flow and/or vasculature is modified. The existing microcirculation

imaging techniques like Doppler ultrasound, positron emission tomography, magnetic resonance imaging, video capillaroscopy, laser Doppler imaging, etc are limited by their respective parameters like quantification of flow rates, capability of depth sectioning, spatial and temporal resolution, use of externally injected drugs to generate flow contrast, etc. DOCT has been successful in overcoming the limitations of these existing microcirculation imaging techniques. While DOCT can also be used to generate microvascular maps, its dependence on Doppler angle and the high sensitivity of phase measurements to tissue motion results in incomplete noisy microvascular maps. Intensity based approaches like speckle variance OCT can be used to retrieve microvascular arrangement in tissue by utilizing the temporal fluctuations in the intensity of backsacttered light.

In this thesis we describe the development of various functional OCT setups (polarization sensitive OCT, Doppler OCT and speckle variance OCT setup) and their utilization for important biomedical imaging applications such as differentiation of oral cancerous tissue from adjoining normal tissue, monitoring radiation exposure induced cutaneous alterations, measurement of absolute flow velocity using multi-beam approaches and monitoring cutaneous microvasculature regeneration during healing of wound in diabetic mice.

The thesis is organized as follows:

In **Chapter 1**, we provide a brief introduction to optical coherence tomography and discuss the various aspects of an OCT system like resolution, sensitivity, etc. We then present the time and frequency domain implementations of OCT system. Some applications of OCT are also presented. We then discuss the major functional variants of OCT and their principles. Some important applications of these functional extensions are also discussed.

In **Chapter 2**, we describe the development and utilization of spectral domain polarization sensitive OCT setup. Polarization Sensitive OCT (PSOCT) system requires measurement on the orthogonally polarized components of back scattered light to generate high resolution (~ a few μm) depth resolved retardation images of tissue. For *in-vivo* polarization sensitive imaging applications, it is desirable to acquire both the orthogonal polarization components (OPCs) simultaneously. The easiest approach to realize this is to make use of two spectrometers, one for each OPC. This however not only increases the size and the cost of the system, but also leads to depth dependent sensitivity profiles that are independent and un-identical for the two OPCs. Another approach explored is by detecting OPCs of the back scattered light either on adjacent halves of a single line scan camera or by implementing the depth encoding using dual reference arms. These single detector based approaches result in a reduction in the maximum imaging depth range by a factor of two. We have come up with a novel approach of single detector based PSOCT scheme that uses a dual reference arm along with phase shifting for simultaneous detection of OPCs without compromising on the depth range. The details of the system and its working are described in this chapter. *Ex-vivo* imaging of human oral tissue and monitoring of the transformation of oral cavity tissue from normal towards cancer was carried out using this system. While the epithelium thickness was measured to be ~ 100 μm for the normal tissue, it could not be measured for squamous cell carcinoma (SCC) tissues as there was a complete loss of distinction between the epithelium and lamina propia layers. It should be noted that while there is a reduction in the decay constant by a factor of 1.3 for an SCC tissue as compared to normal tissue, the birefringence is reduced by a factor of 5. These results suggest that monitoring of tissue retardance can help in better differentiation of normal and cancerous oral tissue sites. These results are important considering the fact that while the five year survival rate for

early stage oral cancer is more than 80%, it drops to about 20 % in late stage disease, clearly emphasizing the need for early diagnosis.

In addition to the retardance measurements, monitoring blood flow can also serve as important indicator to assess progression or healing of diseased condition, and to assess the effect of medical or surgical intervention in clinical trials. In **Chapter 3**, we describe the development of Doppler OCT setups that could be used for flow imaging. We earlier developed a single-beam phase-resolved Doppler OCT system that provides only the axial velocity component along the probe beam. Therefore, in order to get absolute velocity using such a setup, one requires prior information on the angle between the flow direction and the incident beam (Doppler angle). Retrieval of absolute flow velocity without prior knowledge or computation of Doppler angle requires simultaneous probing of the same spatial location in the sample with multiple beams with different incidence angles. However, increasing the number of probe beams generates additional cross-talk images which makes it difficult to accommodate several images within the limited imaging depth range of spectral domain system. A possible approach for avoiding the cross-talk images is to make use of separate interferometers and spectrometers for the different probe beams. However this makes the system complex, sensitive to misalignment and increases the cost. With a view to develop three beam DOCT setup that allows unambiguous determination of flow velocity, we first developed a dual beam DOCT setup which makes use of a beam displacer to provide two orthogonal linearly polarized beams that probe the sample simultaneously at two different incidence angles. The approach helps remove the cross-talk image and facilitates single detector-based spectral domain velocity measurement. After successfully demonstrating velocity measurements in a flow phantom, the setup was suitably modified for three beam based velocity measurements. Along with the use of beam displacer for removal of cross-talk image, the modified scheme uses galvoscanner based phase shifting for removal of

complex conjugate mirror artifact. This scheme allows efficient utilization of the sensitivity and imaging range of the spectral domain OCT system. Absolute velocity measurements were demonstrated in a flow phantom using the developed scheme.

In addition to the flow velocity, arrangement of tissue microvasculature is an important parameter for several pathological conditions which involve microvascular alterations. While DOCT can also be used to generate microvascular maps, its dependence on Doppler angle and the high sensitivity of phase measurements to tissue motion results in incomplete noisy microvascular maps. In **Chapter 4**, we discuss the development of swept source based speckle variance OCT system that utilizes the temporal fluctuations in the intensity of backscattered light to image the tissue microvasculature. The insensitivity of this technique to Doppler angle is an added advantage. We also made use of the developed speckle variance OCT setup to monitor cutaneous microvasculature regeneration during healing of wound in diabetic mice. Structural and vascular changes were monitored in a punch wound in the ear pinna of diabetic mice. The results show that the developed SVOCT system can be used to monitor vascular regeneration during wound healing.

In **Chapter 5**, we present our results on the use of optical imaging techniques for non-invasive assessment of cutaneous alterations in mice exposed to whole body gamma irradiation. This work is motivated by the need for development of techniques for rapid non-invasive screening of population exposed to ionizing radiation in case of intentional/accidental leakage of ionizing radiation. The present methods for the detection of cutaneous radiation injury like visual examination, event recall by the subject, numerical dosimetry reconstruction, cytogenetic analysis and quantitative bio-dosimetry are not amenable to rapid screening of population exposed to radiation. We have therefore used optical techniques to monitor radiation exposure induced cutaneous alterations in mice model. While the spectral domain polarization sensitive OCT was used to monitor

changes in retardance in the dorsal skin, speckle variance OCT and cross polarization imaging setups were used to monitor microvascular alterations in the mice ear pinna. Radiation dose dependent changes were observed in tissue retardance and microvasculature as early as 1hr post radiation exposure. These results suggest that optical techniques may provide a useful tool for early and non-invasive screening of population exposed to radiation.

Chapter 6 presents a summary of the findings of this research along with a brief discussion on the future scope of work.

References

1. C Dunsby and P M W French, “Techniques for depth-resolved imaging through turbid media including coherence-gated imaging,” J. Phys. D: Appl. Phys. 36, R207–R227 (2003).

2. D. Huang, E.A. Swanson, C.P. Lin, J.S. Schuman, W.G. Stinson, W. Chang, M.R. Hee, T. Flotte, K. Gregory, C.A. Puliafito, and J.G. Fujimoto, "Optical coherence tomography," Science 254, 1178-1181 (1991).

3. James Fujimoto and Eric Swanson, "The Development, Commercialization, and Impact of Optical Coherence Tomography," Investigative Ophthalmology & Visual Science 57, OCT1-OCT13 (2016).

4. R. Leitgeb, C. K. Hitzenberger, and A. F. Fercher, “Performance of Fourier domain vs. time domain optical coherence tomography,” Opt. Express 11, 889-894 (2003).

5. J. F. de Boer, B. Cense, B.H. Park, M. C. Pierce, G. J. Tearney, and B. E. Bouma, “Improved signal-to-noise ratio in spectral-domain compared with time-domain optical coherence tomography,” Opt. Lett. 28, 2067-2069 (2003).

6. Christoph K. Hitzenberger, Erich Götzinger, Markus Sticker, Michael Pircher and Adolf F. Fercher, “Measurement and imaging of birefringence and optic axis orientation by phase resolved polarization sensitive optical coherence tomography,” Opt. Express 9, 780-790 (2001).

7. Z. Chen, T. E. Milner, D. Dave, and J. S. Nelson, “Optical Doppler tomographic imaging of fluid flow velocity in highly scattering media,” Opt. Lett. 22(1), 64–66 (1997).

8. Y. Zhao, Z. Chen, C. Saxer, S. Xiang, J. F. de Boer, and J. S. Nelson, “Phase-resolved optical coherence tomography and optical Doppler tomography for imaging blood flow in human skin with fast scanning speed and high velocity sensitivity,” Opt. Lett. 25(2), 114–116 (2000).

9. Shang Wang and Kirill V. Larin, “Optical coherence elastography for tissue characterization: a review,” J. Biophotonics 8, 279–302 (2015).

10. U. Morgner, W. Drexler, F.C. Kartner, X.D. Li, C. Pitris, E.P. Ippen, and J.G. Fujimoto, "Spectroscopic optical coherence tomography," Opt. Lett. 25, 111-113 (2000).

List of figures

Chapter 1

Introduction to Optical Coherence Tomography and its Functional Extensions

In this chapter, we provide a brief introduction to Optical Coherence Tomography (OCT) and discuss the various aspects of an OCT system like resolution, sensitivity, etc. We then discuss the time and frequency domain implementations of OCT system followed by some applications of OCT. Standard OCT systems exploit the intrinsic variation in tissue refractive index to distinguish various tissue microstructures and provide a depth resolved image of tissue reflectivity. Several functional extensions of OCT systems such as polarization sensitive OCT, Doppler OCT, spectroscopic OCT, etc have been developed to provide functional information like birefringence, flow velocity and molecular information of the tissue. In the later part of this chapter, we discuss the major functional extensions of OCT, their principles and their applications.

1.1 Introduction

OCT is a low coherence interferometric technique that is capable of providing depth resolved, real time, high resolution, cross-sectional images of tissue microstructure in a non-invasive and non-contact way [1-3]. OCT is an optical analogue of ultrasound that uses light instead of sound to produce images with resolution over one to two orders of magnitude higher than that of ultrasound. It fills a valuable niche between confocal microscopy and ultrasound, allowing high resolution (~ few micrometers) imaging with imaging depth of ~ 1-2 mm sufficient for many applications [4]. OCT functions as an optical biopsy in the sense that it provides real time information on tissue pathology without the need of tissue contact, tissue excision or tissue processing. As we will see in the later part of this chapter, OCT has been widely used for biomedical imaging applications in the fields of ophthalmology, cardiology, dentistry, etc, and also for non-medical applications like material science and art conservation.

1.2 Principle

OCT relies on low coherence interferometric detection of light backscattered from tissue microstructures. Fig. 1.1 (A) shows a schematic of OCT setup. Typically, it employs a Michelson interferometer where the light from a broadband source (usually a superluminescent diode (SLD)) is split into two arms namely reference arm and sample arm. The reference arm consists of a perfectly reflecting mirror mounted on a translation stage. The sample am comprises of beam steering optics, focusing lens and a sample stage. The light backreflected from the sample and reference arm recombine at the detector to generate interferometric fringes.

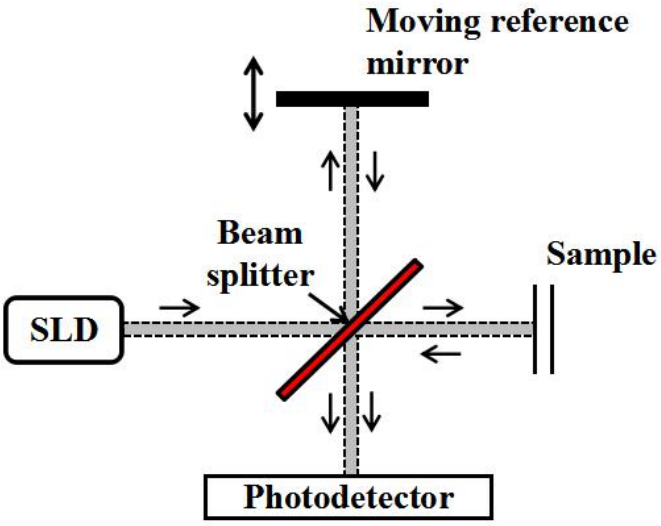

Figure 1.1 (A) *Typical schematic of OCT. SLD: Superluminescent diode.*

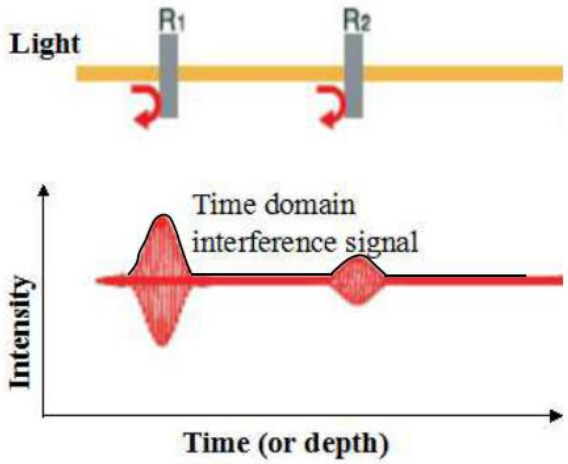

Figure 1.1 (B) *A typical OCT interferogram for the two layered sample shown above; black curve is the envelope of the interferogram.*

Interference occurs only when the optical path difference between the two arms of the interferometer is within the coherence length of the source. Therefore the depth resolution is determined by the coherence length of the source, which is ~ 5-20 μm for the broadband sources employed in OCT. Since the light is backscattered from the sample at each refractive index discontinuity, translation of the reference mirror will allow

observing interference for all these layers, as shown in Fig. 1.1 (B). The detected signal is passed to a lock-in amplifier for envelope detection. Fig. 1.2 shows the image generation procedure in OCT. As shown in Fig. 1.2 (left), the demodulated signal for the entire depth is called an axial scan (or A-scan) where the temporal position determines its location inside the sample and the amplitude determines its reflectivity [1,4]. Taking A-scans at multiple lateral locations results in a two dimensional cross-sectional image, also known as B-scan, as shown in Fig. 1.2 (right). Taking multiple B-frames at adjacent locations results in a three dimensional data.

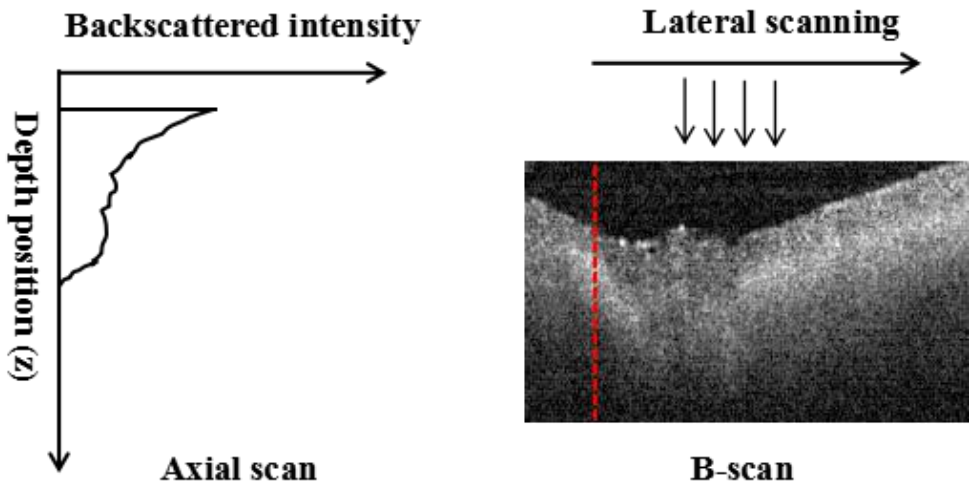

Figure 1.2 *Image generation in OCT. (Left) Axial scan along the red dashed line; (Right) Axial scans acquired at different lateral points leads to generation of a cross-sectional image, also known as B-scan.*

1.3 Mathematical formulation

Let $E_o = |E_o| e^{j(wt-kz)}$ be the electric field of the source light, and E_R and E_S be the reference and sample arm electric fields respectively. The intensity on the detector at any instant can be denoted as

$$I_D \propto |E_R + E_S|^2$$

$$I_D \propto |E_R|^2 + |E_S|^2 + 2|E_R||E_S|\,\mathrm{Re}[\gamma(\tau)]\cos(\frac{2\pi}{\lambda_0}2z) \qquad \ldots\ldots\ldots\ldots\ldots\ldots\ldots\ldots\ldots\ldots(1.1)$$

where $2z$ is the round trip optical path difference between the two arms of interferometer, λ_o is the central wavelength of source and $\gamma(\tau)$ is the complex degree of coherence of the electric fields. Here, the complex degree of coherence $\gamma(\tau)$ can be defined as the normalized autocorrelation function of the electric field emitted by the light source [5]

$$\gamma(\tau) = \frac{\left\langle E^*(t)E(t+\tau)\right\rangle}{\left\langle E^*(t)E(t)\right\rangle} \quad \text{..........} (1.2)$$

where τ is the time delay between the light reaching the detector and backreflected from the two arms, which in turn depends on the path difference. The degree of coherence defines the temporal delay (or path delay) up to which the two light beams can interfere.

1.4 Parameters of an OCT setup

1.4.1 Resolutions

The resolution with which the depth position of a reflecting interface in the sample can be determined depends on the width of coherence length of the source which in turn is inversely proportional to the spectral width of the source. Therefore the broader the bandwidth of the light source used, smaller is the coherence length and hence better is the axial resolution (Δz = $l_c/2$) of the OCT system. The coherence length (l_c = $c\tau_c$) of the source is defined as the FWHM of the modulus of the complex temporal coherence function and for normalized Gaussian power spectral density it can be defined as

$$l_c = \frac{4\ln 2}{\pi}\frac{\lambda_0^2}{\Delta\lambda} \quad \text{..........} (1.3)$$

where $\Delta\lambda$ is the 3dB spectral bandwidth of the source. The above expression clearly explains the choice of broad bandwidth sources for OCT which provide better axial resolution due to their small coherence lengths.

The lateral resolution (Δx) is determined by the focusing optics used and expressed as [4]

$$\Delta x = \frac{4f\lambda_0}{\pi D} \propto \frac{\lambda_0}{NA} \qquad \text{.....(1.4)}$$

where f is the focal length of the lens used to focus the beam over the sample, NA is the numerical aperture of the lens and D is the diameter of beam falling on the lens. Therefore, choosing higher NA results in better lateral resolution and vice versa. However this leads to a loss in the depth of focus (b) which is defined as $b = 2z_R = \frac{\pi(\Delta x)^2}{2\lambda}$.

Physically depth of focus is the distance over which the beam size becomes √2 times the beam waist. Therefore a trade-off between the lateral resolution and depth of focus exists as is seen from Fig. 1.3. It is also clear that unlike microscopy, axial resolution and lateral resolution are decoupled in OCT which allows high resolution imaging of deep seated sites like eye retina which cannot be reached using high NA beams.

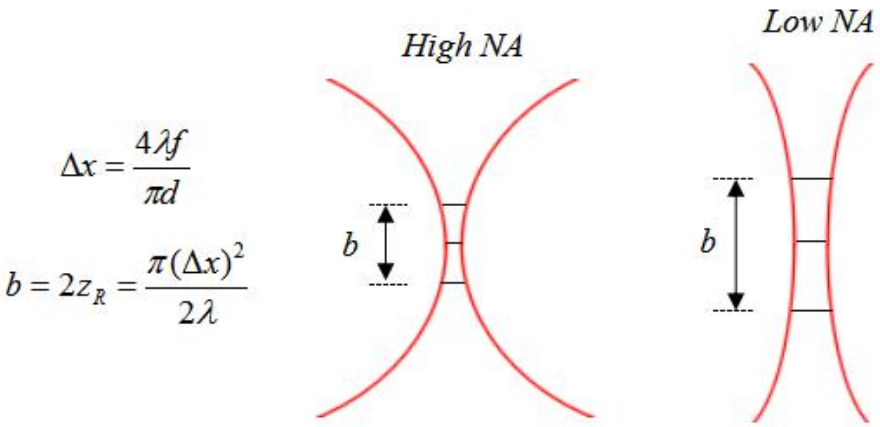

Figure 1.3 *High and low numerical aperture (NA) focusing limits of OCT.*

1.4.2 Imaging speed

This is one of the important parameters for any imaging setup and depends on the OCT configuration being used. The imaging speed is determined by the rate at which the image pixels are acquired. To generate cross-sectional OCT images, a raster scan pattern is used. Here the axial scanning speed (sweep rate) and the number of axial scans required

determine the imaging speed. As will be seen in section 1.5, OCT systems can be implemented in time/Fourier domain. While time domain OCT systems provide scan rates of ~ 1-4 kHz with limited number of A-scans (~ 125) per image, the new Fourier domain OCT (FDOCT) systems are capable of providing 3D imaging (with ~ 500 A-scans per frame) at scan rates ~ 100 kHz [6-11].

1.4.3 Sensitivity

Sensitivity is the parameter which determines the smallest possible signal detecting capability of any system. In OCT the back reflections captured from tissue are generally very weak owing to the minute refractive index variations within the tissue, and the limit of power to be used. However, interferometry enables optical heterodyne gain by multiplying the weak sample electric field with the strong reference arm electric field which results in an increase in the magnitude of the interference term and thereby improves the sensitivity of the detection [4]. Also the scanning reference arm generates a Doppler shift in the reference arm optical frequency which allows electronic filtering of the amplitude of back-scattered light at the Doppler frequency. OCT systems have typical sensitivity of the order of 90-100 dB i.e. signals which are 10^{-9} -10^{-10} times the incident power can also be detected.

1.4.4 Imaging depth

Imaging depth is the maximum depth in the sample from where the backreflections result in an interferometric signal above the noise floor. The scattering and absorption property of the sample and the SNR of the OCT system determine the imaging depth. In the 'biological imaging window' from ~ 800 nm to 1300 nm, tissue absorption is small and the imaging depth is determined primarily by scattering. Also, while whole eye (length ~ 25 mm) can be imaged due to transparency of ocular structures, the imaging depth is limited to a couple of mm for scattering tissues like skin. Since tissue scattering reduces with increasing wavelength, use of source at longer wavelength will lead to larger

imaging depth. Further increase in imaging depth is possible by using optical clearing agents like glycerol and propylene glycol which provide index matching thereby reducing scattering [12-15].

1.5 Time and Fourier domain OCT measurement

As seen from equation 1.1, the interferometric term involves cosine of the product of path difference z and wave vector k ($=2\pi/\lambda_0$). Variation in either z or k will result in amplitude modulations from where the depth information can be retrieved. As seen in Fig. 1.1 (A), the reference mirror is moved at a constant speed in time domain OCT (TDOCT) and the signal is acquired by a photodiode as a function of path delay (or time) [2,4]. While the entire depth is illuminated and light is backreflected from all the layers, the signal in TDOCT is acquired depth section-wise (the width determined by the coherence gate) at a time, and all signal outside this section contributes to background noise. Fig. 1.1 (B) shows a typical interferogram for TDOCT.

An inherent limitation of TDOCT setup is the requirement of moving reference arm for axial scanning that provides the depth resolved reflectivity information of the tissue. Fourier domain OCT (FDOCT) has the advantage that no moving parts are required to obtain axial scans. Also the signal from entire depth contributes to interference signal. Therefore, FDOCT systems have superior performance in terms of imaging speed and sensitivity as compared to the TDOCT systems [16-18]. The reference mirror remains fixed while the detected interferometric signal is dispersed on a spectrometer as shown in Fig. 1.4 (A). The frequency of the interference fringes is directly proportional to the optical path length difference between sample and reference reflections [2,4]. The Fourier transform of the detected intensity spectrum is used to reconstruct the axial profile of the sample as shown in Fig. 1.4 (B). The zero position in Fig. 1.4 (B) (right) corresponds to the path length matched distance between reference and sample arm. The signal appears at both positive and negative frequencies because of the Fast Fourier Transform (FFT) of

real data. This is also known as mirror image or complex conjugate artifact. This ambiguity can be removed by extracting the full complex information of the recorded signal which can be accomplished through different ways [19-22]. Fourier domain systems have been implemented in two ways, namely Spectral Domain OCT (SDOCT) that uses a grating to spatially disperse the spectrum across an array type detector, and swept source OCT (SSOCT) where a narrow band laser is swept across a broad spectrum encoding the spectrum as a function of time [1,23].

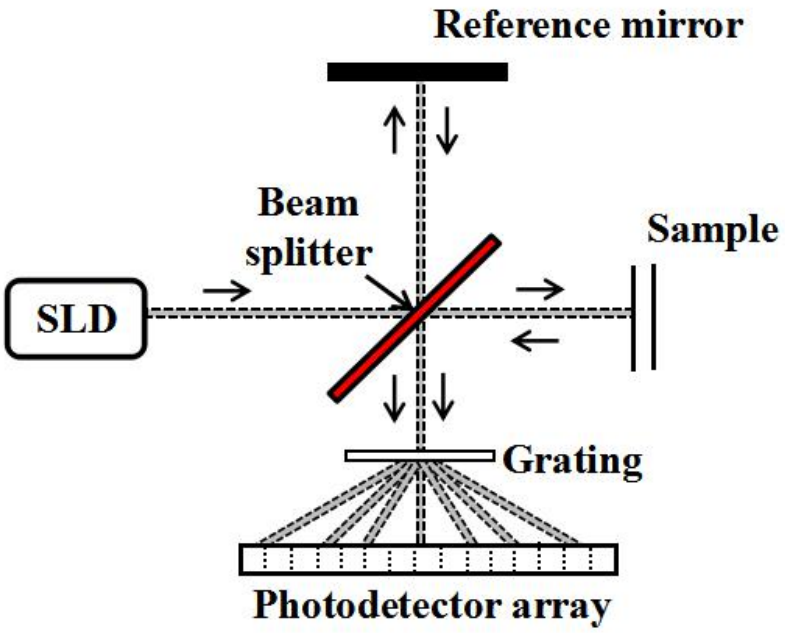

Figure 1.4 (A) *A schematic of Spectral domain OCT. SLD: Superluminescent diode.*

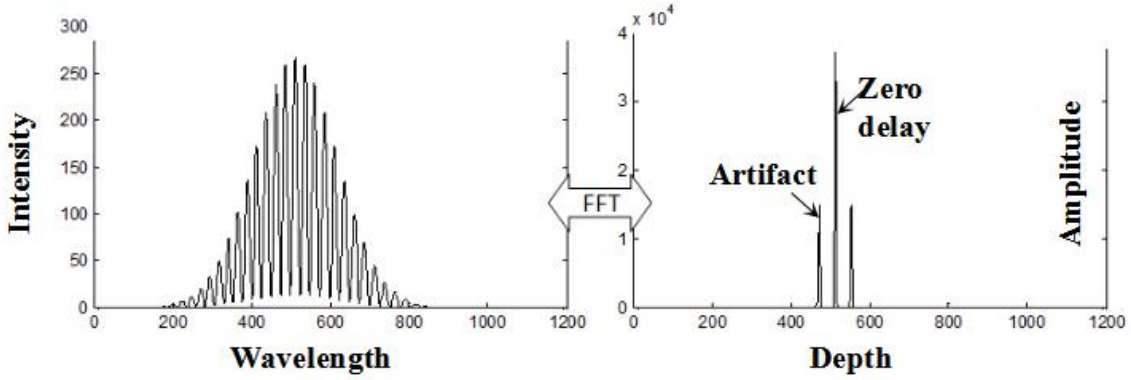

Figure 1.4 (B) *(Left) The spectral intensity as detected at the linear detector array. (Right) The Fourier transform of the spectral intensity pattern gives the depth resolved location of scatterers. The interference at zero delay is the Fourier transform of the source spectrum.*

Fig. 1.5 (A) illustrates a basic SSOCT setup. The source is a tunable laser that sweeps a certain wavelength band. As in TDOCT, light is split by a beam splitter and sent in a sample arm and a reference arm. In the reference arm, the mirror is fixed. In the sample arm, two partial reflectors (blue and red) have been placed. They are located at a distance Δ_1 and Δ_2 from the dotted line. The dotted line represents the zero-delay position; the optical path length from the beam splitter to the dotted line is the same as that from the beam splitter to the mirror. Light reflected by both arms are combined by the beam splitter and sent to the photodetector and an interference phenomenon is observed. It contains a term of the form $\cos(4\pi\Delta/\lambda)$, where λ is the wavelength. As the wavelength is varied (inverse wavelength in the graph of Fig. 1.5 (B)), this term leads to an oscillation. For the blue reflector, the frequency of the oscillation is low. For a reflector located farther from the zero-delay position, like the red one, the frequency of the oscillation is higher. The position of a reflector is encoded in the frequency of the oscillations recorded on the detector as the wavelength is varied. If one takes the Fourier transform of the combined signals from both reflectors, one extracts the position and strength of the

reflectors. Since the information is obtained from the Fourier transform of a real signal, one obtains a mirror image relative to the zero-delay position.

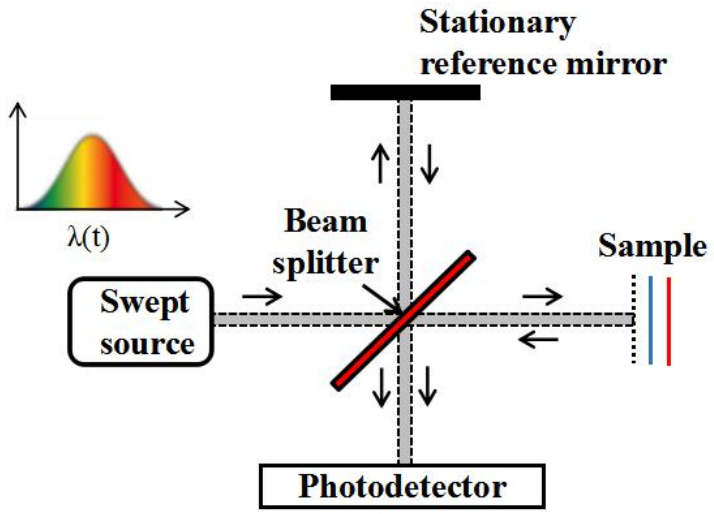

Figure 1.5 (A) *A schematic of Swept source OCT.*

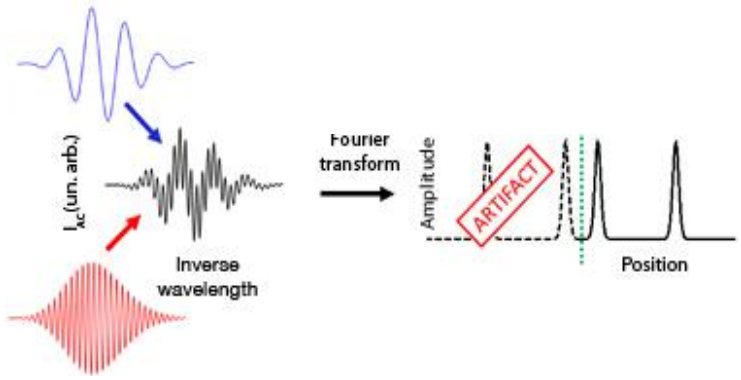

Figure 1.5 (B) *(Left) A typical SSOCT interferogram for a two layered sample shown above; (Right) Fourier transform of the interferogram provides the depth resolved location of scatterers.*

1.6 Applications of OCT

OCT has emerged as a new bio-imaging modality to meet most of the requirements that a modern diagnostic technique should satisfy, such as a large amount of novel diagnostic information, high speed of data acquisition and easy to use device. The noncontact, non-

invasive nature of OCT permits repeatable imaging over extended periods of time at resolutions that approach the level of histology. Due to all these advantages, OCT is promising to find a place in several areas of medical practice [4]. OCT was initially applied for imaging in ophthalmology, and still remains the most widely explored application regime of OCT [24,25]. This is because of the near transparency of the eye coupled with the interferometric sensitivity and precision of OCT. Recently developed ultra high resolution OCT systems provide axial resolution of 1-3μm in non-transparent and transparent media and hence intraretinal subcellular structures can be imaged *in-vivo* [26-28]. This unprecedented visualization of all intra retinal layers provides the ability to assess changes in retinal morphology thereby aiding in better understanding of ocular pathogenesis [29-32]. OCT has also been explored for fields like dentistry, endoscopic applications like cardiovascular imaging, imaging of gastrointestinal tract, etc.

Acquiring excisional biopsy results in creation of wound and poses risk of infection, haemorrhage and even cancer cell spreading. Here optical biopsy comes to rescue as it overcomes all these drawbacks and allows in-situ assessment of tissue, cell functions and morphology. The salient features of OCT like high resolution, high penetration depth, and a potential for functional imaging make it a suitable technique capable of optical biopsy. Development of ultrahigh resolution OCT is a major step towards realizing optical biopsy. High resolution imaging of gastrointestinal (GI) tissues can help delineate tissue at histological level in bulk GI tissue [33-36]. Endoscopic OCT is another important variation which can be used to detect abnormal growth in hollow organs, edema formation and submucosal blood congestion [37,38]. Architectural tissue properties can also be used as tumor screening parameters for identifying pre-malignant tissue states [39-45]. OCT has also been used for understanding coronary plaque and identification of arteriosclerosis [46-48]. OCT has been widely used for dental

applications like diagnosis of periodontal disease, detection of caries, and evaluation of dental restoration and integrity [49-53].

When applied to biomedical scenarios, low-coherence interferometry (LCI) is generally referred to as OCT. Apart from biomedical applications, low-coherence interferometry (LCI) has also been used in optical production technology and other technical fields. It has been used for many years in industrial metrology e.g. as position sensor for the thickness measurement of thin films, and for other measurands that can be converted to a displacement [54-58]. LCI has also been used as a key technology for high-density data storage on multiplayer optical discs and for evaluation of highly scattering polymer-matrix composites [4,59,60]. Non-destructive evaluation of paints and coatings is another promising non-medical OCT application [61-64].

1.7 Functional extensions of OCT

Standard OCT systems exploit the intrinsic variation in tissue refractive index to distinguish various tissue microstructures. These systems provide a depth resolved image of tissue reflectivity. Apart from tissue reflectivity, by measuring change in other parameters of reflected light like phase, polarization, etc, other characteristics of the sample can also be determined. This additional information may provide an insight into functional disturbances, which usually precede morphological changes and could be useful for early diagnosis of diseases. Several versions of OCT systems such as polarization sensitive OCT, Doppler OCT, spectroscopic OCT, elastography OCT, etc. have been developed to provide functional information like birefringence, flow velocity, molecular information of the tissue and stiffness of the tissue sample. In this chapter, we discuss the major functional extensions of OCT, their principles and their applications.

1.7.1 Polarization sensitive optical coherence tomography

Polarization Sensitive Optical Coherence Tomography (PSOCT) gives information about the birefringence of any sample by utilizing the polarization state of light. While

conventional intensity based OCT systems exploit differences in intensity of backscattered light to differentiate between tissue types, PSOCT provides additional contrast and specificity in identifying various tissues by measuring the change in polarization state of backreflected light [65]. There are several biological tissues like tendon, muscle, bone, teeth, cartilage etc that exhibit birefringence. Importance of PSOCT imaging stems from the fact that any change in birefringence could be a potential indicator of change in functionality, structure or tissue viability.

The polarimetric response of a given sample describes how the incident light polarization changes due to the interaction with the sample. This response is a resultant of four fundamental sample properties, namely the diattenuation, retardation, rotation and depolarization. While diattenuator (like linear polarizer) exhibits differential extinction of orthogonal polarization states, most biological tissues do not exhibit diattenuation in the optical window from 800-1300 nm utilized in OCT. A retarder introduces a phase shift between the two orthogonal components. A rotator rotates the plane of polarization without modifying the state of polarization; however its effect cancels in round trip propagation. A depolarizer scrambles the input polarization state i.e. modifies the input polarization in an uncorrelated manner. Basically, scattering and birefringence are the two mechanisms that dominate the change in polarization of light propagating through the tissue. The polarization state of light after a single scattering event depends on the scatterer, orientation of the scatterer and polarization state of incident light. Turbid media such as tissues have a complex distribution of scattering structures with a large variance in their size, shape, orientation and distribution. In turbid medium, each scattering event can modify the incident polarization state differently, and the cumulative effect of multiple scattering events completely randomizes the polarization state of incident light (i.e., uncorrelated with the incident polarization state). In OCT the multiple scattered photons are filtered out by coherence gating hence only single scattering is considered.

Several biological tissues exhibit birefringence due to the presence of organized fibrous structures. The refractive index of a birefringent material is different for light polarized along and perpendicular to its optic axis. The difference of these refractive indices (Δn) induces phase retardation (δ) between orthogonally polarized light components, which can be expressed as

$$\delta = \frac{2\pi x \Delta n}{\lambda} \qquad \text{.....(1.5)}$$

where x is the distance travelled through the birefringent material. Tissue birefringence may originate either from form birefringence or intrinsic birefringence. While form birefringence arises due to arranged linear structures in a tissue matrix with different refractive index, intrinsic birefringence arises due to ordered arrangement of molecules with different optical retardance.

1.7.2 Experimental arrangement for PSOCT

The PSOCT system is similar to that of TDOCT or FDOCT, except that it allows measurements on two orthogonal polarizations of light by incorporation of some polarizing elements like linear polarizer, quarter wave plates and polarizing beam-splitter (PBS). Fig. 1.6 shows a schematic of PSOCT setup. Light from a superluminescent diode is horizontally polarized using a linear polarizer and then split by a non-polarizing beam splitter (NPBS) into two halves, one directed towards the reference arm and the other towards the sample arm. The reference beam passes through a quarter waveplate (QWP) with its fast axis oriented at 22.5° before being reflected by a moving mirror. Hence, in dual passage through the QWP, the reference beam attains circular polarization i.e. contains both vertical and horizontal polarization. In the sample arm, the linear polarized light passes through a QWP with its fast axis oriented at 45° to the incident horizontal polarization to produce circularly polarized light. This is then focussed onto the sample using a focusing lens. In general, the light backreflected from the sample has an arbitrary

(elliptical) polarization state determined by the optical properties of the sample. This light recombines with the H and V polarized components in the reference beam. In the detection arm, a polarizing beam splitter is used to separate the interference signals for the horizontal and vertical components respectively. Had the sample been non-birefringent, the backreflected sample light would have only vertical polarization component and there would be only one interference signal. The interference signals for the two polarization channels are detected by separate photodetectors. The detected interference signals are amplified, band pass filtered and passed to a lock-in amplifier for demodulation of the interferogram. The demodulated signals are digitized with a data acquisition card. After required data processing, images are displayed on personal computer.

The depth resolved reflectivity image can be obtained as $R(z) = A_H(z)^2 + A_V(z)^2$

The phase retardation image can be obtained as $\delta(z) = \arctan\left[A_H(z)/A_V(z)\right]$

The fast axis orientation image can be obtained as $\Phi = \left[\frac{\pi - (\Phi_H - \Phi_V)}{2}\right]$

Here A_H and A_V are the magnitudes of the envelopes of the interferograms corresponding to horizontal and vertical polarizations, and Φ_H and Φ_V are the phase of interference signals in horizontal and vertical polarization. Therefore phase sensitive measurements are required for retrieval of fast axis orientation of the tissue sample [66].

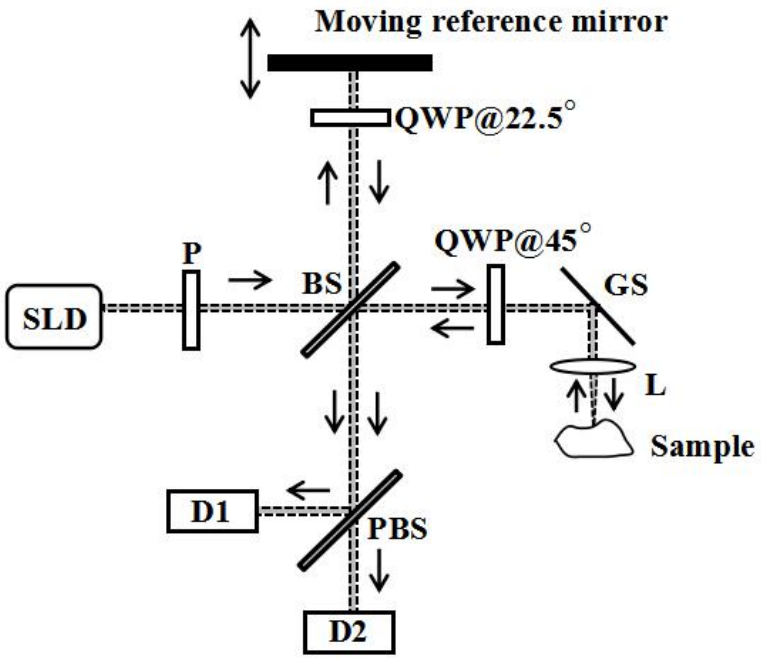

Figure 1.6 *Schematic of PSOCT setup. SLD: Superluminescent diode; D1, D2: Detectors; L: Lens; BS: Beam splitter; PBS: Polarizing beam splitter; P: Polarizer; QWP: Quarter wave plate; GS: Galvoscanner.*

1.7.3 Various schemes in PSOCT

Initial PSOCT setups were developed in free space time domain approach because of the ease of preserving the input polarization is free space geometry [66]. Here circularly polarized light is incident on the sample so that the retardation measurement is insensitive to orientation axis of the sample in the plane perpendicular to incident beam. However, free space setups are sensitive to misalignment and are inconvenient to use for *in-vivo* imaging. Since fiber based setups provide relatively stable alignment and can be coupled to endoscopic probes, they facilitate *in-vivo* applications. Saxer et al first demonstrated the single mode fiber (SMF) based time-domain PSOCT setup [67]. The approach relies on Stokes vector measurement using a polarization modulator to achieve the four polarization states along orthogonal axis of a grand circle in Poincare's sphere.

A major drawback of the time domain OCT setups is that they involve scanning reference arm that limits the imaging speed of the setup and its phase stability. Since Fourier

domain implementation provides increased phase sensitivity and imaging speed, efforts have been made to perform PSOCT measurements in Fourier domain [68]. Fourier domain detection using spectrometer becomes the preferred choice in 800 nm wavelength range owing to the large availability of Si based detectors. The most widely used methodology to perform spectral domain PSOCT measurements involves separation of the two orthogonally polarized components. As will be seen in Chapter 2, several schemes have been developed to accomplish this either by making use of separate spectrometers or by imaging the two orthogonally polarized channels on adjacent halves of a line scan camera [69,70]. However, these schemes suffer from the drawback of either the artifacts in birefringence measurements arising due to the difference in the response function of the two detection channels or a reduction in the imaging depth by a factor of two. We have developed a novel single detector based spectral domain PSOCT setup that allows complex conjugate artifact free single shot measurement of orthogonal polarization channels. Details of this work will be discussed in Chapter 2. For imaging in the 1300 nm wavelength range where low cost CCDs are not readily available to implement spectrograph based detection, use of frequency swept light sources becomes the preferred approach [71]. Another important advantage of swept source OCT systems is that it facilitates the use of balanced detection to minimize the common mode noise and thus reduces the need for high dynamic range A/D conversion. However, swept light sources have large phase jitters which may restrict phase measurements required for the retrieval of sample polarization parameters such as fast axis orientation [72].

Despite the advantages of portability and easy alignment offered by SMF based implementations, polarization mode dispersion (PMD) and other factors like fiber bending, microscopic defects in the fiber and other environmental stresses produce random birefringence changes in SMF which limit the propagation of the desired polarization state of light. Several groups have demonstrated the use of polarization

maintaining fibers that can take care of the PMD effects by isolating the orthogonal polarization states of light for PSOCT measurements [73, 74].

1.7.4 Applications of PSOCT

Since various biological components contain intrinsic and/or form birefringence, PSOCT provides an additional contrast mechanism for identification of structural components. As changes in birefringence may also relate to functional changes in the tissue, PSOCT imaging may also reveal the functional state of tissue. Also it can serve as a useful feedback tool in real-time, laser surgical procedures involving birefringent biological materials. We shall discuss below some major applications of PSOCT.

1.7.4.1 Determination of burn depth

Burn is the injury to the skin and deeper tissues caused by hot liquids, flames, radiant heat, and direct contact with hot solids, caustic chemicals, and electricity. First degree burns are limited to superficial skin (< 100 μm) and are capable of healing spontaneously and hence do not require treatment. A second degree burn shows destruction of the epidermis and partial destruction of the underlying dermis (0.12-2 mm). Third degree burns involve complete destruction of the epidermis and dermis (>2 mm), and need to be grafted. While superficial wounds can be determined using visual inspection, determination of burn as second or third degree by visual inspection is difficult as it requires assessment over several cell layers within the underlying dermis. Studies have shown that the amount of reduction in birefringence can be related to the denaturation in collagen, which can in turn indicate the depth of burn [75]. As is observed from Fig. 1.7, the uniform presence of collagen fibrils in normal skin is lost in burnt skin resulting in reduced birefringence. The loss of collagen birefringence is also reflected in the reduced slope of phase retardation plot for the burn skin.

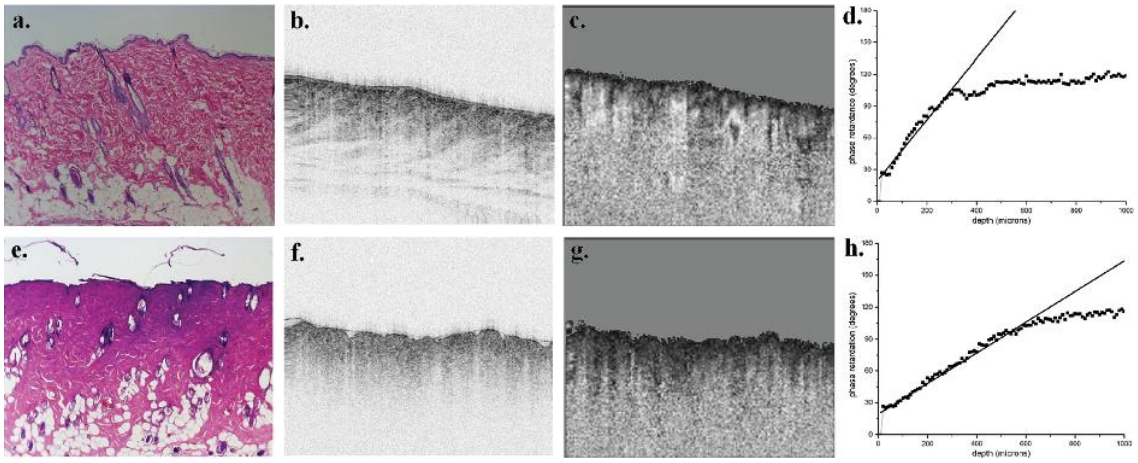

Figure 1.7 *Normal and burned rat skin, respectively, (a, e) histology, (b, f) OCT image, (c, g) phase retardation image, and (d, h) plot of phase retardance versus depth. The thermal injury was for 30 s at 75° C (reprinted with permission from Journal of Biomedical Optics [75]).*

1.7.4.2 Monitoring of wound healing

Wound healing is a complex process wherein the injured tissue is repaired, and proceeds in overlapping phases of hemostasis, inflammation and proliferation. The proliferation phase involves synthesis and remodelling of collagen fibers, angiogenesis and wound contraction. Non-invasive technologies for monitoring wound healing are thus important tools to aid clinicians and researchers who need safe ways to evaluate healing. Oh et al made use of PSOCT to monitor wound healing in rabbit skin tissue under presence of healing and anti-healing drug [76]. Wounds were imaged at different time points post wounding and phase retardance values were also computed. Phase retardance was observed to be higher for sites treated with healing agent as compared to those treated with anti-healing agent. Results show that the healing process can be quantified by PS-OCT as it monitors the progress of collagen matrix remodeling, its content and fiber orientation. Fig. 1.8 shows the PSOCT images obtained at 14 day post wounding for the control as well as treated sites.

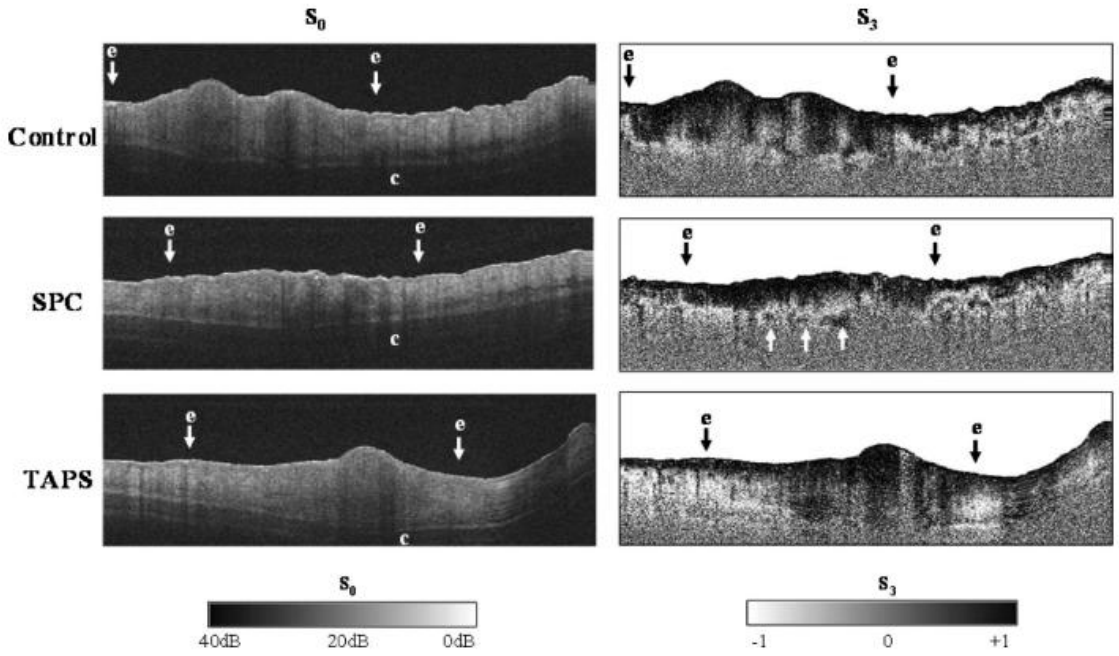

Figure 1.8 *(Left) Backscattering intensity S_0 and (Right) birefringence images S_3 for control, sphingosylphosphorylcholine (SPC) and tetraacetylphytosphingosine (TAPS) tretaed sites. Image size: 1.3 mm (depth) x 8.5 mm (width). Wound edges and cartilage are marked as e and c, respectively. Arrows point to wound boundaries. White arrows in the S_3 image for the SPC case indicate a region with rapid gray level change inside the wound healing region (reprinted with permission from Journal of Biomedical Optics [76]).*

1.7.4.3 PSOCT in basal cell carcinoma

Basal Cell Carcinoma (BCC) is one of the common types of skin cancer that begins in the basal cells lining the epidermis. As it progresses deeper into the skin, the normal architecture is lost, including the vessels, pilosebaceous units, nerves, and glands. This is attributed to action of proteases released from the tumor cells and altered collagen synthesis by tumor stromal cells. The combination of loss of normal structures, destruction of collagen and synthesis of mucopolysaccharides alters the fundamental structure of the dermis. Strasswimmer et al found that there is a dramatic alteration in birefringence in the case of both ulcerated and infiltrative examples of BCC when they are compared to each other and to perilesional skin [77]. Fig. 1.9 shows the intensity and

phase retardance images for the uninvolved perilesional skin and the nodular infiltrative basal cell carcinoma.

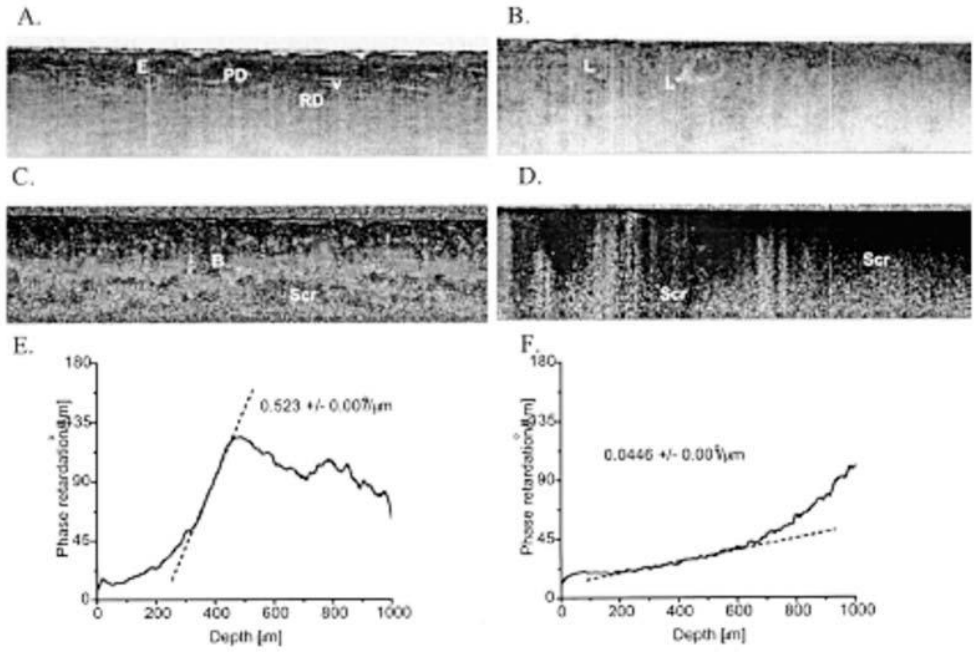

Figure 1.9 *(A) Standard intensity OCT image of uninvolved perilesional skin; (B) OCT image of nodular infiltrative basal cell carcinoma; (C) PSOCT image of uninvolved perilesional skin; (D) PSOCT image of nodular infiltrative BCC; (E) and (F) show the phase retardation of plot for pre-lesion and BCC tissue (reprinted with permission from Journal of Biomedical Optics [77]).*

1.7.5 Doppler optical coherence tomography

Doppler Optical Coherence Tomography (DOCT) is a low coherence interferometric technique to extract depth resolved blood flow information in blood vessels. High spatial and temporal resolution, non-contact and non-invasive nature of imaging, flexibility to integrate with clinical systems, and the ability to provide depth resolved flow information with high speed and sensitivity are among the main features of DOCT that make it an attractive tool for obtaining flow information. DOCT can provide 3-D tomographic map and velocity profile of blood flow, which can be of potential use in applications like determination of wound closure, monitoring efficacy of laser treatment of port wine stains, monitoring the effect of pharmaceutical drugs on blood flow, etc.

Although DOCT is fundamentally similar to Laser Doppler Flowmetry (LDF), there are significant differences [78]. While LDF suffers from imprecise imaging due to the long coherence length of the source used, DOCT uses low coherence property of OCT to overcome this drawback and therefore it provides depth resolved velocity information. Here, the velocity resolution depends on detection electronics, scan angle and acquisition time. While earlier time domain DOCT provided resolution of ~ 10-100 μm/s, the new generation FDOCT systems can provide resolution of few μm/s [78-81].

The basic concept of DOCT lies in the Doppler effect, which describes the change in frequency of waves reflected from moving objects. The amount of change in frequency can be used to determine the velocity of moving object. For electromagnetic waves, the Doppler shifted frequency is $f_D = \sqrt{\frac{c+u}{c-u}} f_o$

where f_0 is the initial frequency of electromagnetic wave, c is speed of light and u is the speed of the moving object. Here, u is assumed positive when moving towards observer, and hence an apparent increase in the frequency ($\Delta f = f_D - f_0$ is positive). Similarly, u is assumed negative when moving away from observer, and hence an apparent decrease in the frequency ($\Delta f = f_D - f_0$ is negative). For $u \ll c$, $\Delta f = \frac{u}{c} f_D$.

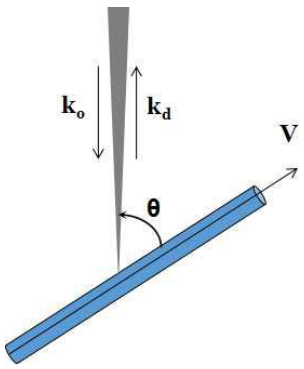

Figure 1.10 *Schematic showing the formation of Doppler angle between the incident beam and the flowing scatterers inside the tube.*

Fig. 1.10 shows a schematic of sample arm of DOCT, where the incident beam is at an angle θ to the direction of flow. Incident light is scattered by moving particles and undergoes Doppler shift twice, once from source to particle and other from particle to detector. Consider the incident wave-vector $\mathbf{k_0}$, scattered wave-vector $\mathbf{k_d}$, and the velocity vector of moving particles **V**. The Doppler frequency shift may be expressed as

$$f_D = \frac{1}{2\pi}(\mathbf{k_d} - \mathbf{k_o})\mathbf{V}$$

Since $|\mathbf{k_0}| = |-\mathbf{k_d}| = k = 2\pi/\lambda_0$, $f_D = \frac{2V\cos\theta}{\lambda_0}$

The above equation shows that the Doppler shift depends on the velocity of moving scatterer and the Doppler angle (the angle between the incident beam and the direction of flow). Therefore to be able to quantify the flow rate using DOCT, one must be able to measure the frequency shift.

1.7.6 DOCT based modalities for microcirculation imaging

DOCT has given birth to various modalities for microcirculation imaging. The first two dimensional *in-vivo* DOCT was generated using spectrogram method in 1997 by Chen et al [82]. Here, a Short Time Fourier Transform (STFT) is performed on successive time segments of Doppler signal current which provides the spectral information in that time segment, and then the window is moved to next time segment. Continuing this process, the signal is simultaneously analysed in frequency and time domains. A major drawback with this method is the coupling between velocity sensitivity and spatial resolution. Choosing a large time window increases the velocity sensitivity but degrades the spatial resolution and vice versa. This severely limits its ability for real time *in-vivo* imaging of blood flow as increased frame rates lead to reduced velocity sensitivity.

Unlike spectrogram method, phase resolved DOCT (PRDOCT) does not suffer from coupling between spatial resolution and velocity resolution. Here the phase difference

between adjacent A-scans is used to calculate flow velocity [83]. The method provides access to the axial flow component i.e. along the direction of incident beam according to the expression

$$V_z = \frac{\lambda_0 \Delta\Phi}{4\pi n \Delta T} \qquad \text{.....(1.6)}$$

where V_z ($=V\cos\theta$) is the axial velocity component, λ_0 is the central wavelength of light source used, $\Delta\Phi$ is the phase difference between adjacent A-scans, n is tissue refractive index, ΔT is the time between adjacent A-scans and θ is the Doppler angle (the angle between flow direction and direction of incident beam). The sign of the phase difference also helps determine the direction of blood flow. Since the method uses phase difference between adjacent A-scans, this is most widely used in Fourier domain approach which directly provides access to the phase information.

Usually, oversampling factor of 10 is used so that the static portions of the sample are highly correlated between adjacent depth scans (or A-scans) and any phase difference will be due to the flow. Since the method is phase sensitive, the minimum detectable velocity is governed by the phase stability of the setup. For a typical phase stability of 20 mrad and exposure time of 100 μs, velocity sensitivity as low as 10 μm/s can be achieved. Due to phase wrapping, maximum possible measurable velocity is determined by the maximum possible phase difference of 2π i.e. $v_{max} = \lambda/2n\Delta T$. Several methods to overcome this phase wrapping artifact have been developed that extend the measurable velocity range [84,85]. Since the method provides axial flow velocity, prior knowledge of Doppler angle is required for obtaining absolute velocity. This however is not generally possible with most biological tissues where tortuous blood vessels are surrounded by turbid tissue bed. To overcome this problem, multi-beam approaches have been developed where multiple beams (2 or 3) are used to simultaneously probe the same spatial location of the tissue from different angles to provide flow velocity information in

2/3 dimensions. We have also developed novel dual and three beam approaches for determination of absolute flow velocity, as discussed in Chapter 3. There are several situations like port wine stains, atherosclerosis, etc where visualizing microcirculation is equally important as is the flow velocity. As will be seen in Chapter 4, several intensity based techniques like correlation mapping OCT, speckle variance OCT and optical micro-angiography (OMAG) have been developed that allow *in-vivo* visualization of the three dimensional vascular network inside the tissue. Here endogenous contrast arising due to scattering from flowing scatterers allows visualization of the vascular network. Also these techniques are independent of Doppler angle and are better resistant to bulk motion artifacts.

1.7.7 Biomedical applications of DOCT

The non-invasive nature and high spatial resolution offered by DOCT coupled with its depth sectioning ability make it important for a wide variety of clinical situations. DOCT can be used to obtain three dimensional vasculature alongwith the flow patterns and flow velocities through them at any desired location.

1.7.7.1 Imaging brain vasculature and hemodynamics

Doppler OCT has been used to image cerebral microvasculature and assess hemodynamics in cerebral cortex of brain [86]. Any deviation in the cerebral blood flow (CBF) pattern from normal may result in stroke, alzheimer's disease, etc. Gold standard for regional blood flow determination is autoradiography which involves administration of a radioactive tracer drug such as iodo[14C]antipyrine for a short duration of time followed by cardiac arrest and freezing. Autoradiography of frozen sections determines the radioactivity level at various tissue sites, which is then related to blood flow [87]. By monitoring the clearance (or activity) of the tracer drug, blood flow can be ascertained as blood flow rate is inversely proportional to decay half-life. Although the technique can provide spatial information, it does not provide information on temporal changes in CBF

pattern. Although laser Doppler flowmetry and laser speckle imaging can be used to obtain spatially resolved flow patterns, they provide perfusion values without any depth resolved information. DOCT overcomes the drawback of these techniques and can provide real-time three-dimensional, depth resolved and absolute CBF measurements that can prove useful in studying functional cerebral activation and cerebral pathophysiology. Fig. 1.11 shows the OCT angiogram of the rat cortex.

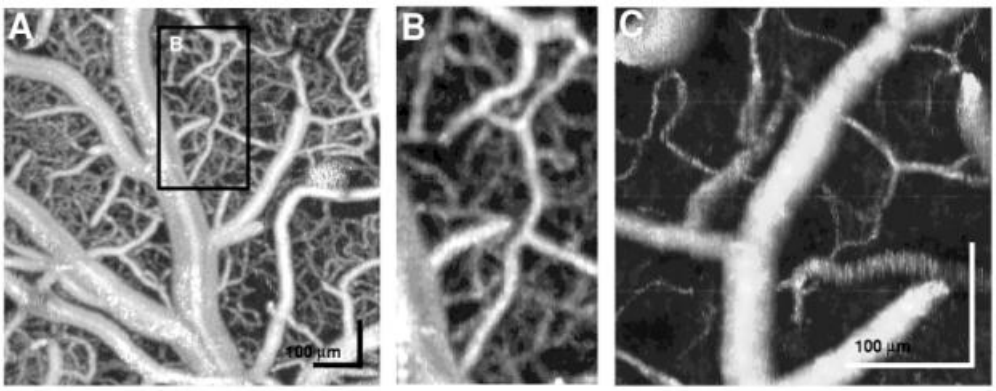

Figure 1.11 *(a) OCT maximum intensity projection (MIP) angiogram of the rat somatosensory cortex showing comprehensive visualization of the vasculature at 12.0 µm transverse resolution; (b) zoom of arterial anasthmosis, showing visualization of surface vessels as well as capillaries below; (c) OCT MIP angiogram acquired with a 3.6 µm transverse resolution in a different animal (reprinted with permission from Optics Express [86]).*

1.7.7.2 Monitoring efficacy of laser treatment of port wine stains

In-vivo monitoring of the efficacy of laser treatment of port wine stains (PWS) is the first clinical application of DOCT. PWS is a congenital disease characterized by progressive vascular malformation of capillaries in the dermis of human skin. PWS can be treated by using pulsed laser to selectively coagulate the PWS vessels. Presently, no technique exists that can assess the efficacy of laser treatment of PWS. Phase resolved DOCT provides a real time monitoring of the efficacy of laser treatment. Fig. 1.12 shows the DOCT structural and velocity images before and after laser treatment in a PWS patient. The

velocity image after treatment does not show any blood vessel, thereby verifying the accurate destruction of blood vessels in laser treatment [88].

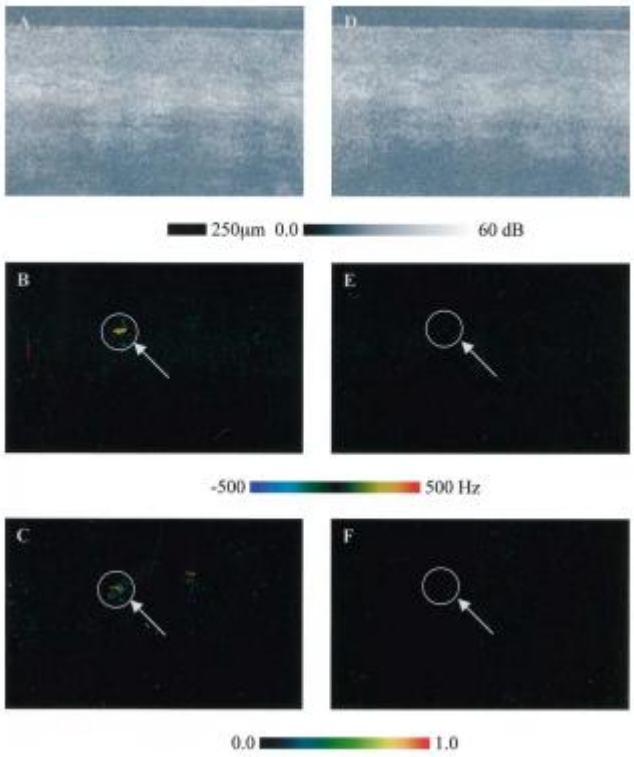

Figure 1.12 *Tomographic images of identical PWS sites before (A–C) and after (D–F) laser treatment. A, D, Structural images; B, E, Doppler-shift (blood flow velocity) images; C,and F, normalized variance of flow velocity. The vessel areas are marked by circles and arrows in the velocity and variance images (reprinted with permission from Optics Letters [88]).*

1.7.7.3 *In-vivo* imaging and quantification of ocular blood flow

DOCT has been widely used for microvasculature imaging and flow velocity assessment in the retinal and choroidal regions of the eye. Accurate knowledge of retinal hemodynamics may prove helpful in understanding several ocular diseases, including diabetic retinopathy, glaucoma, and age-related macular degeneration. OMAG has been used to map microvasculature of the retina and choroid in humans. Subsequently, Doppler OMAG (DOMAG) has extended OMAG's capability to quantitatively measure blood flow velocity [89]. Fig. 1.13 shows the absolute velocity determination using DOMAG.

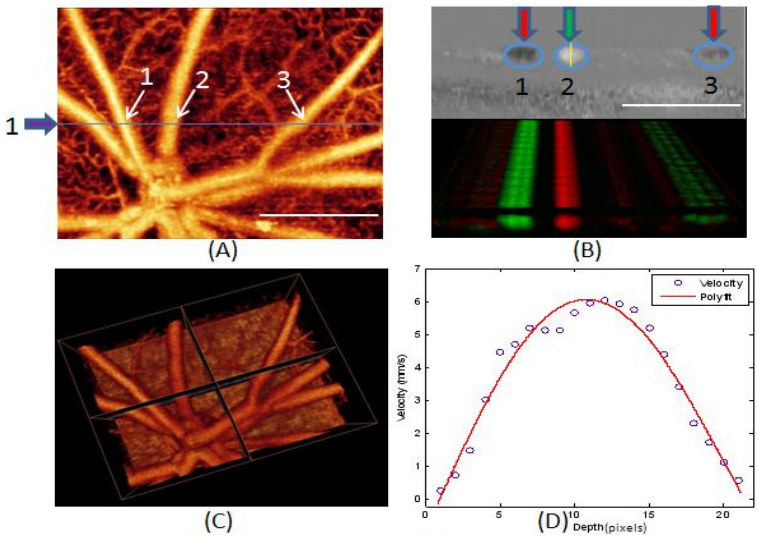

Figure 1.13 *Measurement of absolute velocity within retinal blood vessels in the rat. (A) Microvasculature angiogram of a normal rat retina in-vivo where the blue line and arrow indicate where the DOMAG data were captured. (B) DOMAG phase difference map in one cross section (upper row) and the 3D rendered phase difference extended in 20 seconds at the same cross section. (C) 3D vasculature image showing the vessel orientation that was used for calculating the Doppler angle and vessel diameter for the vessels being analysed. (D) The axial velocity profile of vessel 2 along depth direction. White bar = 500 µm (reprinted with permission from Biomedical Optics Express [89]).*

1.7.8 Molecular contrast OCT

OCT, a low coherence interferometric technique for tissue imaging, gains its contrast by probing variations in the refractive index of tissue. While conventional OCT is highly sensitive to structural changes, it cannot provide molecular information as refractive index variations between different types of biomolecules is insignificant. Molecular-sensitive imaging modalities enable better understanding of local biochemistry of tissue, and better visualization of pathological and physiological processes. Merging molecular sensitivity with structural imaging at micron-scale resolution can provide complete characterization of tissue. Unfortunately, due to its interferometric detection scheme, OCT is incompatible with many common methods for obtaining molecular contrast like fluorescence emission and Raman scattering because of their incoherent nature. However, adding molecular contrast to OCT provides several advantages when compared to existing microscopic molecular imaging techniques, such as larger working distances,

increased penetration depths and heterodyne detection [90]. More importantly, adding molecular contrast to OCT enables specific imaging of biomolecules such as hemoglobin and melanin, as well as exogenous chromophores such as dyes or nanoparticles targeted to particular cellular or biochemical process. There have been several efforts to introduce molecular contrast into OCT. Pump–probe optical coherence tomography (PPOCT) is an extension of OCT that enhances the contrast of OCT images on the basis of transient absorption in the sample induced by an external pump beam [91]. Photothermal OCT is another extension of OCT that exploits the photothermal effect using endogenous or exogenous chromophores to detect thermally-induced changes in refractive index [92]. Spectroscopic OCT (SOCT) and Second Harmonic OCT (SH-OCT) are two important ways of introducing molecular contrast in OCT [93,94]. While SOCT monitors wavelength dependent absorption and scattering to gain molecular insight, SH-OCT takes advantage of intrinsic second harmonic generation of structures like collagen fibers. Two fundamental sources of contrast in SOCT imaging are wavelength dependent absorption and wavelength-dependent scattering. Endogenous or exogenous materials with characteristic absorption profiles such as melanin, hemoglobin, water, or contrast-enhancing dye can be used to provide spectroscopic contrast based on wavelength dependent absorption [95]. Wavelength-dependent scattering contrast is based upon the fact that scattering particles of different size, refractive index, and spatial distribution produce backscattered spectra with a characteristic modulation of the spectrum. Therefore, by examining the spectral modulations present in spectroscopic OCT signals, variations in the size and density of scattering particles in biological tissue samples may be differentiated. Since the cells that compose various types of tissue typically have varying organelle sizes and densities, examining spectral modulation may lead to contrast enhancement of different cell types. Diseases such as cancer often cause changes in cell size, nuclear size, and mitochondrial density which may reflect as changes in

spectroscopic OCT images. Fig. 1.14 shows the conventional OCT image and the SOCT image of African frog tadpole (Xenopus laevis) [93]. It is seen that the cell membranes, cell nuclei and melanocytes exhibit higher backscattering as compared to cytoplasm. In the SOCT image, a red hue shows long-wavelength enhancement of backscattered light, while green hue shows long-wavelength enhancement of backscattered light. The upper part of SOCT image has green hue and the lower portion has red hue, which is in accordance with the larger penetration depth of higher wavelengths. Melanocytes marked by arrows appear bright red, probably because of enhanced absorption of melanin at shorter wavelengths [93]. It can be seen that melanocytes are easily differentiated by spectroscopic OCT as compared to conventional OCT.

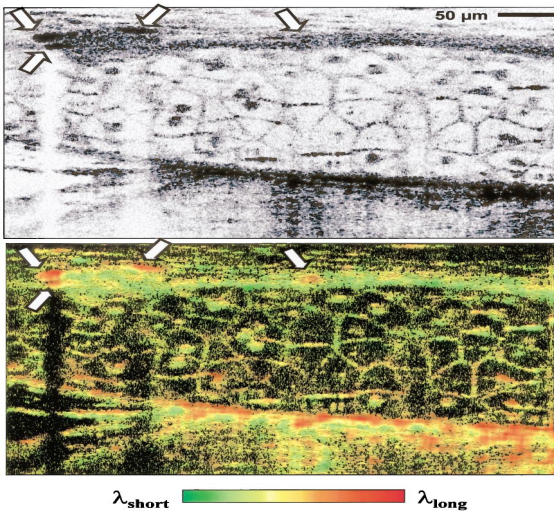

Figure 1.14 *(Top) In-vivo conventional OCT and (bottom) spectroscopic OCT image of an African frog tadpole (Xenopus laevis) (reprinted with permission from Optics Letters [93]).*

Second harmonic generation (SHG) is an effect where a nonlinear material converts two photons of one frequency to a single photon of twice the frequency. Because of the symmetry of the process, SHG does not occur in a uniform, isotropic medium. SHG is generally produced at surfaces, in birefringent media, or by asymmetric structures such as rod-like or fiber like structures. SHG is very promising as a sensitive probe in tissue

morphology and physiology studies. Collagen is the predominant structural protein in most biological tissues, as well as an efficient source of SHG due to its triple helix structure. Modifications of the collagen fibrillar matrix structure are associated with various physiologic processes, such as wound healing, aging, diabetes, and cancer. SH-OCT has been used to generate high-resolution high-contrast images of collagen fibrils organization in rat tail tendon [94]. Fig. 1.15 shows the SH-OCT image of rat tail tendon, where many cable-like, parallel oriented, and slightly wavy collagen fiber bundles can be visualized.

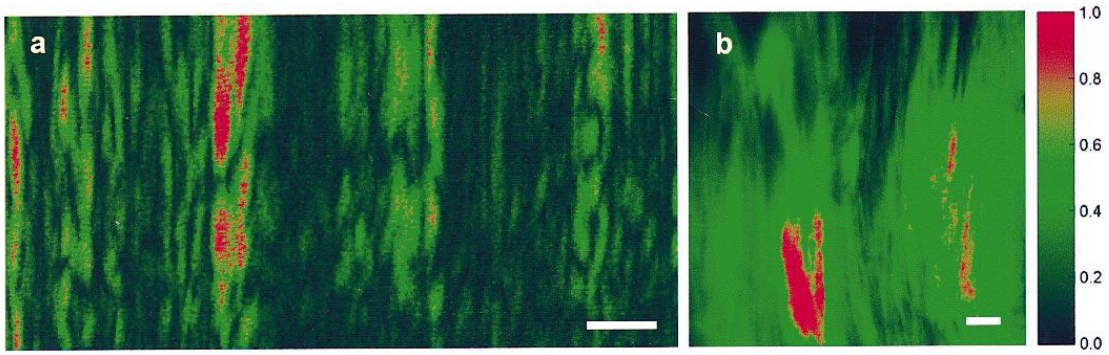

Figure 1.15 *(a) SH-OCT image showing an area of 100 x 50 µm in the rat-tail tendon. The transverse and axial resolutions of this image are 1.9 and 4.2 µm, respectively; (b) 60X polarization microscope image of the same sample (scale bar: 10 µm) (Reproduced from [94], with the permission of AIP Publishing).*

1.8 Conclusions

In this chapter, we discussed OCT, its major functional variants and their applications. It was seen that OCT measures the strength of backscattered light to obtain the reflectivity map of the sample. These reflectivity variations arise due to the minute refractive index variations within the tissue sample. Apart from tissue reflectivity, other parameters of the sample like birefringence, blood flow, etc can also be determined by measuring change in properties like polarization, phase, etc of reflected light. This additional information may be intimately related to functional disturbances, which usually precede morphological changes and could be useful for early diagnosis of diseases. This has given rise to the

various functional extensions of OCT like polarization sensitive OCT, Doppler OCT, spectroscopic OCT, Second harmonic OCT, etc that provide functional information like birefringence, flow velocity, and molecular information of the tissue.

Chapter 2

Development and utilization of spectral domain PSOCT setup

In this Chapter, we first present the development and characterization of a single detector based spectral domain PSOCT setup. The developed system provides identical depth dependent sensitivity for the orthogonal polarization channels. We then present the use of the developed setup for *ex-vivo* imaging of human oral mandibular tissue samples. Our results show that compared to the changes observed in the parameters obtained from intensity images like epithelium thickness and the decay constant of A-scan intensity profile, a much larger degree of change was observed in the phase retardation for tissue sites progressing from normal to the malignant state. These results suggest that monitoring tissue retardance can help in better differentiation between normal and cancerous oral tissue sites.

Work discussed in this chapter has resulted in the following publication:

1. "Human ex-vivo oral tissue imaging using spectral domain polarization sensitive optical coherence tomography", **P. Sharma**, Y. Verma, K. Sahu, S. Kumar, A. V. Varma, J. Kumawat, P. K. Gupta, *Lasers in Medical Science*, **2017**, 32, 143-150.

2.1 Requirement and challenges in development of spectral domain PSOCT setup

PSOCT is a functional extension of OCT that provides information on tissue birefringence by measuring the change in the polarization of backscattered light. Since several biological tissues like collagen, tendon, cartilage, teeth, etc display significant birefringence, accurate measurement of birefringence can help in better diagnosis and management of pathologies of such tissues. Owing to this, PSOCT has been used in several pathological conditions like determination of wound healing, estimation of burn depth, caries detection in tooth, differentiation of cancerous tissue, etc [75-77], as already discussed in Chapter 1.

PSOCT systems, in general require measurement of the orthogonally polarized components of back scattered light to generate high resolution depth resolved retardation images of tissue. Initial PSOCT systems were based on time domain approach and generally made use of two separate detectors for measurement of orthogonal polarization channels [67]. Spectral domain systems are more suited to *in-vivo* imaging conditions owing to their increased imaging speed and higher sensitivity as compared to their time-domain counterparts [68]. A widely used methodology to perform spectral domain PSOCT measurements involves separation of the two orthogonally polarized components by using polarizing beam splitter or Wollaston prism [69,70,96-98]. While two independent spectrometers can be used for these measurements, it not only leads to an increased cost of the setup but also suffers from the drawback of artifacts in birefringence measurements arising due to the difference in the response function of the two detection channels [69,96]. One of the approaches used to address this issue has been to find a way of imaging the two orthogonal polarization components of the back scattered light on adjacent halves of a single line scan camera [70,97,98]. However because only half of the

total line scan camera pixels are used for each orthogonal polarization channel, the imaging depth of the setup is reduced by a factor of two compared to the case when each polarization channel sees all the pixels. Further, the spatially separated orthogonal polarization channels do not follow identical path in the spectrometer which leads to different distortion in their spectral shapes. Therefore, a careful software based correction of the recorded interference spectra is required to achieve identical depth dependent sensitivity.

Single detector operation where both polarization channels see all the pixels has been implemented by introduction of a path delay between the two orthogonally polarized channels in the reference arm [99,100]. Although this approach has several advantages it has a problem arising due to the fact that spectral domain approach suffers from reducing sensitivity of measurement with increasing depth. This is because the contrast of interference fringes decays as a function of depth [101]. Because the images for the two orthogonally polarized components are created at different depths from the plane corresponding to the zero optical path difference between the reference and the sample arm, the depth dependent sensitivity profile (S_D) for the two orthogonal polarization channels is different. In fact, because of the methodology used to remove the complex conjugate images, the measurement sensitivity for one of the polarization channels is higher for the top surface and gradually decays with depth while for the other it is less for the top surface and gradually increases with depth. Although one can in principle correct it using the estimated depth dependence of the sensitivity, the unmatched noise properties as a function of depth for the two polarization channels would introduce error in retardation calculations. Further, the optical path delay introduced to separate the two orthogonal polarization channels in depth domain needs to be larger than the imaging depth of the system. Therefore it needs to be adjusted depending upon the scattering properties of the sample. Another single detector based approach where both polarization

channels see all the pixels involves sequential probing of the sample with three different polarization states of incident light [102]. This however increases the image acquisition time by a factor of three and hence makes it unsuited for *in-vivo* imaging applications.

In this chapter, we first present the development of a simple, single camera based approach for spectral domain polarization sensitive measurement where both orthogonal polarization channels see all the pixels. Incorporation of a novel triangular reference arm results in identical depth dependent sensitivity profile for the orthogonal polarization channels without making use of any software based correction. Unlike the earlier reported scheme, our scheme does not require any adjustment of the depth location of the images corresponding to orthogonal polarization channels according to the scattering properties of the sample. We further show the use of the developed spectral domain polarization sensitive optical coherence tomography (SD-PSOCT) for the differentiation of normal and malignant human oral mandibular tissue samples. Measurements made on epithelium thickness, decay constant of the A-scan intensity profile and phase retardance in *ex-vivo* human oral mandibular tissue samples suggest that measurement of tissue retardance allows better differentiation of normal and malignant tissues.

2.2 Development of SD-PSOCT system

2.2.1 Experimental arrangement

A schematic of the developed SD-PSOCT setup is shown in Fig. 2.1. The developed setup makes use of a 5 mW superluminescent diode with center wavelength 840 nm and bandwidth ~ 40 nm. The output was collimated and then passed through a polarizing beam splitter to get vertically polarized light beam. This vertically polarized input beam was then split into reference and sample beams using a non-polarizing beam splitter (NPBS). In the sample arm, the passage of the vertically polarized light through a quarter waveplate (QWP) with its fast axis oriented at 45° to the incident vertical polarization leads to circularly polarized light incident on the sample. This is done to ensure that the

tissue retardance measurements are independent of the fast axis orientation of the tissue. This circularly polarized light was the focused on the sample using an achromat lens of focal length 30 mm. The galvo-scanner was driven by a saw-tooth waveform generated from a function generator for lateral scanning of the probe beam on the sample.

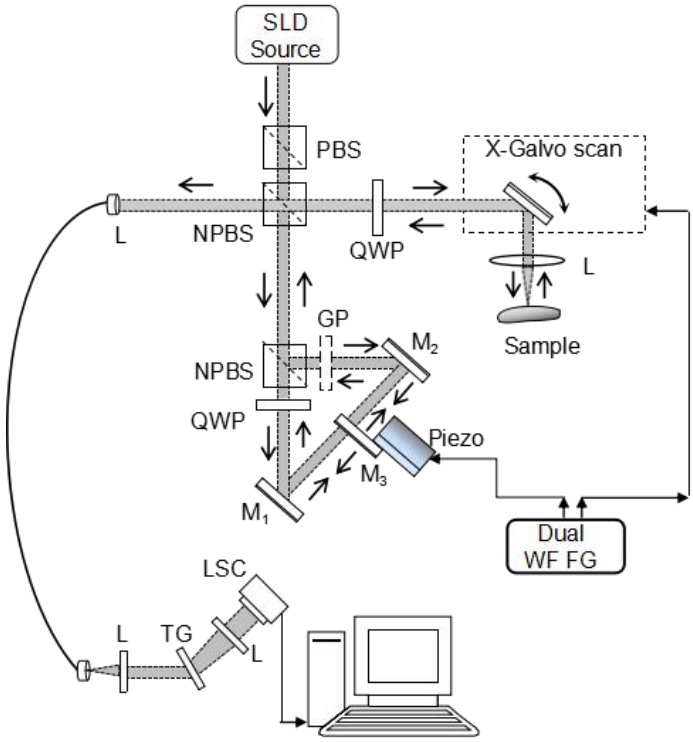

Figure 2.1 *Block diagram of SD-PSOCT setup. SLD Superluminescent diode, PBS Polarizing beam splitter, NPBS Non-polarizing beam splitter, QWP Quarter waveplate, L Lens, M_1 M_2 M_3 Mirrors, LSC Line scan camera, GP Glass plate, TG Transmission grating, WFFG Wave form function generator.*

The dual reference arm was arranged in a triangular geometry. Here, the incoming vertically polarized beam was split into two reference beams using a NPBS. These mutually perpendicular transmitted and reflected reference beams, incident at angle of 22.5° to the normal on mirrors M_1 and M_2, were then back reflected by a normal incidence mirror M_3 mounted on a piezo translation stage. In the path of the transmitted reference beam, a QWP with its fast axis oriented at 45° with respect to horizontal was

placed so that horizontally polarized light (orthogonal to incident vertical polarization) is generated after round trip propagation. Because there is no polarization optics in the path of the reflected reference beam, it maintains its original vertical polarization state. In this way, round trip propagation through the dual triangular reference arm assembly results in two reference beams with orthogonal (horizontal (H) and vertical (V)) polarization states. Using a piezoactuated stage, the mirror M_3 was given a small forward or backward movement (amplitude ~ 50 μm, 10 Hz synchronous to the galvo scanner movement) to introduce a simultaneous increase and decrease in the path lengths of the orthogonally polarized reference beams by equal amounts. This movement of mirror M_3, synchronous with transverse scanning introduces a constant modulation frequency in the spectral interferogram which enables use of Hilbert transformation for the removal of the complex conjugate mirror images [19]. A focusing lens was used to couple the back reflected beams coming from sample and reference arms to a single mode fiber. The single mode fiber directs the interfered light to the spectrometer where it is first collimated with a 50 mm focal length lens and then dispersed by a volume phase transmission holographic grating (1200 lines/mm, Wasatch Photonics, UT, USA). A 150 mm focal length imaging lens spatially Fourier transformed the dispersed beam onto the line scan camera (14 μm pixel size, Atmel, CA, USA) which was operated at 10 kHz readout rate (corresponding to integration time of 100 μs). Each B-frame was composed of 1000 A lines, each line being 1024 pixels in length. The interferometric data was digitized by a PCI-1428 (National Instruments, TX, USA) camera link image acquisition board. NI-IMAQ software was used under Labview™ environment for data acquisition and subsequent processing. It should be noted that the saw-tooth waveforms for driving the galvoscanner for lateral scanning of the probe beam on the sample, and back and forth motion of piezo translation stage should be synchronized with each other and hence a dual waveform function generator was employed to generate these synchronized waveforms. A trigger

signal generated by the same function generator was used to trigger the data acquisition card in synchronization with the saw-tooth waveforms. The acquired interferogram was preprocessed using mean dc subtraction and spectral reshaping for removal of fixed pattern noise and side-lobes of axial point spread function in depth domain [103-105]. This was followed by even sampling in k-space by means of cubic spline interpolation. The FFT of the resampled interference spectrum generates the depth resolved intensity (structural) and phase images. Prior to the generation of PSOCT images, these intensity images were further thresholded for the suppression of the background noise. The system features axial and lateral resolutions of ~10 µm and 30 µm respectively, with a maximum imaging range of ~2 mm (limited by the spectral resolution (~0.09 nm) of the spectrometer). The measured signal sensitivity (SNR) of the system was 95.5 dB at 100 µm optical path delay which reduced to 80 dB at a depth of 1.8 mm.

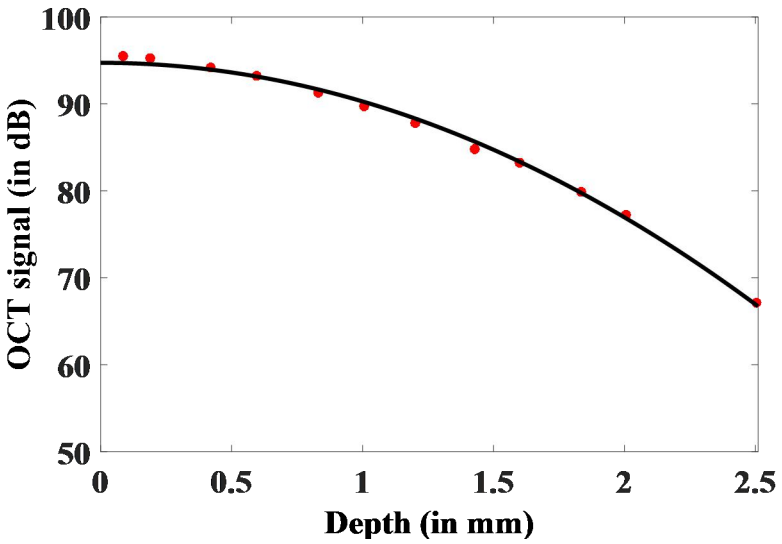

Figure 2.2 *The measured variation of sensitivity with depth. Red dots represent experimental points and black solid line represents the polynomial fit.*

Fig. 2.2 shows the measured variation of sensitivity with depth for the developed setup where red dots represent experimental points and black solid line represents the polynomial fit [11,18]. It is important to note that the choice of the central wavelength of

the source depends on interplay between the desired axial resolution and imaging depth. Most often, OCT setups make use of broadband source with central wavelength in the spectral range 800–1350 nm (where the tissue attenuation is minimal). Scattering of light by tissue is the major limiting factor for OCT imaging depth and in most biological tissues such as oral tissue, esophagus, skin, etc it is about a mm for 840 nm wavelength of light [106]. It is also known that the scattering coefficient reduces with the increase in the wavelength and hence use of 1300 nm can provide greater penetration depth as compared to 840 nm [105]. However, the axial resolution in OCT is compromised with use of longer wavelength because of the $\lambda^2/\Delta\lambda$ dependence. This results in an axial resolution of > 20 μm with 1300 nm wavelength light (considering identical spectral bandwidth ~ 40 nm) as compared to ~ 10 μm resolution achieved with the use of 840 nm. Because of the higher resolution, we chose to work with 840 nm as one of the objectives of our work was to monitor changes in the epidermal thickness. Also the maximum imaging range of ~ 2mm available with the use of 840 nm was sufficient for our studies.

2.2.2 Removal of complex conjugate mirror artifact

One of the important and attractive aspects of the developed SD-PSOCT setup is the removal of complex conjugate artifact such that the orthogonal polarization channels exhibit identical depth dependent sensitivity. In this section, we shall see how this task is accomplished. Fig. 2.3A shows an A-scan for orthogonal polarization components (H & V) and their complex conjugates (mirror images) i.e. H' and V' along with the depth dependent sensitivity profile (S_D) for a conventional single detector based SD-PSOCT system. The depth profiles for H and V components are shown by solid line and that for the corresponding mirror images (H' and V') by dashed lines. The movement of the piezoactuated stage on which the common mirror M_3 is mounted introduces simultaneous (equal and opposite) path change (and hence phase shift) in the two reference beams. In the earlier reported scheme where both the reference beams undergo equal phase shift

[99,100], the complex conjugate mirror images were removed from one side of the zero delay line, as shown in Fig. 2.3B. The zero path delay plane can then be positioned between the orthogonal polarization images (as is shown in Fig. 2.3C) through proper adjustment of reference path lengths for maximum utilization of the high sensitivity zone around the zero delay position [99]. One can now see that this leads to a difference in the depth dependent sensitivity profile for both the images because the top surfaces in the two images are located at different depths from the zero delay position. In fact, the sensitivity reduces with depth inside the sample for one polarization state (V) and increases with depth inside the sample for the other polarization state (H). In our scheme, the reference arm is arranged in the form of a triangle using mirrors M_1, M_2 and M_3. Since the two reference beams are reflected off from opposite sides of the common mirror M_3, the movement of the piezo stage introduces equal and opposite phase shifts in the orthogonal polarization components (OPC) of light, resulting in orthogonal polarization images placed on the opposite side of zero delay line (as shown in Fig. 2.3D) on application of Hilbert transform. The path length in the dual reference arm was then suitably adjusted so that the orthogonal polarization images are present at the same depth from the zero delay position (as shown in Fig. 2.3E). The major advantage of this scheme is that since both the orthogonal polarization images are on opposite sides of zero delay line with identical S_D, simultaneous measurements can be done. The reflectivity and retardance images were generated using orthogonal polarization images. The depth resolved reflectivity image *R(z)* was obtained by summing the squares of the magnitudes ($A_{H,V}(z)$) of the envelopes of the interferograms and the retardation image $\delta(z)$ was obtained by computing the arc tangent of their ratio [66].

$$R(z) = A_H(z)^2 + A_V(z)^2 \qquad \text{..... (2.1)}$$

$$\delta(z) = \tan^{-1}\left(\frac{A_V(z)}{A_H(z)}\right) \qquad \text{..... (2.2)}$$

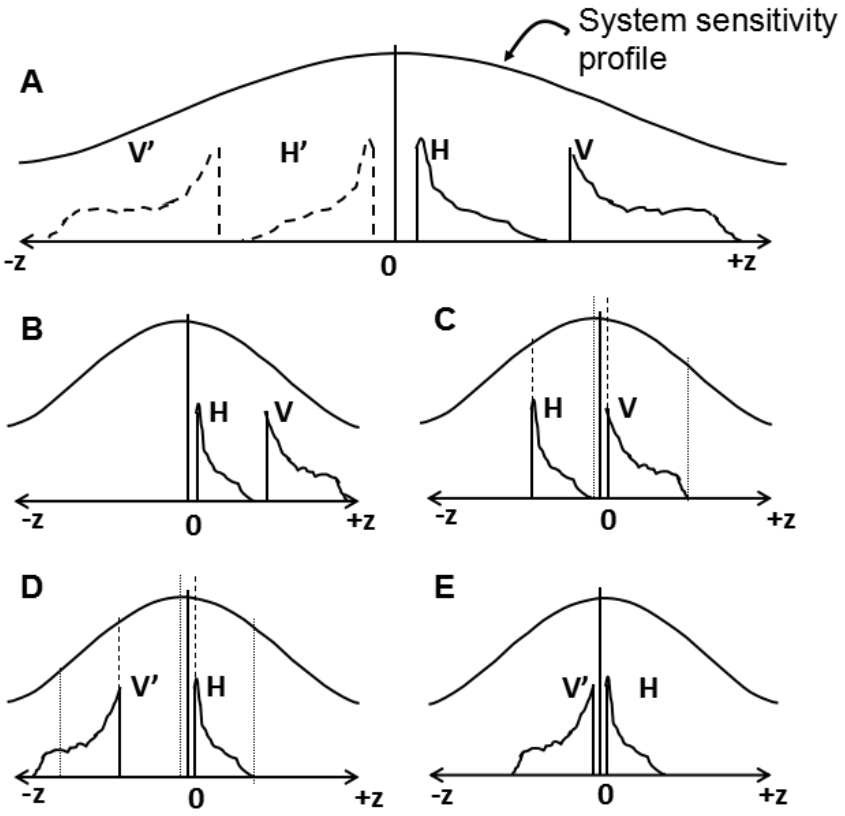

Figure 2.3 *Depth scan of orthogonal polarization components (H and V) of back scattered light. (A) Without phase shifting, (B) with phase shifting (same for both orthogonal polarization components) and with optical delay between them, (C) is same as (B) with adjusted reference arm lengths to utilize maximum sensitivity near the zero delay, (D) with equal and opposite phase shifting for both orthogonal polarization components and with optical delay between them, (E) is same as (D) without any optical delay between orthogonal polarization reference beams. H' and V' are the complex conjugate mirror images of H and V.*

A closer look at equation (2.2) will help in understanding the importance of the identical depth dependent sensitivity for the orthogonal polarization channels offered by our scheme. Since the retardation calculation involves the ratio of the orthogonal polarization channels, the retardation measurements in the conventional scheme utilizing equal phase shifting will be either more or less (depending on the top surface of which polarization channel is closer to the zero delay plane) than the actual values. The retardation measurements in our scheme will be more closer to the actual values as both the orthogonal polarization channels experience identical depth dependent sensitivity.

2.2.3 Calibration of the developed setup

The developed SD-PSOCT setup was calibrated by performing phase retardance measurements for a quarter-wave plate (WPA 4412-690-1200, Union optic). The QWP was rotated from 0° to 360° (in steps of 10°) in a plane perpendicular to the incident beam. The retardation value was averaged over 20 A-scans for each orientation and was measured to be 84.17°± 0.04°. The variation between the measured and expected retardation value (90°) is attributed to the wavelength dependence of the retardation of the QWP and possible errors in waveplate fabrication. The measured phase retardation values were observed to be independent of the orientation of the QWP in a plane perpendicular to probe beam, as shown in Fig. 2.4. Since the computation of retardance values involves ratio of the measured components, the identical sensitivity profile offered by our scheme for the OPC helps provide accurate results. To demonstrate the superior performance of our approach, we performed retardance measurement of same QWP using equal phase shifting as in a conventional depth encoded approach. For this, the piezo stage was made stationary and the path lengths of the two reference arms were adjusted such that the orthogonal polarization images were separated by ~ 2mm. Separation distance of 2 mm was chosen because most scattering samples provide a penetration depth of ~ 2mm. Complex conjugate mirror image artifact removal was accomplished using galvoscanner based phase shifting [107]. The measured retardance values will be higher or lower than the actual ones depending on which polarization channel experiences reduced sensitivity (due to a depth separation of 2 mm between OPC). In our case, the top surface for H polarization image was close to zero delay line while the top surface for the V polarization image was present at a greater depth. As can be seen from equation (2.2), the reduced sensitivity for V polarization will reduce A_V leading to lower retardance values. The average retardation value for 20 A-scans was measured to be 78.58° ± 0.69°. The effect of unequal sensitivity decay for the OPC can be compensated in the software by

taking into account the measured sensitivity decay of the system. This compensation resulted in a retardance value of the QWP to be 84.34°± 0.35° which is in closer agreement with the retardance value (84.17° ± 0.04°) obtained using our approach. It should be noted here that this software correction will not be that effective for scattering samples as the unmatched noise properties as a function of depth for the two polarization channels would introduce error in retardation calculations.

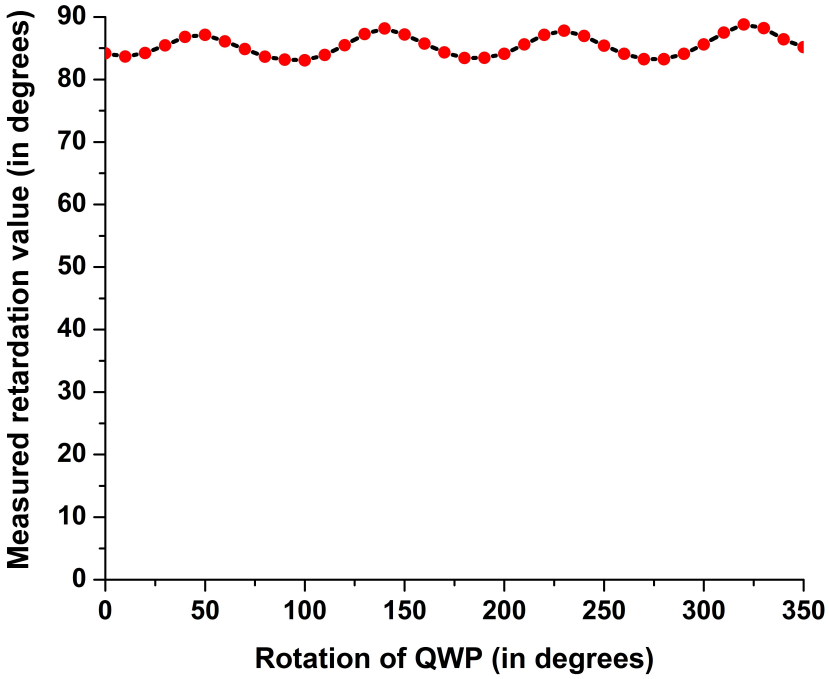

Figure 2.4 *Measured retardation of a QWP using equal and opposite phase shifting for OPC. Red dots show the experimental points while the black line joins them.*

2.3 Utilization of SD-PSOCT setup for *ex-vivo* oral tissue imaging

In this section, we show the use of the developed SD-PSOCT setup for the differentiation of normal and malignant mandibular tissue samples. Measurements were made on epithelium thickness, decay constant of the A-scan intensity profile and phase retardance

in *ex-vivo* human oral mandibular tissue samples, and results indicate that monitoring tissue retardance allows better differentiation of normal and malignant tissues.

2.3.1 Motivation of the work

Oral cancer continues to grow at an alarming rate in Indian subcontinent due to unhealthy habits like consumption of tobacco and pan masala [108]. While early screening is beneficial not only in terms of treatment cost and patient comfort and management, it also leads to better survival rates. Statistics reveal that while the five year survival rate for early stage oral cancer is more than 80%, it drops to about 20% in late stage disease. At present, the only definitive method for determining cancer is histopathological examination of tissue biopsied from the suspected site. Biopsy is not an ideal screening tool because it is invasive and subject to random sampling errors. Owing to their non-invasiveness and high resolution, optical techniques are emerging as particularly well suited for non-invasive screening of oral cancers. OCT is one such high resolution optical imaging modality that provides depth resolved noninvasive imaging of tissue morphology [1-4]. Previous studies reveal that careful examination of the OCT intensity images can help in identification of premalignant disorders and early cancers [39,40,109,110]. The most commonly studied parameters for identification were the changes in epithelium (EP) thickness, the decay constant of the axial scan (A-scan) profile and the larger spatial variation of the OCT intensity signal from dysplastic regions arising due to variations of cell size, shape, nucleus size and cellular distribution.

It is known that most early cancers arise in epithelial tissue and are associated with alterations in both epithelial cells and stroma [111,112]. Since the main scatterers in the stroma are collagen fibers which are birefringent, neoplastic changes are expected to lead to changes in the polarization parameters of the tissue. Indeed, previously done measurement of the polarization parameters (linear retardance, diattenuation and depolarization) of normal and malignant tissue from human oral cavity and breast show

that the observed differences in these parameters were consistent with the changes expected in the collagen structure in these tissues [113]. Therefore, measurement of tissue birefringence should provide additional diagnostic information. To the best of our knowledge, there are only two reports on the use of PSOCT for retardance imaging in oral tissue [114,115]. While Yoon et al [114] showed the higher birefringence of the normal buccal mucosa as compared to the normal tongue tissue; Lee et al [115] showed higher birefringence of submucosal fibrosis lesion as compared to the adjoining normal looking mucosa. While PSOCT has provided better discrimination of tissue pathology in breast and ovarian tissues [116-118], its use for screening of oral cancers has not yet been evaluated.

2.3.2 Materials and methods

Remnant, de-identified and formalin (10%) fixed oral mandibular specimens (8 in number) used in this work were obtained from the surgical pathology section of Sri Aurobindo Medical College & P.G Institute Indore. The tissue excision and handling procedure was in accordance with the Institutional Review Board at Sri Aurobindo Medical College & PG Institute, Indore and written informed consent was obtained from the patients prior to tissue excision. Each tissue sample measured approximately 15 mm in length, 5 mm in breadth and 4mm in thickness. After performing PSOCT imaging on a number of sites on these samples, they were dehydrated in graded ethyl alcohol, processed for standard histological procedures, embedded in paraffin and sectioned into consecutive sequences at 5 μm intervals. Two regions of each sample corresponding to the regions where OCT imaging was carried out were selected for sectioning. The deparafinized tissue sections from these regions were stained with hematoxylin and eosin (HE) followed by light microscopy for evaluation. From each HE stained sample, ten zones were randomly selected and evaluated for thickness measurement of the epithelial layer and lamina propia by means of a calibrated ocular on a light microscope (Olympus, IX 70) at 40X

magnification. A pathologist at Sri Aurobindo Medical College & P.G Institute Indore who was blinded to the study performed the diagnosis.

To detect the presence of collagen fibers in lamina propia and submucosal layers of tissues, Masson's Trichrome (MT) staining was carried out. In each MT stained sample, imaged at 400X magnification, 10 regions were selected and in each micrograph, the density of collagen fibers was graded according to the following scale:1=few collagen fibers, 2=few and partially dispersed collagen fibers, 3=few and fully spread collagen fibers, and 4=dense collagen fibers [119]. Two individuals who were blinded to the study scored for collagen density. Statistical data were analyzed and expressed as mean ± standard deviation (SD). Statistical comparison between means was carried out using Student's t-test. The regression coefficient 'R^2' from the linear regression analysis was used to quantify the correlation between the different parameters. $p<0.05$ were considered significant.

2.3.3 Measurements on oral tissue samples

The OCT intensity images and HE stained images for tissue sites belonging to normal, epithelial hyperplasia (EH), mild dysplasia (MD) and squamous cell carcinoma (SCC) classes are shown in Fig. 2.5(a-d) and 2.5(e-h) respectively. Well defined layered structure is seen in the intensity image of a normal tissue site (Fig. 2.5a). The top highly reflecting layer (marked by white arrow) corresponds to stratum corneum (SC) which is followed by a thin epithelium (EP, marked by double sided arrow). The comparatively higher scattering layer that lies below the epithelium is known as lamina propia (LP). The SC, EP and LP layers can also be clearly differentiated in the HE stained image of normal tissue (Fig. 2.5e). In the hyperplastic tissue (Fig. 2.5b and Fig. 2.5f) the epithelial ridges (shown by white arrows in Fig. 2.5b) can be seen in the EP layer which are indicative of sub-epithelial inflammation. The EP layer gets thickened in the case of mild dysplasia (Fig 2.5c), and the basement membrane layer (shown by black dashed line) which

separates the EP and LP layers can still be seen in most part of the imaged region. The increased EP thickness and loss of differentiation between LP and EP in the dotted trapezium region by can also be confirmed from the corresponding HE stained section (Fig. 2.5g), indicative of tissue transformation to malignant state [120]. In the case of SCC tissue, the distinction between LP and EP layers is completely lost [120]. For a better visibility of Figures 2.5-2.7, all noise above the tissue surface was equated to a small constant value in OCT intensity images and to 45° in retardance images. Since the region above the tissue surface does not contain any useful data, these operations do not interfere with generation of intensity or retardance images [99].

First, we measured the EP thickness and the A-scan decay constant to quantify the changes in tissue sites progressing from normal to cancerous state. For these measurements, we performed an average of 10 A-scans. In order to avoid the effect of high intensity specular reflections from the air-tissue interface on the measurement of decay constant, a depth range of 25 to 700 μm below this interface was used for exponential fitting. The EP thickness was measured to be ~ 100 μm for normal tissue. EP thickness and decay constant were not well defined in epithelial hyperplasia tissue because of the formation of epithelial ridges which result in large spatial variation in EP. The EP gets thickened and was measured to be ~ 250 μm in mild dysplasia. Because of complete loss of distinction between the EP and LP layers in SCC, the EP thickness could not be measured. The decay constants for the normal, mild dysplasia and SCC tissues were measured to be 0.0026 μm^{-1}, 0.0023 μm^{-1} and 0.0015 μm^{-1}, respectively. The observed decrease in the decay constant for cancerous tissue sites is consistent with the previous reports [120].

Figures 2.5(i-l) and 2.5(m-p) show the retardation images and MT stained images, respectively, corresponding to Fig. 2.5(a-d). The well defined banded structure in the retardation image for a normal tissue (Fig. 2.5i) is indicative of the presence of organized

collagen fibers running parallel to the EP surface. The presence of organized collagen is also confirmed from the MT stained image (Fig. 2.5m). The increased inflammation in the epithelial hyperplasia stage causes some disorganization of collagen fibers resulting in disturbances in collagen ordering and hence the banding pattern (Fig. 2.5j). The localized increase in the collagen density (Fig. 2.5n) is indicative of local invasion during epithelial cell migration at the advancing edge of tumor where the tumor cells realign the collagenous matrix to facilitate local invasion [121]. Significant reduction in birefringence is observed in regions of increased epithelium thickness (Fig. 2.5k) in mild dysplasia. The conversion to SCC is accompanied by a complete loss of birefringence (Fig. 2.5l).

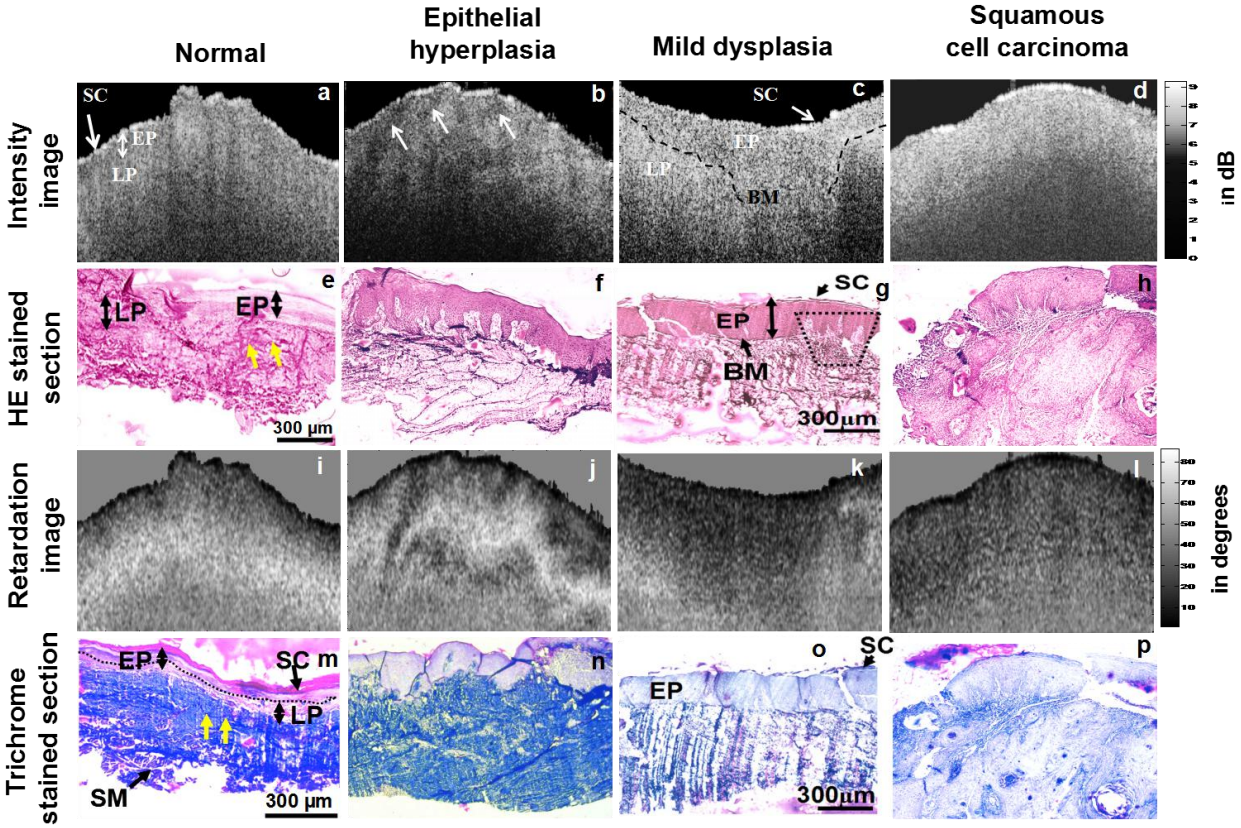

Figure 2.5 *OCT intensity images (a, b, c, d); micrographs of HE-stained section (e, f, g, h); retardation images (i, j, k, l), and micrographs of trichrome-stained section (m, n, o, p) for normal, epithelial hyperplasia, mild dysplasia, and squamous cell carcinoma tissue. SC Stratum corneum, EP Epithelium, BM Basement membrane, LP Lamina propia, SM Submucosa. PSOCT image dimensions: 2 mm (H) × 1 mm (V). Yellow arrows indicate collagen fibers, dashed trapezium shows region with loss of basement membrane.*

Tissue birefringence is another important parameter that was measured to quantify the changes in tissue sites progressing from normal to cancerous state. Linear fitting for the rising part of the first band in the retardation profile (averaged over 10 adjacent A-scans) was done to measure the phase retardation values. The average slope of the linear fit for normal, mild dysplasia and SCC tissues was 0.10 ° μm^{-1}, 0.06 ° μm^{-1} and 0.02 ° μm^{-1}, respectively. It is pertinent to note here that while there is only a factor of 1.3 reduction in the decay constant for a SCC tissue as compared to normal tissue, the birefringence is reduced by a factor of 5. This clearly suggests that tissue birefringence can help in better identification of tissue pathology.

Fig. 2.6 shows the OCT intensity image, retardation image and a trichrome stained image, respectively, for an oral lesion with submucosal fibrosis (SMF). While the left part of the image appears to be normal, the right part has SMF. The broad white streaks in the intensity image (Fig. 2.6a) for SMF are probably due to the thick fibrous collagen bands characteristic of fibrosis [122]. The corresponding retardance image (Fig. 2.6b) also shows the increase in banding pattern owing to increased collagen levels in fibrosis. Thick dense ordering of collagen fibers (yellow arrows) is also seen in the corresponding trichrome stained image (Fig. 2.6c), suggestive of increased collagen levels. The increased collagen levels in SMF can be attributed to increased collagen synthesis and decreased collagen degradation [122]. The phase retardance was measured to be 0.24 ° μm^{-1} for SMF tissue sites.

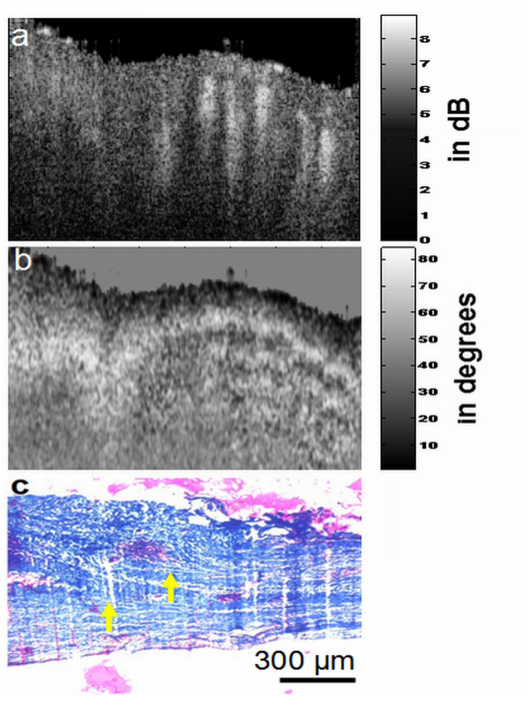

***Figure* 2.6** *OCT intensity image (a), retardation image (b), and micrograph of trichrome-stained section (c) for an oral submucosal fibrosis lesion. PSOCT image dimensions: 2 mm (H) × 1 mm (V). Yellow arrows indicate collagen fibers. Scale bar in trichrome-stained image: 300 µm.*

For the boundary regions between normal and cancerous tissue, the OCT intensity and corresponding retardation images are shown in Fig. 2.7(a,c) and Fig. 2.7(b,d) respectively. The normal and cancerous regions are marked by red dashed and blue dotted rectangles respectively (Fig. 2.7 b & d) in the retardation images. It can be seen that as we move towards the cancerous region, the epithelium gets thickened (Fig. 2.7a) accompanied by loss of birefringence (Fig. 2.7b). The basement membrane is shown by black dashed line in Fig. 2.7a. The HE stained section (Fig. 2.7e) confirms the thickening of EP and loss of basement membrane. While the decay constant was measured to be 0.0030 μm^{-1} and 0.0021 μm^{-1} for the normal and cancerous region, the phase retardance was measured to be 0.16 ° μm^{-1} and 0.05 ° μm^{-1} for the normal and cancerous region respectively. It can easily be seen that as one moves from normal to cancerous region, a much larger change is observed in tissue birefringence as compared to the change in intensity decay constant. This suggests that monitoring tissue birefringence can help in better identification of cancerous lesion margins. The decrease in collagen fibers in the cancerous region is also seen in the trichrome stained image (Fig. 2.7f). These observations suggest disorganization of collagen matrix possibly due to collagen fiber proteolysis assisted by matrix metalloproteases during cancer progression and metastasis [121,123]. In some studies, the relationship between the degree of interstitial collagen deposition at the invading edge of the tumor and the clinical and pathological findings in SCC has been examined. It has been observed that regions with scanty interstitial collagen in biopsy specimens from edge of invading SCC tend to have highly malignant characteristics [124].

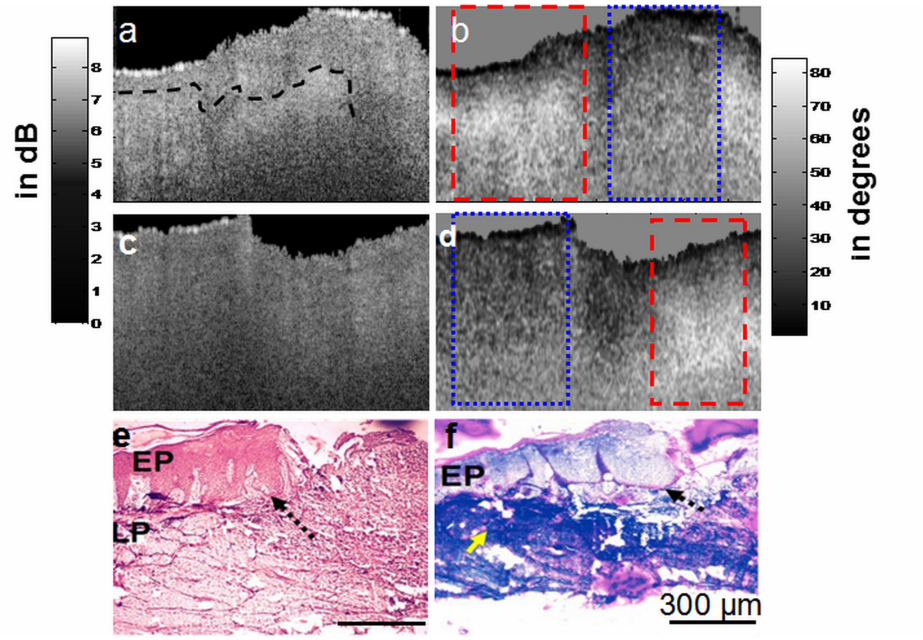

***Figure* 2.7** *OCT intensity (a, c) and retardation (b, d) images along the boundary of cancerous lesion. Normal and cancerous regions are marked by red dashed and blue dotted rectangles, respectively, in retardation images. Representative micrographs of HE-stained section (e) and trichrome-stained section (f) for the boundary region. Dashed arrows: region beyond which there is loss of BM. Yellow arrow: Collagen fibers. Scale bar in (e, f): 300 µm.*

In order to observe the site to site variation in the retardance measurements, PSOCT imaging was carried out on 10 tissue sites of each pathological class, namely; SCC, mild dysplasia, normal and submucosal fibrosis. Further, collagen density scoring was carried out for equal number of MT stained regions of each pathological class. The measured phase retardation values and the corresponding collagen density scores for these groups are plotted in Fig. 2.8. The birefringence of normal tissue is observed to be much higher (~ 4 times, $p<0.001$) as compared to SCC. Also, a positive linear correlation ($R^2 \sim 0.94$, $p=0.009$) between phase retardation and collagen density score suggests that phase retardance can serve as good indicator for the different pathologies of oral mandibular region.

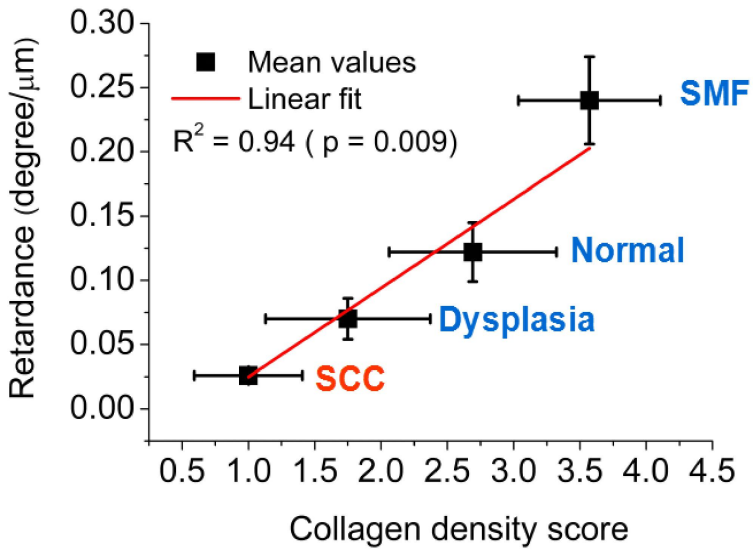

Figure 2.8 *Regression plot for retardance and collagen density score as assessed by PSOCT and MT staining, respectively, for SCC, mild dysplasia, normal, and submucosal fibrosis (SMF) tissue. The data represent mean ± SD for these groups.*

These observations strongly suggest that monitoring tissue birefringence alongwith backscattered intensity can help in better detection of oral tissue pathology and delineation of cancerous lesions. However, the relatively small sample size of this study and intra-sample heterogeneity in collagen density as well as retardance values calls for more studies with larger number of samples for better establishment of observed results.

2.4 Conclusions

To conclude, we have developed a simple, single camera based approach for spectral domain polarization sensitive measurement where both the orthogonal polarization channels see all the pixels and experience identical depth dependent sensitivity profile for the orthogonal polarization channels without making use of any software based correction. Further, we made use of the developed SD-PSOCT setup for *ex-vivo* imaging of human oral tissue samples. Measurements on EP thickness, decay constant of A-scan profile and phase retardance were carried out and compared with histopathological (HE and MT staining) measurements. The results obtained suggest that compared to the use of

differences in EP thickness and the decay constant of A-scan intensity profile, measurement of tissue birefringence provides more sensitive monitoring of the transformation of oral cavity tissue from normal towards frank cancer.

Chapter 3

Development of Doppler OCT setups for flow measurements

In this Chapter, we describe the development of phase resolved Doppler OCT (PRDOCT) setups for flow imaging. Single beam PRDOCT system provides only the axial velocity component along the probe beam. Since the vessel orientation is unknown, absolute velocity cannot be recovered with single beam measurements. We therefore developed multibeam (dual and three beam) DOCT setups that allow determination of absolute flow velocity. These setups were used to measure flow through phantom, and the experimental measurements showed good correlation with the set flow velocities.

Work discussed in this chapter has resulted in the following publications:

1. " Absolute velocity measurement using three beam spectral domain Doppler optical coherence tomography", **P. Sharma**, Y. Verma, S. Kumar, P. K. Gupta, *Applied Physics B*, **2015**, 120, 539–543.
2. " Single detector-based absolute velocity measurement using spectral domain Doppler optical coherence tomography ", S. Kumar, Y. Verma, **P. Sharma**, R. Shrimali, P. K. Gupta, *Applied Physics B*, **2014**, 117, 395-399.

3.1 Introduction to single beam phase resolved Doppler OCT

Flow measurements require measurement of the Doppler frequency shift. As Doppler frequency is related to the phase change of the recorded interferogram, one requires system with high phase stability for flow measurements. Since SDOCT approach avoids scanning of reference mirror to obtain depth information, it provides better phase stability as compared to TDOCT and is better suited for phase resolved measurements required for measurement of flow velocity. As already discussed in Chapter 1, the phase difference between adjacent A-scans ($\Delta\Phi$) is used to estimate the velocity using the expression

$$V = \frac{\lambda_0 \Delta\Phi}{4\pi n \Delta T \cos\theta}$$

Here, V is the flow velocity, λ_0 is the central wavelength of light source used, $\Delta\Phi$ is the phase difference between adjacent A-scans, n is tissue refractive index, ΔT is the time between adjacent A-scans and θ is the Doppler angle (the angle between flow direction and direction of incident beam). However, it must be noted that single beam measurements provide only the axial velocity component and prior knowledge of Doppler angle is required to retrieve absolute flow velocity.

3.2 Introduction to dual beam DOCT

As seen in the previous section, conventional DOCT that uses a single probe beam can provide absolute velocity only if the Doppler angle (angle between the flow direction and the incident beam) is known. This is generally not possible in biological tissues where the blood vessels are surrounded by turbid tissue. Here, one requires simultaneous probing of the same spatial location in the sample with two or more beams coming from different incidence angles to measure absolute velocity. Probing same spatial location with two beams provides the velocity component in the plane containing two probe beams. Ambiguity in the third dimension remains and can be addressed by taking multi beam measurements or by rotating the two probe beams across the optic axis [125,126].

Pederson et al demonstrated a dual beam approach by inserting a glass plate in one half of the sample beam for generating the two angularly displaced probe beams [127]. These beams had an optical path delay determined by the thickness of the glass plate. A major issue with this path length encoded scheme is the presence of a third 'cross-talk' image in addition to the two images corresponding to the two probe beams retracing their original paths after scattering from the tissue. This cross-talk image arises due to the first probe beam being scattered along the path of the second probe beam and vice-versa. This cross-talk image reduces the depth of the tissue that can be imaged with a given setup. This is of major concern with spectral domain OCT systems where the imaging range of the setup is already limited by the spectral resolution of the spectrometer [101], thereby limiting the system applicability to thin samples with depth at least three times smaller than the imaging range of the system [128]. Furthermore, SDOCT systems suffer from depth dependent sensitivity decay which degrades phase measurement accuracy and hence absolute velocity estimation [129].

The cross-talk image can be avoided by using two separate interferometers and detection units that share the same sample and reference arms but have an optical delay longer than the imaging range of the systems [130]. However this makes the system costly and bulky. Werkmeister et al [131] and Dave et al [132] have investigated the use of two orthogonally polarized beams to avoid cross-talk image. However the requirement of two separate detectors for the two orthogonal polarization channels complicates the system alignment and synchronization for phase sensitive detection.

We have developed a simple single detector based dual beam spectral domain PRDOCT setup. Introduction of a beam displacer in the sample arm of the interferometer to generate two orthogonal polarization beams helps avoid the problem of the cross-talk image. The issue of phase errors resulting from use of separate spectrometers for the measurement of orthogonal polarization channels is also avoided.

3.2.1 System description

A schematic of the dual beam PRDOCT set up for absolute flow velocity measurement is shown in Fig. 3.1. The fiber based Michelson interferometer was illuminated with a 15 mW superluminescent diode source with center wavelength 840 nm and 40 nm bandwidth. A 50:50 single mode fiber coupler splits the incoming source beam into reference and sample arms. A beam displacer (BD) was introduced in the sample arm to split the input beam into two orthogonally polarized parallel beams with ~ 4 mm spatial shift between them. The horizontally polarized beam labeled as '1' emerges straight while the vertically polarized beam labeled as '2' emerges at a spatial offset of 4 mm from the entrance direction. After reflecting off the galvoscanner, these beams are focused on the sample through a focusing lens of focal length 50 mm. To avoid the overlapping of the two orthogonal polarization images in depth domain, a glass plate (GP) is inserted in the beam path of vertically polarized probe beam. The thickness of GP is suitably chosen to ensure that the resultant optical path delay between the two orthogonal polarization probe beams (~ 1.2 mm) remains larger than the imaging depth of the sample glass tube while still remaining smaller than the maximum imaging depth range of SDOCT setup.

The reference arm comprises of a reference mirror which reflects the light back to the interferometer. Additionally, in order to minimize the dispersion mismatch arising due to the use of BD in sample arm, a glass window (GW) of appropriate thickness is incorporated. The light beams reflected from the two arms of the interferometer recombine and generate interference fringes which are encoded in depth and are detected by a spectrometer. The spectrometer comprises of a 50 mm focal length lens to collimate the input beam, followed by a volume phase transmission holographic grating (1200 lines/mm, Wasatch Photonics, UT, USA) which disperses the collimated beam. A 150 mm focal length imaging lens spatially Fourier transforms the dispersed beam onto a line scan camera (1024 pixels, 14 μm pixel size, Atmel, CA, USA). The line scan camera is

operated at 10 kHz readout rate which corresponds to integration time (ΔT) of 100 μs. A PCI-1428 (National Instruments, TX, USA) camera link image acquisition board was used to digitize the data from the line scan camera.

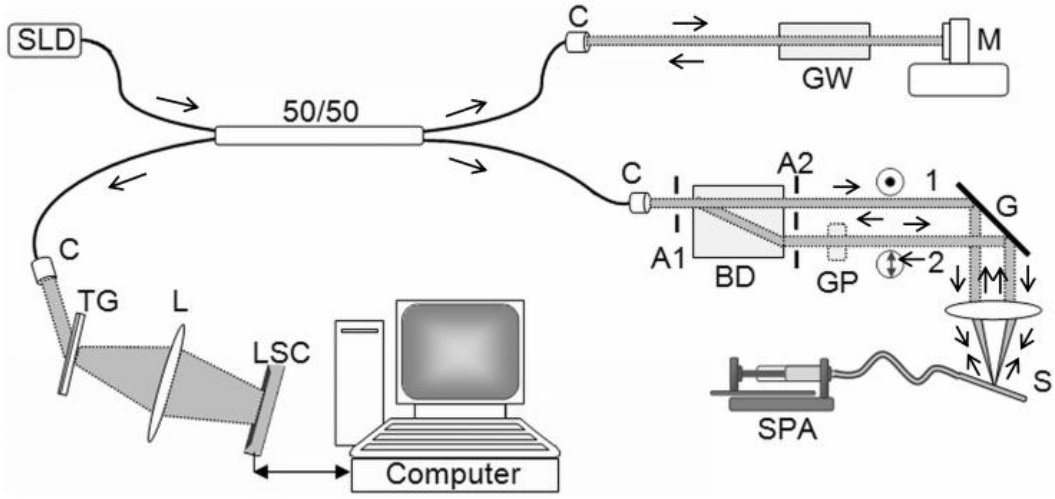

Figure 3.1 *Schematic of dual beam PRDOCT setup. SLD-Superluminescent diode, C-Collimating lens, L-Lens, GW-Glass window, M-Mirror, A1 and A2-Apertures, BD-Beam displacer, GP-Glass plate, G-Galvoscanner, SPA-Syringe pump assembly, S-Sample, TG-Transmission grating, LSC-Line scan camera. The beams labelled as '1' and '2' are orthogonal linearly polarized beams with horizontal and vertical polarization respectively.*

NI-IMAQ software is used under Labview™ environment for data acquisition and subsequent processing. A dual waveform function generator was employed to generate a saw tooth waveform synchronous with a trigger signal. While the sawtooth waveform was used to drive the galvoscanner for lateral scanning of the probe beams on the sample, the trigger signal was used to trigger the data acquisition card in synchronization with the saw tooth waveform. The interferometric data collected by the spectrometer was evenly sampled in k-space by means of cubic spline interpolation. The FFT of the resampled interference spectrum generates the depth resolved intensity (structural) and phase images. The dual beam DOCT system features axial and lateral resolutions of ~10 μm and 50 μm respectively, with a maximum imaging range of ~2 mm (limited by the spectral resolution

(~0.09 nm) of the spectrometer). The measured sensitivity (SNR) of the system for the two probe beams are 95 dB and 89 dB respectively. The difference in sensitivity is because the two images are present at different depths from the zero delay position, and spectral domain systems suffer from depth dependent sensitivity decay [101].

3.2.2 Methodology of dual beam approach

The proposed scheme makes use of a BD to avoid the problem of cross-talk image. Fig. 3.2 shows propagation of incident horizontally polarized (path 1 i.e. ABC) and vertically polarized beams (path 2 i.e. ADC) and their focusing on the sample. As seen in Fig. 3.2a, only the light that gets scattered from the sample and retraces its incidence path (that is probe beam 1, that reaches the sample by following the path ABC being scattered back along CBA and similarly the probe beam 2 following the path ADC being scattered back along CDA) passes through the aperture A1 placed before the BD and recombines. The scattered light which follows the cross path (probe beam 1 that reaches the sample by following the path ABC being scattered back along CDE (Fig. 3.2b) and similarly probe beam 2 that reaches the sample by following the path ADC being scattered along CBF) gets blocked by the aperture A1 (Fig. 3.2c). Another aperture A2 was also placed after the BD for efficient rejection of the cross path light. The two delay encoded phase images were used for the measurement of the velocity component along their respective beam directions. The flow velocity vector was determined by making use of the phase difference between adjacent A-scans in each of these phase images. An oversampling factor of 10 was used to minimize the phase de-correlation between adjacent A-scans due to sample inhomogeneity.

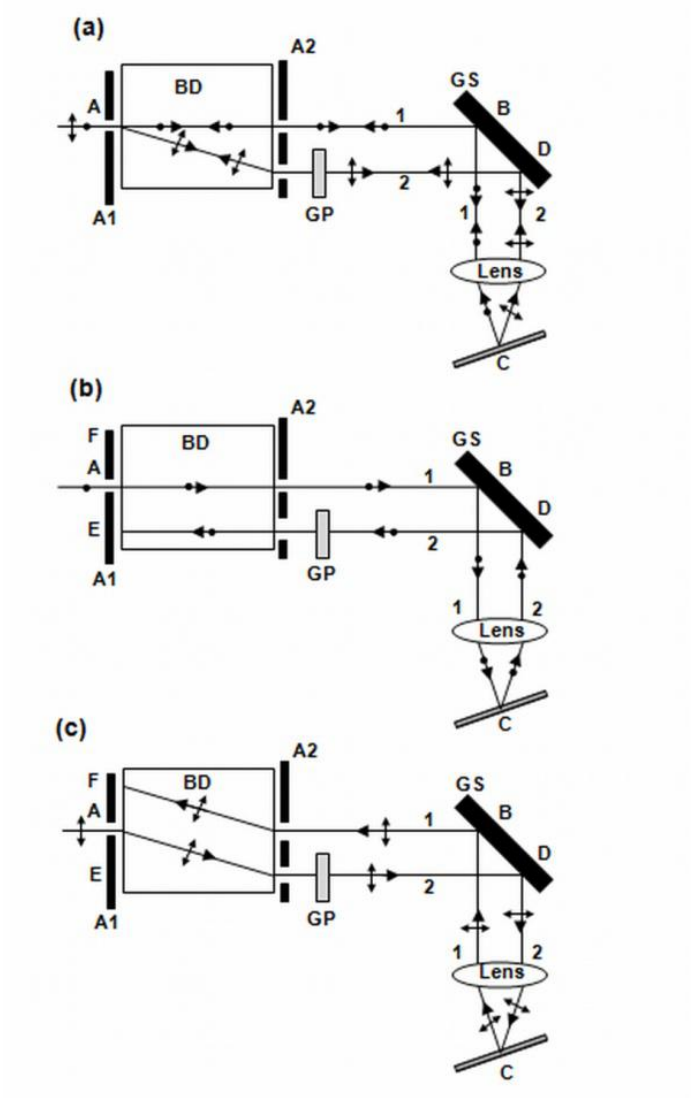

Figure 3.2 *Propagation of orthogonal linearly polarized probe beams. The horizontally and vertically linear polarization components are shown in dot and double arrows respectively. Beams retracing their original paths after scattering (a) A-B-C-B-A or A-D-C-D-A will get through aperture A1, while the cross-talk beams following A-B-C-D-E (b) or A-D-C-B-F (c) will get blocked by aperture A1. GS: Galvoscanner, BD: Beam displacer, GP: Glass plate.*

Fig. 3.3 shows the focusing geometry of the orthogonally polarized probe beams. The angle between the two beams ($\Delta\alpha$) probing the same spatial location of the sample was determined by $2*\arctan(\Delta x/(2f))$, where Δx and f refer to the spatial offset between the two beams and the focal length of the focusing lens respectively. For our setup with Δx and f as 4 mm and 50 mm respectively, $\Delta\alpha$ comes out to be ~ 4.5º. The Doppler angles (α_1

and α_2) formed by the two incident beams with the direction of flow, and absolute velocity (V) can be determined by the following equations [127].

$$v_1 = d\phi_1 . \frac{\lambda}{4\pi n \Delta T \cos\alpha_1}, \quad v_2 = d\phi_2 . \frac{\lambda}{4\pi n \Delta T \cos\alpha_2} \qquad \text{..... (3.1)}$$

$$\alpha_2 = \pi - \Delta\alpha - \alpha_1 \qquad \text{..... (3.2)}$$

$$V = \frac{v_1}{\cos\alpha_1} = \frac{v_2}{\cos\alpha_2} \qquad \text{..... (3.3)}$$

where $d\phi_1$ and $d\phi_2$ are the phase change for the two images.

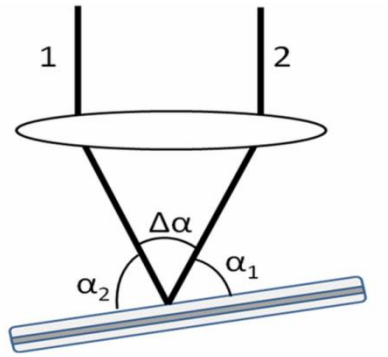

Figure 3.3 *Focusing geometry of the horizontally (marked as 1) and vertically (marked as 2) polarized probe beams. α_1 and α_2 are the angle between the flow direction and incident probe beams. $\Delta\alpha$ is the angle between the two probe beams.*

3.2.3 Results

The scheme was validated by performing absolute velocity measurement in a flow phantom. As shown in Fig. 3.1, a syringe and precision DC translation stage were used to flow 1% Intralipid solution in water through a glass tube with 0.5 mm inner diameter. Figures 3.4a and 3.4b show the structural and phase images of the intralipid flow phantom

formed by the two orthogonal polarization beams for a given flow velocity. Velocity components v_1 and v_2 were calculated by parabolic fitting of the measured axial velocity distribution profiles for each beam as shown in Fig. 3.4c. These are then used to calculate Doppler angles (α_1 and α_2) and the absolute velocity (V) using equations 3.1 to 3.3.

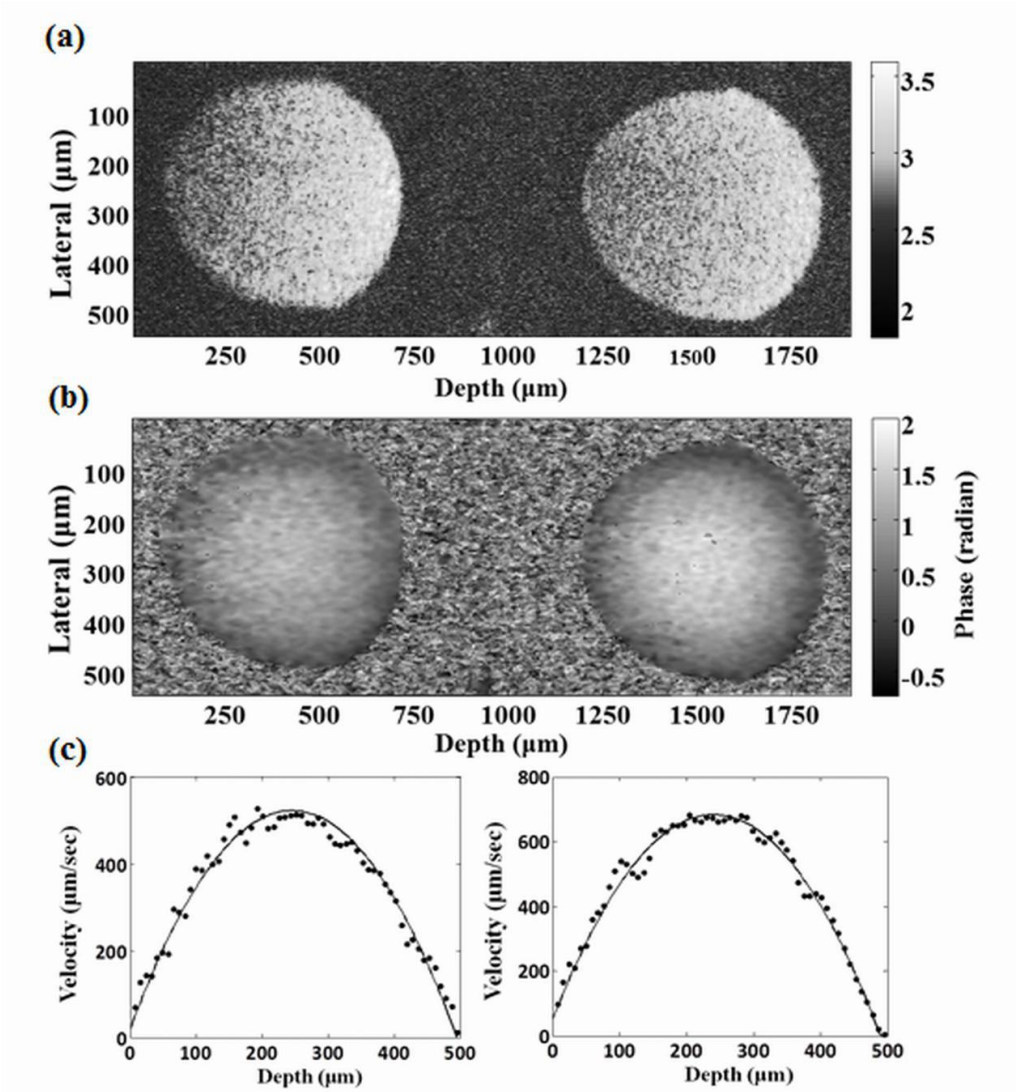

Figure 3.4 *(a) The structural images corresponding to the two probe beams. (b) The phase resolved DOCT images corresponding to the two beams. (c) Velocity distributions along each of them. The points represent the experimentally obtained data while the solid curves represent parabolic fit to the data.*

Fig. 3.5a shows good correlation between the set velocities and the absolute velocities estimated using the approach. The average root mean square (rms) error in the measured value for the velocity was ~0.05 mm/s. Fig. 3.5b shows the variation in the measured

value for the absolute velocity as a function of the tilt of the glass tube (having fixed flow rate of 0.5 mm/s) with respect to the horizontal. The fact that the measured velocity is indeed the absolute velocity is validated by the observed angular invariance of the measured velocity. In the above discussion, the estimated velocity is referred to as the absolute velocity as the flow phantom was aligned in the plane of the two probe beams. If the flow phantom is out of plane, determination of absolute flow velocity using dual beams would require rotation of the plane containing the probe beams.

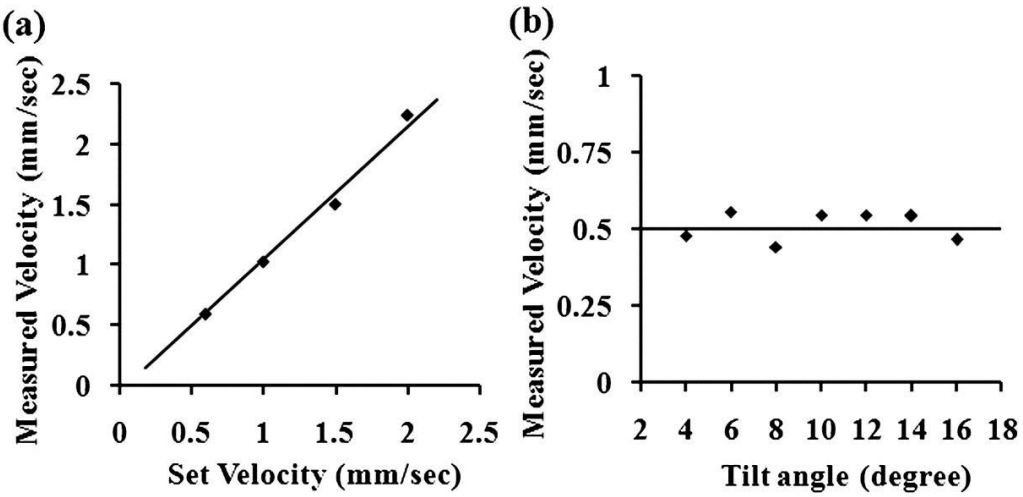

Figure 3.5 *(a) Correlation between set and measured flow velocities. (b) Measured absolute velocity for different tilt angles of tube with respect to the horizontal.*

3.3 Introduction to three beam DOCT

As already seen in previous sections, single beam phase resolved DOCT measurements can provide only the axial velocity component [83]. Absolute velocity measurement using such a setup requires prior information on the Doppler angle, which is generally not possible. Absolute velocity measurement using the dual beam approach requires aligning the plane of the two beams with the orientation of the vessel, making the approach labor intensive and time consuming. Another way to determine the vessel orientation is to acquire a 3D dataset of the sample and then make use of two cross-sectional B-frames

separated by a known distance [133]. However, the accuracy of the measurement of the Doppler angle is limited by the unavoidable motion artifacts in live samples, and the need to acquire multiple B-frames makes this approach labor intensive and time consuming. Determination of absolute velocity in a single B-frame measurement without prior knowledge of flow direction requires use of three or more probe beams that probe a single location in the sample from different incidence angles. A previously reported three beam based absolute flow velocity measurement set up makes use of depth encoding to get the corresponding images [125]. The achievable imaging depth in the sample is severely limited in this case because the five images (three images corresponding to the three probe beams and two additional cross-talk images corresponding to the cross-coupling paths for the three beams) need to be incorporated within the imaging range of the setup. Because these five images are created at different depths with respect to zero path delay between the reference and the sample arms, they experience different sensitivity. This in turn affects the velocity measurement as the sensitivity decreases with increasing depth of imaging and the minimum measurable phase difference is inversely proportional to square root of the measurement sensitivity [101,129]. One approach to avoid the problem of reducing sensitivity with depth is to make use of vertical cavity surface emitting laser (VCSEL) that offer large coherence lengths (~ 10's of cm) [134]. Another three beam DOCT setup has been reported which incorporates three separate interferometers, one for each probe beam [135]. However using three sources and three spectrometers not only results in higher cost but makes the system complex and alignment sensitive.

In this section, we discuss the development of a three beam spectral domain Doppler optical coherence tomography setup that allows single B-frame based measurement of absolute velocity without prior knowledge of vessel orientation. Use of a beam displacer in the sample arm (to generate two orthogonal polarization beams) coupled with

galvoscanner based phase shifting (to remove complex conjugate mirror artifact) helps avoid the cross-talk images that limit the achievable depth range.

3.3.1 System description

A schematic of the three beam PRDOCT setup for absolute velocity measurement is shown in Fig. 3.6. Here, the dual beam setup was suitably modified to allow three beam measurements. A non-polarizing beam splitter in the sample arm splits the beam into two parts. One of these beams is further split using a beam displacer (BD) into two linear orthogonally polarized parallel beams with ~ 4 mm spatial shift between them. The horizontally polarized beam labelled as '1' emerges straight while the vertically polarized beam labelled as '2' emerges at a spatial offset of 4 mm. The third beam labelled as '3' was directed to the galvoscanner using a pair of additional mirrors. A glass plate (GP) was inserted in the beam path of vertically polarized probe beam to match the optical path of the probe beams 1 and 2. The optical path of probe beam 3 was adjusted such that the optical path delay between probe beam 3 and 1(or 2) is at least twice the imaging range of the setup. This was done to ensure that any cross-coupling between probe beams 3 and 1(or 2) does not contribute to interference signal. These 3 beams were aligned such that they form the three vertices of an equilateral triangle, each vertex being placed at an offset from the pivot axis of the galvoscanner. After reflecting off the galvoscanner these three beams were focussed to a common spot on the sample using a focusing lens of focal length 50 mm (NA=0.012). The angle between any two probe beams was ~4.6°. Fig. 3.7 shows the (A) top (XY plane) and (B) side views of the focusing geometry of the three probe beams on the sample. Here α_1, α_2 and α_3 are the angles between three probe beams and the tube, v is flow velocity vector and v_1, v_2 and v_3 are the velocity components along the three probe beams.

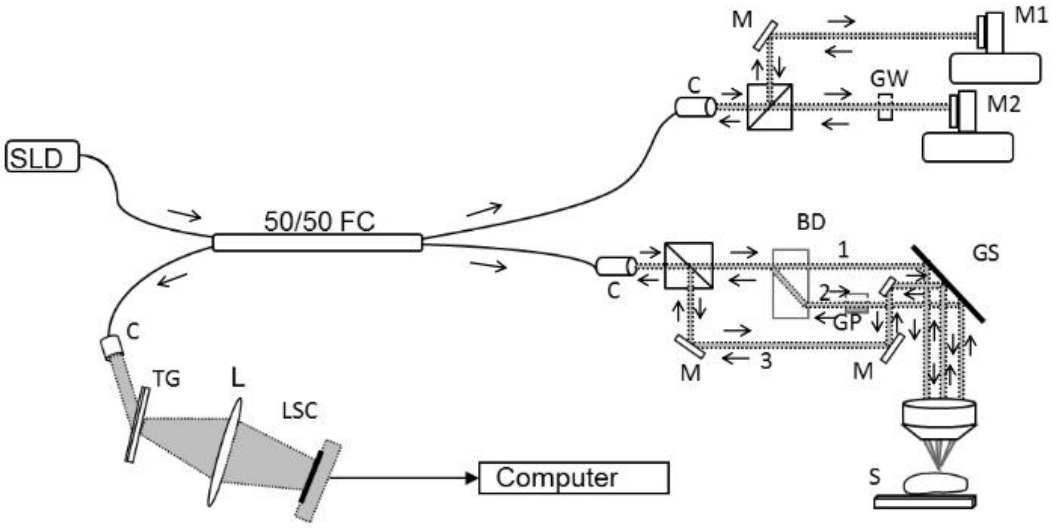

Figure 3.6 *Schematic of three beam PRDOCT setup. SLD-Superluminescent diode, C-Collimating lens, L-Lens, GW-Glass window, FC-Fiber coupler, M,M1,M2-Mirrors, BD-Beam displacer, GP-Glass plate, GS-Galvoscanner, SPA-Syringe pump assembly, TG-Transmission grating, LSC-Line scan camera. Labels 1, 2 and 3 represent the three probe beams.*

Another non-polarizing beam splitter was used in the reference arm to split the beam into two reference beams. One reference beam was path matched to probe beams 1 and 2, while the other was path matched to probe beam 3. To minimize the dispersion mismatch arising due to the use of BD in generation of probe beams 1 and 2, a glass window (GW) of appropriate thickness was incorporated in the corresponding reference beam. The light beams reflected from the reference and the sample arms recombine and generate interference fringes. These delay encoded interference patterns were detected by a spectrometer comprising of a collimating lens (focal length 5 cm), a volume phase holographic transmission grating with 1200 lines/mm, a focusing lens of focal length 15 cm and a line scan camera (Atmel Aviiva, 1024 pixels) operating at 10 kHz line rate [136,137]. These interference spectra were first processed with background subtraction, resampled in k-space and then Fourier transformed to generate the depth resolved intensity and phase images. Further, the phase images corresponding to the three probe

beams were also corrected for the phase shift introduced by the galvoscanner. The axial and lateral resolutions of the three beam PRDOCT setup were ~10 µm and 50 µm respectively, and the sensitivity roll-off was 3dB at a depth of 1 mm. The maximum imaging range was ~4 mm, limited by the spectral resolution (~0.1 nm) of the spectrometer. The measured sensitivity (SNR) of the system was 90 dB, 91 dB and 88 dB for the probe beams 1, 2 and 3 respectively.

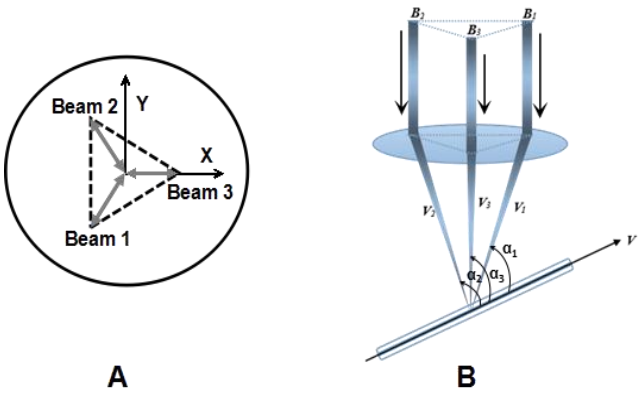

Figure 3.7 *Focusing geometry of three probe beams. (A) Top view and (B) Side view.*

3.3.2 Methodology

To avoid the overlap of the OCT images corresponding to the three probe beams, these images need to be separated in optical path. To achieve this, the galvoscanner induced phase shifting method was incorporated which helps remove the complex conjugate artifacts and doubles the imaging range of the system [107]. As shown in Fig. 3.8 (A), the sample arm of the system was aligned such that the probe beams 1 and 3 were present on one side of the pivot axis of the galvoscanner while probe beam 2 was present on other side of the pivot axis. During lateral scanning, positive phase shifts were introduced for probe beams 1 and 2, while negative phase shifts were introduced for probe beam 3, as shown in Fig. 3.8 (B). The phase shifts introduced in each of the three beams were used to remove the complex conjugate artifact. Hilbert transformation (for a given k along time or

x-axis) and then Fourier transformation along k axis places the images corresponding to probe beams 1 and 3 on one side of the zero delay line while the image for probe beam 2 on opposite side of zero delay line.

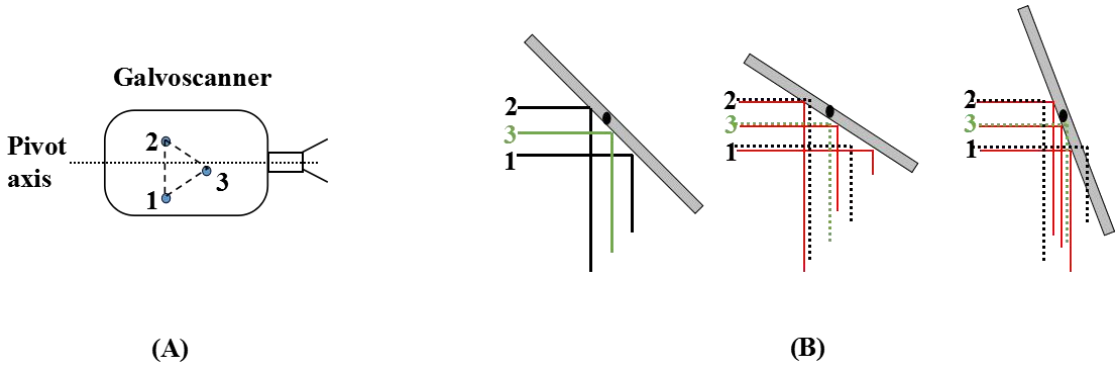

Figure 3.8 *Beam geometry on the galvoscanner. (A) Front view and (B) Side view.*

The optical paths of probe beams 1 and 2 were adjusted such that the corresponding images are placed at equal distances on opposite side of the zero delay line in depth domain. This resulted in identical depth dependent sensitivity variation for the two probe beams (1 and 2). Also the reduction in sensitivity for probe beam 3 due to depth dependent sensitivity decay in SDOCT was partly compensated by an increase in the power for probe beam 3. As already seen, the BD used to generate two orthogonal polarization probe beams (1 and 2) helps avoid the cross-talk image [137]. The optical path of the third probe beam was adjusted such that the corresponding image was separated from the orthogonal polarization images by a distance greater than the achievable imaging depth in the sample. Since the three probe beams make different angles of incidence ($\alpha_{1,2,3}$) with the flow direction, phase difference measurements ($d\phi_{1,2,3}$) for each of the phase images provides the corresponding axial velocity components ($v_{1,2,3}$). By making use of the axial velocity components, the three velocity components ($v_{x,y,z}$) and absolute velocity was determined using the following equations [135]:

$$v_1 = e_{1x}.v_x + e_{1y}.v_y + e_{1z}.v_z = d\phi_1 \frac{\lambda}{4\pi\Delta Tn\cos\alpha_1} \quad \text{..... (3.4)}$$

$$v_2 = e_{2x}.v_x + e_{2y}.v_y + e_{2z}.v_z = d\phi_2 \frac{\lambda}{4\pi\Delta Tn\cos\alpha_2} \quad \text{..... (3.5)}$$

$$v_3 = e_{3x}.v_x + e_{3y}.v_y + e_{3z}.v_z = d\phi_3 \frac{\lambda}{4\pi\Delta Tn\cos\alpha_3} \quad \text{..... (3.6)}$$

3.3.3 Results

The scheme was validated by performing absolute velocity measurements in a flow phantom. A syringe pump was used to flow 1% Intralipid solution in water through a glass tube of 0.5 mm inner diameter. Fig. 3.9 (A, B) shows the intensity and phase resolved DOCT images of the Intralipid flow phantom obtained using the developed approach. Here the glass tube was oriented at 70° with respect to Z axis. The choice of Doppler angle of 70° was made considering the facts that mostly the tissue vasculature is arranged in a horizontal plexus and that Doppler measurements become increasingly erroneous as Doppler angle approaches 90° [126]. Axial velocity components $v_{1,2,3}$ were calculated by parabolic fitting of the measured velocity profiles. These axial velocity components were then used to calculate the flow velocity components $v_{x,y,z}$ along X, Y and Z axis using equations 1 to 3. The measured as well as fitted axial velocity distribution profiles for the three probe beams are shown in Fig. 3.9C. The measured velocity profiles are an average over 10 adjacent A-scans. The experimentally measured velocity was ~7.8 mm/s for a set velocity of 8.5 mm/s.

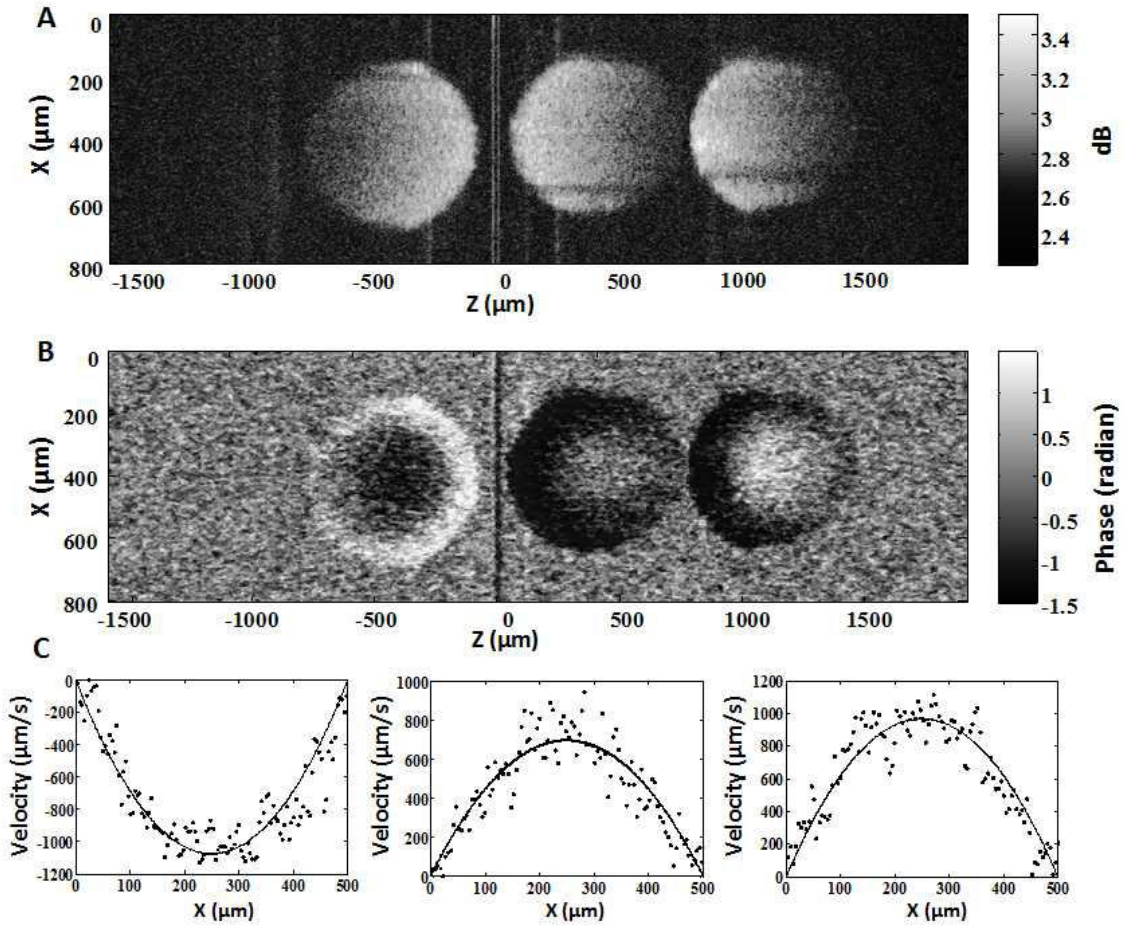

Figure 3.9 *The (A) intensity, (B) phase resolved DOCT images for the three probe beams and (C) axial velocity distributions along each of them. X and Z denote the lateral and axial dimensions respectively. Points represent experimental data while the solid curves represent parabolic fit to the data.*

Fig. 3.10A shows the experimentally measured flow velocities for glass tube oriented at an angle of 70° with respect to Z-axis for different flow velocities set by syringe pump. Good correlation can be seen between the set and experimentally measured velocity values. Fig. 3.10B shows the velocity measurements carried out for different tilt angles of the glass tube with respect to Z-axis (θ) and X-axis (φ). The measured flow velocity of 4.7 ±0.4 mm/s for the different orientations of glass tube matches reasonably well with the set flow velocity of 5.1 mm/s. The dotted lines and solid circles show the expected and measured velocity values and the error bars equal the standard deviation of the

measured velocity values. The deviation between the set and measured velocity could be due to the refraction of the probe beams at the outer surface of the glass tube.

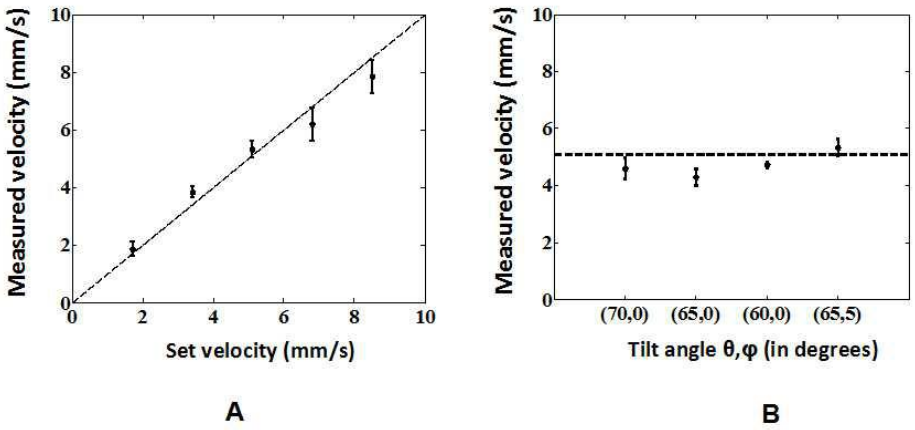

Figure 3.10 *(A) Absolute velocity measurement for different set velocities for a constant tilt angle of tube; (B) Absolute velocity measurement for different tilt angles of the glass tube.*

3.4 Conclusions

To conclude, we have seen that single beam PRDOCT allows measurement of axial flow velocity. However, single beam measurements require prior knowledge of vessel orientation to recover absolute flow velocity which is most often not possible in biological tissues. Recovering the absolute flow velocity then requires simultaneous probing of the sample with two or more beams. We therefore developed dual beam Doppler OCT scheme for velocity measurement that provides absolute velocity measurement in the plane of the two probe beams. This scheme not only allows a single detector based implementation of dual beam spectral domain PRDOCT setup but also helps eliminate the cross-talk image. The approach has been validated by carrying out velocity measurement in a flow phantom. While the dual beam approach provides flow velocity component in the plane of the two beams, absolute velocity measurement without prior knowledge of the vessel orientation or having to rotate the plane of the

probe beams necessitates use of atleast 3 probe beams. In the developed three beam single detector based spectral domain PRDOCT setup, use of phase shifting introduced by the galvoscanner to remove the complex conjugate mirror artifact and the use of beam displacer in the sample arm of the fiber optic interferometer to generate orthogonal polarization beams allows efficient utilization of the achievable depth range and measurement sensitivity of the SDOCT setup for velocity measurement without any cross-talk. The three beam approach has also been validated by measurement of absolute flow velocity in a flow phantom.

Chapter 4

Microvasculature imaging

Arrangement of tissue microvasculature is an important diagnostic parameter for several pathological conditions like diabetic retinopathy, psoriasis, etc which involve microvascular alterations. While DOCT can be used to generate microvascular maps, its dependence on Doppler angle and the high sensitivity of phase measurements to tissue motion results in incomplete noisy microvascular maps. In this Chapter, we discuss different intensity based schemes like correlation mapping and speckle variance imaging which are used for imaging tissue microvasculature. Microvascular visualization using such intensity based schemes is preferable because they are independent of Doppler angle and are comparatively less sensitive to bulk tissue motion. We then describe the development of swept source based SVOCT system for microvascular imaging and its use for monitoring microvascular regeneration in a punch wound created in ear pinna of a diabetic mice. The changes observed in the tissue morphology and vasculature at different time points post wounding are presented.

Work discussed in this chapter has resulted in the following publication:

1. "Feasibility of speckle variance OCT for imaging cutaneous microvasculature regeneration during healing of wounds in diabetic mice", **P. Sharma**, J. Kumawat, S. Kumar, K. Sahu, Y. Verma, P. K. Gupta and K. D. Rao, *Laser Physics*, **2018**, 28, 025601.

4.1 Introduction to microvasculature imaging

It is widely accepted that apart from structural information, information on vascular remodeling can help in more accurate assessment of wound healing [138]. Phase resolved Doppler OCT makes use of the phase shift introduced by flowing blood cells to recover the blood flow velocity [139]. While Doppler OCT can also be used to reconstruct vascular maps, the very fact that it makes use of phase information makes it highly sensitive to bulk motion artifacts [140]. Also, due to angle dependence of the Doppler effect, the sensitivity of measurement is poor in locations like skin where the vasculature is usually arranged in a horizontal plexus perpendicular to the incident probe beam [141]. Recently, various algorithms like correlation mapping OCT, speckle variance OCT, optical micro-angiography, etc have been developed that make use of the fluctuations in the intensity of backscattered light for reconstruction of vascular maps and are less sensitive to motion artifacts, a problem very difficult to avoid in real time imaging scenarios [89,142,143]. Also the insensitivity of these methods to the Doppler angle is an added advantage.

4.2 Intensity based schemes for microvascular imaging

Here, we will discuss two major and widely used intensity based techniques for microvascular imaging, namely correlation mapping OCT and speckle variance OCT.

4.2.1 Correlation mapping OCT

Correlation mapping OCT (CMOCT) is a newly developed technique for visualization of blood vessels by using only the intensity information. Here the cross correlation coefficient is calculated between adjacent B-frames to serve as a measure of de-correlation. Since the vascular portions are more de-correlated than the static regions, this allows enhanced view of tissue microvasculature. Generally two modes of scanning are used. The first one uses a ramp waveform for dense scanning along the C-scan direction

to ensure sufficient correlation between adjacent B-frames. However this makes the system slow and limits its application for real time *in-vivo* imaging. The second one uses a step waveform such that multiple B-scans are acquired at a particular location to ensure sufficient correlation. Here the correlation map is generated from this set of B-frames (acquired at a particular location) and then the scanner moves to next location along the C-scan direction. Taking multiple B-scans at a particular location improves the sensitivity of microvasculature detection. Therefore CMOCT is a magnitude based angiographic technique that provides three dimensional view of tissue microvasculature. The first step in CMOCT is to determine correlation coefficient between two cross-sectional (XZ slices) B-frames I_A and I_B using the expression

$$cmOCT(x,z)=\sum_{p=0}^{M}\sum_{q=0}^{N}\frac{[I_A(x+p,z+q)-\overline{I_A(x,z)}].[I_B(x+p,z+q)-\overline{I_B(x,z)}]}{\sqrt{(I_A(x+p,z+q)-\overline{I_A(x,z)})^2+(I_B(x+p,z+q)-\overline{I_B(x,z)})^2}}$$

..……...…(4.1)

where (M,N) is the grid or kernel size and $\bar{I}$ is the mean intensity value over this grid. Next the kernel is moved across the entire XZ slice and a 2D correlation map is generated. The correlation map has values in the range 0 to ±1 indicating weak and strong correlation [142]. The kernel size is determined by the optimum trade-off between processing time and image quality. Choosing a large kernel size may lead to loss of smaller vessels, whereas choosing a small kernel size will result in a time consuming and noisy correlation map as small variations in intensity will result in de-correlation and appear as false vascular areas. Since the noise regions are also de-correlated, they have correlation values similar to those from vascular regions. Hence the correlation map is masked by an intensity mask such that only the vascular regions remain. The resultant map has values 0 to ±1 where smaller values indicate weak correlation and higher values indicate strong correlation. Since the light backscattered from flow regions exhibits larger fluctuations, it results in weaker correlation between intensity values of adjacent B-frames.

The light backscattered from static regions exhibits strong correlation. Generally, regions with correlation coefficient > 0.6 are considered to be static. The correlation values might be dependent on the temporal separation between B-frames as low time separation may lead to loss of vessels with small flow velocity. Fig. 4.1 shows the processing steps for CMOCT and results obtained in a phantom [142].

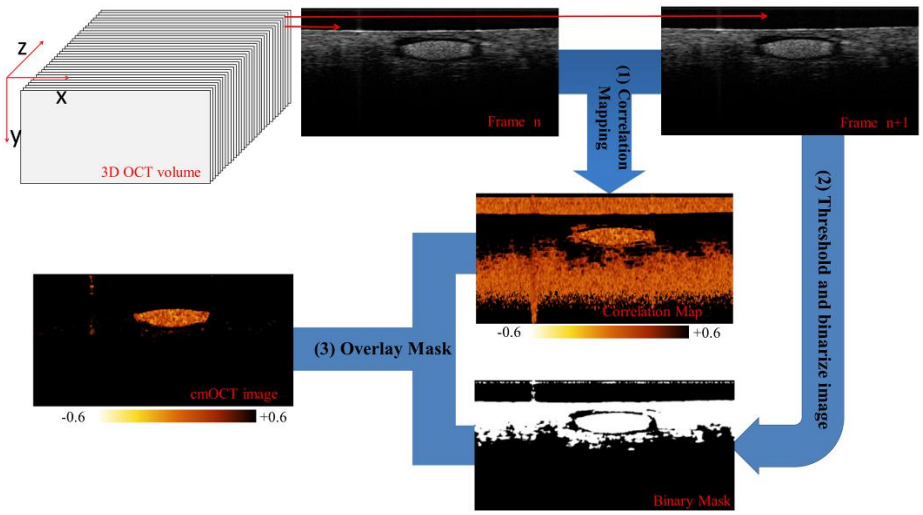

Figure 4.1 *Processing steps for CMOCT algorithm. Higher correlation is shown as darker colour while lower correlation is shown as brighter colour. The figure shows a 200 μm capillary tube containing intralipid solution moving under Brownian motion embedded in excised porcine tissue (reprinted with permission from Biomedical Optics Express [142]).*

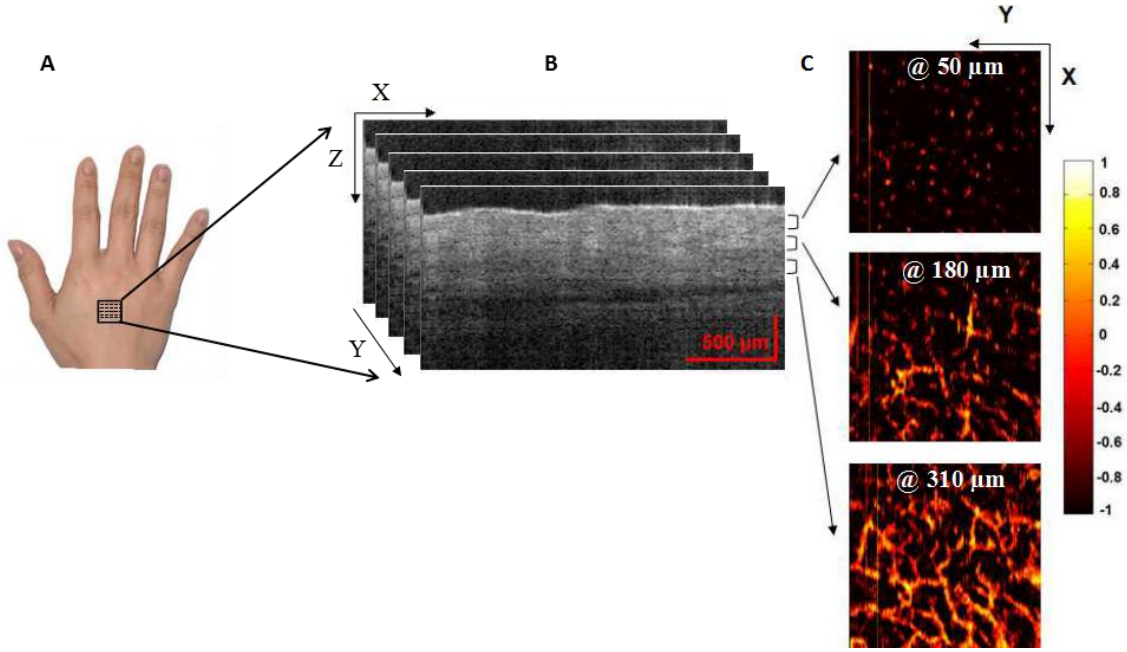

Figure 4.2 *Microvascular imaging of human hand in-vivo using CMOCT. (A) Photograph of the human hand. The imaged area is shown as black square (2 mm x 2mm). (B) Cross-sectional (XZ) OCT images of human hand along dashed lines marked in A. (C) En-face (XY) maximum intensity projections of vasculature at different depths. Image dimensions are 2 mm x 2mm.*

One can also employ full depth imaging in CMOCT by offsetting the probe beam from the pivot of the scanner to gain access to the high sensitivity zone near the zero delay location. To get *en-face* view of microvasculature, maximum intensity projection (MIP) images can be obtained from the 3D correlation volume for different depth sections. CMOCT has been used to image microvasculature in volar forearm, dorsal skin, palm, etc. Fig. 4.2 shows the *in-vivo* microvasculature images obtained from human hand using CMOCT.

4.2.2 Speckle variance OCT

Speckle variance OCT (SVOCT) generates microvasculature maps by statistical analysis of the variation in speckle pattern. As already discussed, phase resolved DOCT suffers from angular dependence and becomes insensitive for small flow velocities in capillaries with Doppler angle approaching 90°. In various cases such as in ocular measurements, the blood vessels are nearly parallel to the surface and hence perpendicular to the incident

beam. Also because of the highly tortuous nature of bold vessels, use of PRDOCT may result in incomplete vascular maps [143]. Since speckle pattern does not depend on Doppler angle, speckle variance OCT overcomes the above drawbacks of PRDOCT. Since the blood is in state of continuous motion, there results a variation in the speckle pattern spatially as well as temporally. In OCT, the cross-sectional data is acquired in a point wise manner and hence the different pixels along B-scan or C-scan direction can be considered as the temporal sampling of the dynamic speckle pattern. The interframe speckle variance image may be generated from the OCT intensity images according to the expression

$$SV_{ijk} = \frac{1}{N}\sum_{i=1}^{N}(I_{ijk} - I_{mean})^2 \qquad \text{.....(4.2)}$$

where N is the number of B-scans used to calculate the speckle variance image; *i, j, k* represent the frame index, lateral and depth index respectively; and I_{mean} is the average over the group of pixels. Because of blood flow, the vascular regions are de-correlated between adjacent frames which lead to larger variation in speckle intensity and hence larger speckle variance values [143].

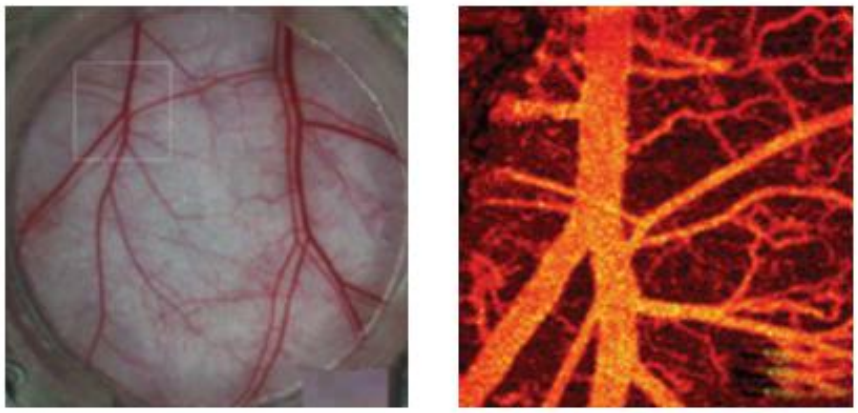

Figure 4.3 *(Left) White light microscopy of dorsal skin-fold window chamber model in mice. (Right) Speckle variance OCT en-face projection image of vasculature in the region marked as square box (1.8× 1.8 mm) (reprinted with permission from Optics Letters [143]).*

One of the major advantages of speckle variance imaging is that it is free from Doppler angle. Also, it uses only the intensity information and is computationally simple. The technique exploits endogenous scattering contrast to provide microvasculature information. However, direct relation of speckle variance with flow velocity is not understood as the variance values cover a wide range and also show dependence on the window size. Hence, a priori structural information is needed to separate static and flowing tissue components. Also it suffers from multiple scattering induced blood vessel shadowing artifacts and bulk motion artifacts that can result in high variance values [144]. Speckle variance OCT has been used to monitor photodynamic therapy, developing embryo, etc. Fig. 4.3 shows the speckle variance images for the dorsal skin fold of the mice [143].

4.3 Development of swept source based SVOCT setup for microvascular imaging

A schematic of the developed swept source based SVOCT setup is shown in Fig. 4.4. Light from a swept source (central wavelength ~ 1325 nm, bandwidth ~ 110 nm) was coupled into a fiber based Mach–Zehnder interferometer through a 80/20 input coupler. Two identical circulators were used to deliver light into the two arms of the interferometer. While 80% of the light was delivered to the sample arm, the remaining 20% was directed to the reference arm. The back-reflected light from both the arms of the interferometer was collected by a 50/50 detection coupler and coupled to an InGaAs balanced photoreceiver (Thorlabs PDB120C). High-speed data acquisition board (NI-5122) was used to digitize the interferometric signal. The Fourier transform of the acquired interferogram provides the depth resolved reflectivity profile of the sample. System control and signal processing was done using Labview^{TM} based software.

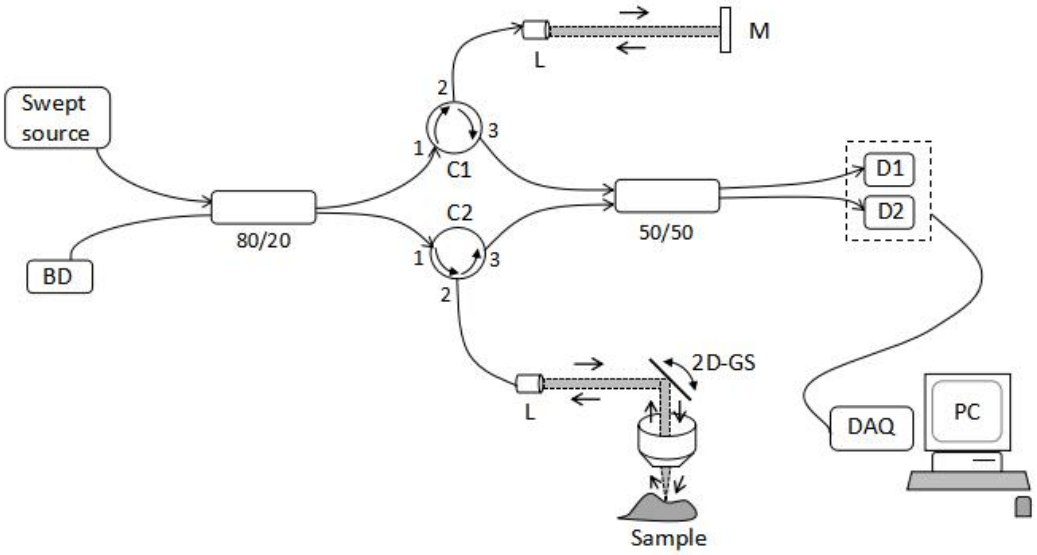

Figure 4.4 *Schematic of SVOCT setup. C1,C2: Circulators; D1,D2: Balanced photodetector; L: Lens; M: Mirror; DAQ: Data acquisition card; PC: Personal computer; 2D-GS: Two dimensional galvoscanner; BD: Beam dump.*

The system features axial and lateral resolutions of ~ 15 μm and ~ 20 μm respectively with a measured SNR of ~ 95 dB. In order to generate *en-face* views of the tissue vasculature, volumetric imaging was done using two dimensional XY scanning. A total of 800 B-frames were acquired in one volume, 5 B-frames being acquired at each step of the slow scanner (Y). The image acquisition time was ~ 5 min for a 2mm x 2mm (XY) area. Speckle variance algorithm was applied on the acquired 3D dataset for generation of microvascular maps. The algorithm makes use of the ratio of standard deviation to the mean value of the intensity of the B-frames (acquired at a particular location) as a measure of temporal fluctuation in the intensity of backscattered light. Speckle variance is very large from vascular regions as compared to the surrounding static tissue because flowing blood introduces large fluctuations in the intensity of the backscattered light. In order to remove noise regions above the tissue surface and at depths below 1 mm from the tissue surface, the speckle variance image was masked by a binary mask generated from the averaged intensity image [145]. In this way, 160 masked speckle variance

images were generated for all 160 locations along the Y scan direction. Maximum intensity projection view was generated for a depth range of 50 to 375 μm below the tissue surface for *en-face* visualization of microvasculature. Several such *en-face* views of adjacent areas were stitched together to generate the microvasculature map over a larger area. In a similar fashion, structural *en-face* maps can also be generated from the intensity images to visualize surface topography.

4.4 Use of swept source based SVOCT for imaging microvascular regeneration in diabetic mice ear

4.4.1 Motivation of the work

It is widely accepted that wound healing is a complex process involving both structural and vascular changes. Hence, information on vascular remodeling can help in more accurate assessment of wound healing [138]. This is of greater importance in diabetic conditions where the wound healing process is delayed/impaired and hence accurate monitoring of vascular remodeling can play a vital role in planning future course of action. A major shortcoming in the testing of angiogenic drugs/therapies lies in the lack of quantitative, non-invasive techniques that can provide time resolved information on microvascular density and perfusion, blood velocity, blood oxygenation, etc from the same tissue site [146]. Generally used intravital methods such as laser Doppler perfusion imaging and MRI angiography, and postmortem methods such as micro-computed tomography (micro-CT) and histology for monitoring dynamic vascular response are highly operator dependent and require access to and expertise in the use of these instruments. It is therefore desirable to develop robust techniques that can provide time dependent measurements on microvasculature thereby helping in rapid screening of new angiogenic therapies. SVOCT is one such intensity based approach that can image tissue microvasculature and thus holds considerable promise for noninvasive monitoring of the

healing of wounds [145]. The approach makes use of the temporal fluctuations in the intensity of light backscattered from flowing blood as compared to surrounding static tissue to image tissue vasculature. Wound healing measurements are preferred in mice because of their low cost and easy availability and maintenance. Cutaneous wounds can be studied using different models. Tape stripping is one such model which is widely used to simulate inflammatory skin conditions. This involves mechanical disruption of only the topmost epidermal barrier (~ 50-100 μm) by multiple applications and stripping off of a tape. Another model for cutaneous wound is the excisional wound wherein full thickness biopsy wounds are created. In the present work, we made use of a mice ear punch wound model because of its high reproducibility. Creating a tape strip or excisional wound on mice ear pinna requires extreme precision. While excisional/tape stripping wounds heal more by contraction, punch wound heals mostly by regeneration. The former is similar to what we observe in tight skinned animals like pig or in humans. It may be noted that mice ear is devoid of subcutaneous fat unlike mice body skin which is loose and has cutaneous fat. Since mice ear has a central cartilage surrounded by epidermis from both sides, a punch wound heals by re-epithelialization and extracellular matrix remodeling [147]. While different wound models may have differences in the vascular and tissue changes occuring during wound healing process, they share common phases of wound healing like inflammation, tissue regeneration and remodeling.

Few works have reported the use of intensity based OCT approaches for monitoring vascular remodeling in mice ear punch wound. Jung et al used optical microangiography (OMAG) to monitor the dynamics of vascular regeneration in mice ear punch wound [147]. Results showed that OMAG could track acute and chronic changes in blood flow, microangiography and structure during wound healing. Yousefi et al also made use of OMAG for *in-vivo* monitoring of microcirculation dynamics at different phases of healing of cutaneous wounds [148]. These results demonstrate that non-invasive label-free

monitoring of each phase of wound healing (by using OMAG) could potentially avoid the use of invasive histological and immunochemistry technologies. To the best of our knowledge, there have been no previous reports on the use of speckle variance OCT for monitoring vascular regeneration in diabetic mice ear pinnae.

Here, we present the use of SVOCT system for monitoring microvascular regeneration in a punch wound created in ear pinna of a diabetic mice. The changes observed in the tissue morphology and vasculature at different time points post wounding are presented.

4.4.2 Materials and methods

4.4.2.1 Experimental setup

The details of the SVOCT used for this study can be found in section 4.3.

4.4.2.2 Mice handling and punch wound creation protocol

Swiss albino mice (12 weeks old, 6 in number) were used for the experiments. The protocol of the study was approved by Institutional Animal Ethical Committee. Mice were housed individually and had free access to food and water *ad libitum*. Multiple intra-peritoneal injection of streptozotocin (50 mg/kg for 5 days) was used to induce diabetes in the mice. A commercial glucometer (One-Touch Horizon, Johnson and Johnson) was used to measure blood glucose concentration for a period of 3 months to ensure sustained hyperglycemia. Mice with blood glucose level of >250 mg/dl were considered as diabetic [149]. At 4 weeks post streptozotocin treatment, the diabetic mice were used for wound creation. A needle was used to create punch wound of 0.5 mm diameter in ear pinnae of each mouse. Owing to its higher transparency and less sensitivity to breathing induced motion, mice ear pinnae is a preferred site for microvascular measurements [150]. For the purpose of OCT imaging, mice were anesthetized by intra-peritoneal injection of ketamine (80 mg/kg body weight) : xylazine (10 mg/kg body weight) cocktail. The mice ear pinna was stabilized on a perspex block using a double sided tape. An ‘L’ shaped mark was drawn over the mice ear to ensure that imaging was carried out at the same

location at different time points. Photographs of the punch wounds were also taken at different time points post wounding (p.w.).

4.4.3 Results and discussion

SVOCT imaging of the mice ear pinna was carried out prior to creation of punch wound and at three different time points p.w. namely 1 hr p.w., 14 day p.w. and 30 day p.w.. Fig. 4.5 shows the typical cross-sectional intensity image for a mice ear pinna where different features like epidermis, cartilage, blood vessel etc can be identified.

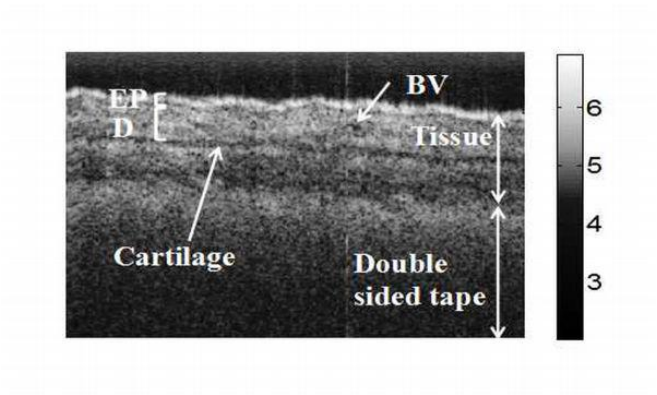

Figure 4.5 *Typical OCT intensity image for a mice ear. EP: Epidermis, D: Dermis, BV: Blood vessel. Image dimension: 1.6 mm (H) x 1.6 mm (V).*

The cross-sectional OCT intensity images (row 1), *en-face* surface topography (row 2) and photographic images (row 3) acquired over the wound site at different time points are shown in Fig. 4.6. These intensity images (row 1) were acquired across the maximum wound size (shown by dashed green lines in the surface topographic maps). The demarcation between the ear and the double sided tape on which the ear was stabilized is shown by black dashed lines in the cross-sectional intensity images. Well defined epidermal and dermal layers can be easily identified in the cross-sectional intensity images. While the combined thickness of these two layers was ~ 150 μm prior to wound creation, this thickness increased to ~ 210 μm at 1 hr p.w. The increase in thickness is probably due to injury induced extravasation of fluids and ensuing inflammation. The

combined (epidermal and dermal layers) thickness further rose to ~ 300 μm at day 14 p.w. and continued to be around ~ 300 μm thick at 30 day p.w. even when the wound had closed. The fact that the dermal thickness does not go back to its pre-punch value even at day 30 p.w. when the wound appears closed is consistent with the observations of Jung et al [147]. It may also be noted that though the wound might have closed after day 30 post punch, the collagen in the dermal layer and the cartilage that gets ruptured due to punch may not have been remodeled completely. This is consistent with results of other studies which suggest that for freshly healed ear pinna punch wound, cartilage remains immature and there is lesser collagen II/VI deposition than healthy cartilage [151,152].

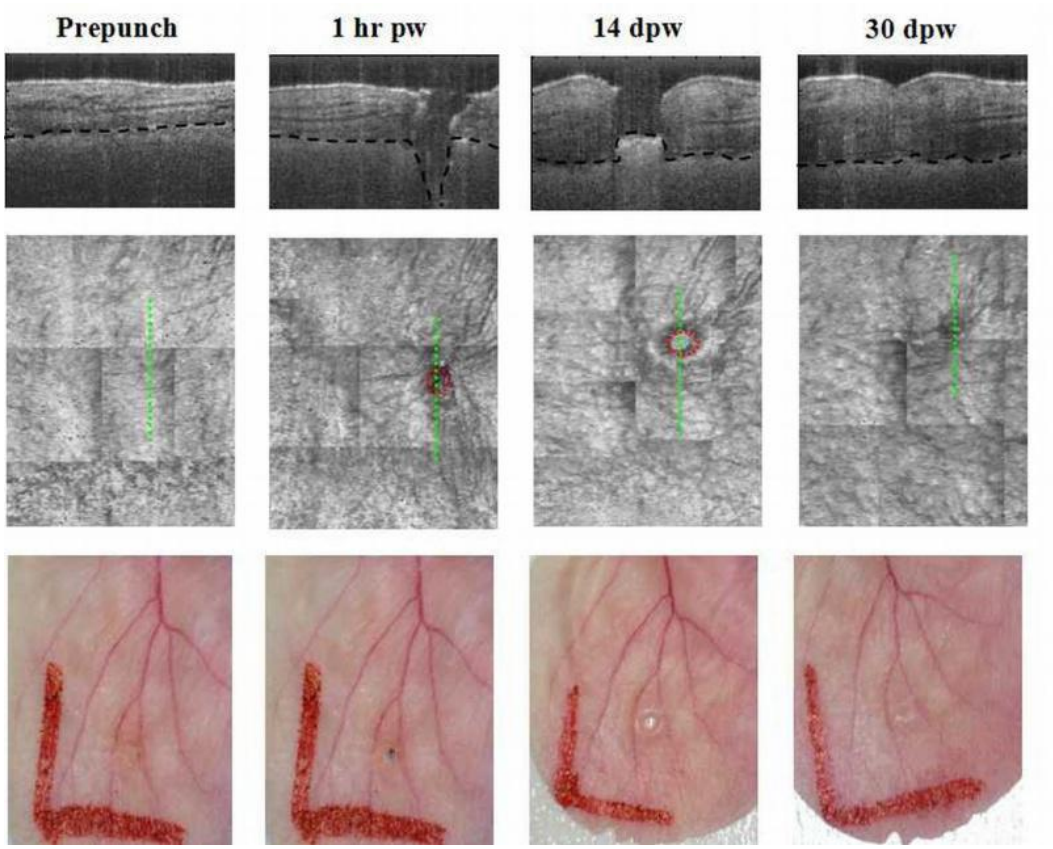

Figure 4.6 *OCT intensity images (row 1), en-face surface topographies (row 2) and photographic images (row 3) acquired before punch and at 1hr, 14 day and 30 days post punch wound (column 1 to 4 respectively). Image dimensions: 1.5 mm (H) x 1.5 mm (V) [for row 1]; 3 mm (H) x 4.5 mm (V) [for row 2 and 3].*

Fig. 4.7 shows the *en-face* microvasculature maps corresponding to the surface topographies presented in Fig. 4.6, row 2. Fig. 4.7(a-d) are the raw microvascular maps generated through the speckle variance algorithm. We made use of a Difference of Gaussian filter to improve the microvascular contrast. This filter is often used for edge enhancement in image processing where it acts as a band pass filter that smoothens very high frequency components corresponding to uncorrelated single pixel noise as well as low frequency background [153]. This filter is particularly suitable for the contrast enhancement in images with binary type of features as in the microvasculature images. To make use of this filter, the image was convolved with two Gaussian functions of different widths. The two images were then normalized to have same integrated intensity and their difference provides the background flattened image.

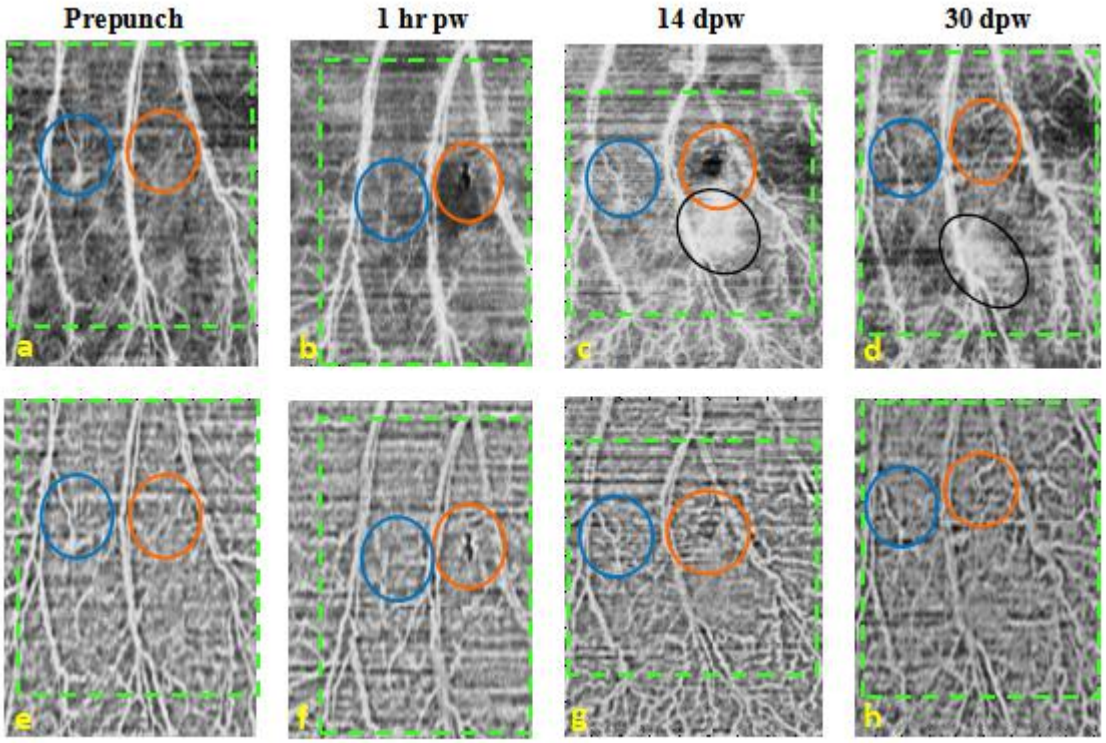

Figure 4.7 *En-face microvasculature images acquired before punch and 1hr, 14 day and 30 days post wound. (a-d): through speckle variance algorithm, (e-h): after application of Difference of Gaussian filter. Image dimensions: 3 mm (H) x 4.5 mm (V). Circled areas show region with prominent vasculature changes.*

Fig. 4.7(e-h) show the images generated after applying Difference of Gaussian filter on the corresponding raw microvascular maps shown in Fig. 4.7(a-d). It can be easily seen that the microvasculature is more prominent and clearly visible in the filtered images shown in Fig. 4.7(e-h). The common imaged areas have been marked by green dashed rectangles. It is observed that immediately after the punch wound creation; at 1 hr p.w., the vasculature is completely lost in the vicinity of wound area (shown by orange circle). It may also be noted that the vasculature gets affected in a larger area surrounding the wound. As the wound healing progresses, some fine capillaries start to grow in and around the punch affected zone. From the blue circles, one can see that a vessel segment that gets damaged at 1 hr p.w. starts regenerating around 14 days p.w. and is completely restored at 30 days p.w.. The presence of signal rich areas (as shown by black ovals in Fig. 4.7(c,d)) is probably due to the damage to the vasculature and the resulting extravasation of fluid. The fact that the wound size as assessed by vascular images is larger than that assessed by structural images at all the time points is consistent with the reported literature [147]. Since the presence of a functional vasculature is essential for proper tissue functioning, one can monitor the wound repair more precisely through such microvascular maps.

4.5 Conclusions

To conclude, we discussed different intensity based approaches for microvasculature imaging. Since these are independent of Doppler angle and are less sensitive to bulk tissue motion, these are more amenable for *in-vivo* imaging of tissue microvasculature. We then describe the in house development of swept source based SVOCT system for microvascular imaging. We further made use of the developed SVOCT system for *in-vivo* monitoring of healing of punch wounds in ear pinna of diabetic mice. The microvasculature was successfully monitored for upto 30 days post wounding. The results show that SVOCT can provide fine vascular details thereby allowing more accurate

assessment of wound healing as compared to the use of intensity information alone. The observed results on dermal thickness and wound size are in accordance with the reported literature. The findings from the current investigation suggest that SVOCT measurements on vasculature remodeling in mice ear punch wound model can be used to study the effects of potential therapeutic agents that can alter angiogenesis in wound healing.

Chapter 5

Non-invasive assessment of cutaneous alterations in mice exposed to whole body gamma irradiation using functional optical coherence tomography

In this chapter, we present our results on the use of functional optical coherence tomography and cross polarization imaging techniques for non-invasive assessment of cutaneous alterations in mice exposed to whole body gamma irradiation. Radiation dose dependent changes were observed in tissue retardance and microvasculature as early as 1hr post radiation exposure. Results suggest that the used optical techniques can serve as useful tools for early and non-invasive screening of population exposed to radiation.

Work discussed in this chapter has resulted in the following publication:

1. "Noninvasive assessment of cutaneous alterations in mice exposed to whole body gamma irradiation using optical imaging techniques", **P. Sharma**, K. Sahu, P. K. Kushwaha, S. Kumar, M. K. Swami, J. Kumawat, H. S. Patel, S. Kher, P. K. Sahani, G. Haridas & P. K. Gupta, *Lasers in Medical Science*, **2017**, 32, 1535-1544.

5.1 Introduction

Accidental or intentional release of ionizing radiation in a densely populated area calls for rapid screening of exposed population [154]. Exposure to high dose of ionizing radiation induces DNA damage and release of free radicals thereby causing damage to highly proliferating cells such as in skin [155]. Moreover, in case of local exposure during medical or industrial uses of ionizing radiation, visibly assessable changes are first observed on skin as it is the outermost layer of body that is exposed first [156]. Currently used methods for detection of cutaneous radiation injury include use of visual examination, event recall by the subject, numerical dosimetry reconstruction and cytogenetic analysis. Techniques such as *ex-vivo* electron para-magnetic resonance measurements, fluorescence in-situ hybridization, premature chromosome condensation assay and hypoxanthine-guanine phosphoribosyltransferase, etc can be used to perform quantitative bio-dosimetry [157]. However the above discussed methods are not amenable for rapid screening of radiation exposed population.

Collagen and vasculature are among the various tissue components that are damaged by exposure to radiation. Radiation exposure induced changes in tissue collagen and vasculature have been primarily studied using electron microscopy, polyacrylamide gel electrophoresis and immuno-histochemistry [158,159]. These methods are invasive and require intensive sample preparation. Optical imaging techniques allow non-invasive real time monitoring of radiation exposure induced changes in cutaneous tissue. Since collagen is a birefringent tissue component, PSOCT measurements allow monitoring changes in the organization or content of tissue collagen [160,161]. Maslennikova et al made use of techniques like second harmonic generation microscopy and cross polarization optical coherence tomography for early assessment of radiation induced damage to the collagen structure in murine tail tendon [162]. Reflectance confocal microscopy has also been used to visualize the onset of spongiosis, exocytosis and

infiltration of inflammatory cells in acute radiation dermatitis [163]. Microcirculatory network, an interconnected network of blood vessels, is responsible for the transport and exchange of oxygen, nutrients and other biomolecules between blood and the tissue. This is among the important tissue elements that are affected by radiation exposure. Imaging microcirculation can provide useful information on changes in local metabolism and tissue viability. Goertz et al made use of intravital fluorescent microscopy to carry out long-term investigations on cutaneous microcirculatory and inflammatory changes following irradiation [164]. Diffuse optical spectroscopy and hyperspectral imaging have been successfully used to monitor changes in perfusion, oxygenation status and to differentiate ionizing radiation induced skin toxicity as early as 2 hour post irradiation [165,166]. While intravital fluorescent microscopy requires intravenous administration of fluorochromes, diffuse optical spectroscopy and hyperspectral imaging require large computation time which limits their use for rapid screening. Although laser Doppler flowmetry has also been used for non-invasive measurement of perfusion, it lacks the high resolution required for visualization of microcirculation [167]. Most of the earlier reported studies were performed for high exposure doses and there are only a few studies on effect of low dose exposure on cutaneous tissue microvasculature. By making use of several biochemical tests, Vala et al have shown that low dose of exposure promotes both embryonic and adult angiogenesis in Zebrafish [168]. While the above discussed studies highlight the sensitivity of optical methods in monitoring the radiation induced changes in cutaneous tissue, quantitative assessment of changes in the optical properties of skin and microcirculation with different time-dose need more detailed investigations.

Speckle variance optical coherence tomography (SVOCT) is a widely used technique that allows noninvasive depth resolved images of tissue microvasculature by making use of the temporal fluctuations in the intensity of light backscattered from the tissue [143,145]. To corroborate our observations on tissue microvasculature using SVOCT, we used cross

polarization imaging (CPI) which is another optical imaging modality that can be used to assess changes in blood flow and vascular arrangement. The CPI system makes use of the fact that the light gets increasingly depolarized as it propagates deeper into the tissue. Hence, the vasculature present in the superficial layers can be imaged by observing scattered light in the orthogonal polarization state with respect to the incident linear polarization. In this chapter, we present the combined use of polarization sensitive optical coherence tomography, speckle variance optical coherence tomography and cross polarization imaging for early monitoring of radiation exposure induced changes in the cutaneous tissue of mice exposed to whole body irradiation as a function of exposure dose.

5.2 Material and methods

5.2.1 Mice handling and irradiation protocol

Swiss albino mice is a widely used strain to monitor radio-protective effects of various drugs after exposure to whole body gamma irradiation [169,170]. A total of 32 (16 male and 16 female, 25-28 gms) such mice were used for our experiments. These individually caged mice were divided into sham and irradiated groups and had free access to food and water *ad libitum*. Different exposure doses (0.5, 2, 5, 10 and 20 Gy) were used for the experiment. Cobalt-60 source with a dose rate of 2.7 Gy/hr was used for low dose exposure (0.5 and 2 Gy). For higher exposure doses (5, 10 and 20 Gy), mice were exposed to gamma radiation in a Gamma Chamber 5000. This comprises of a set of stationary Cobalt-60 sources placed in a cylindrical cage and delivers radiation with a dose rate of 0.8 kGy/hr. For irradiation, mice were physically restrained inside a custom made perforated perspex tube. This tube was rotated continuously to ensure uniform irradiation. During irradiation, the tube was kept in a vertically upright position with the head of the animal towards the top. Retardance of mice skin and microvasculature in mice ear pinnae were monitored both prior to gamma irradiation as well as at 1hr, day 1, day 2, day 3, day 7, 2nd week, 4th week and 2 months post irradiation. For imaging purpose, mice

were anesthetized by intra-peritoneal injection of ketamine (80 mg/kg): xylazine (8 mg/kg) cocktail. An area of 1 cm x 2 cm was marked on the back of each mice which was made hairfree through use of trimmer and depilatory hair removal cream (Hindustan Lever/Johnson and Johnson). Since dermal region of skin contains collagen which is birefringent in nature, PSOCT can be used to assess alteration in cutaneous tissue by monitoring changes in tissue retardance. However, breathing induced motion, high scattering from dermal region and relative opacity make it difficult to monitor blood flow and microcapillaries in mice back skin. At the same time, mice ear pinnae is a preferable site for microvascular measurements because of the much higher transparency of this tissue site and the fact that measurements here are less sensitive to breathing induced motion. For microvascular measurements using SVOCT and CPI, a region of interest was marked on mice ear pinna and repeated measurements were performed on the same location at different time points. Mice ear pinna was stabilized on a perspex block using double sided tape. All the experimental procedures involving animals were approved by the Institutional Animal Ethics Committee, in accordance with the guidelines of the Committee for Purpose of Care and Supervision of Experimental Animals (CPCSEA), Department of Environment and Forests, Government of India. Individually housed mice were maintained on a 12-h light/dark cycle at 22 °C (±2 °C). All the animal imaging experiments were carried out in anesthetized conditions, and animals were kept on warm cotton pads for recovery from anesthesia. Animals were euthanized by cervical dislocation. All research animals were treated humanely, and all efforts were made to minimize the animal suffering and the number of animals killed. The tissue excision procedure was also in accordance with the guidelines of Institutional Animal Ethics Committee.

5.2.2 Visual assessment of alterations in skin

The scale used by Randall and Coggle was used to score the skin's acute reaction to ionizing radiation [171]. Here, a score of 0 represents normal skin, 1 represents erythema, 2 represents dry desquamation and/or pigmentation changes, 3 represents incomplete moist desquamation and 4 represents complete moist desquamation.

5.2.3 Experimental setups for assessment of cutaneous alterations

Fig. 5.1A shows the schematic of the spectral domain PSOCT setup used for retardation measurements. The details of the system have already been discussed in Chapter 2 [160]. The imaging depth achieved by PSOCT in mice back skin was ~ 750 μm with the imaging wavelength region being around 840 nm.

The schematic of the swept source based SVOCT setup used for imaging microvasculature is shown in Fig. 5.1B. The details of the system have already been discussed in Chapter 4. For *en-face* visualization of microvascular maps, maximum intensity projection view was generated for a depth range of 50 μm to 375 μm below the tissue surface. Several such *en-face* views of adjacent areas were stitched together to generate the microvasculature maps over a larger area.

Fig. 5.1C shows a schematic of the CPI system. The system comprises of a blue (450 nm) and green (530 nm) LED as excitation source. The collimated excitation light was horizontally polarized using a linear polarizer and then passed through a lens L_1 to focus it on to the sample. The light scattered from the sample was first passed through an aperture (~0.5 mm diameter) followed by an objective lens L_2 and an analyzer crossed with respect to the input polarizer. The light passing through the analyzer was then imaged on to a CMOS camera. Difference of Gaussian filter was used for contrast enhancement in the microvasculature images.

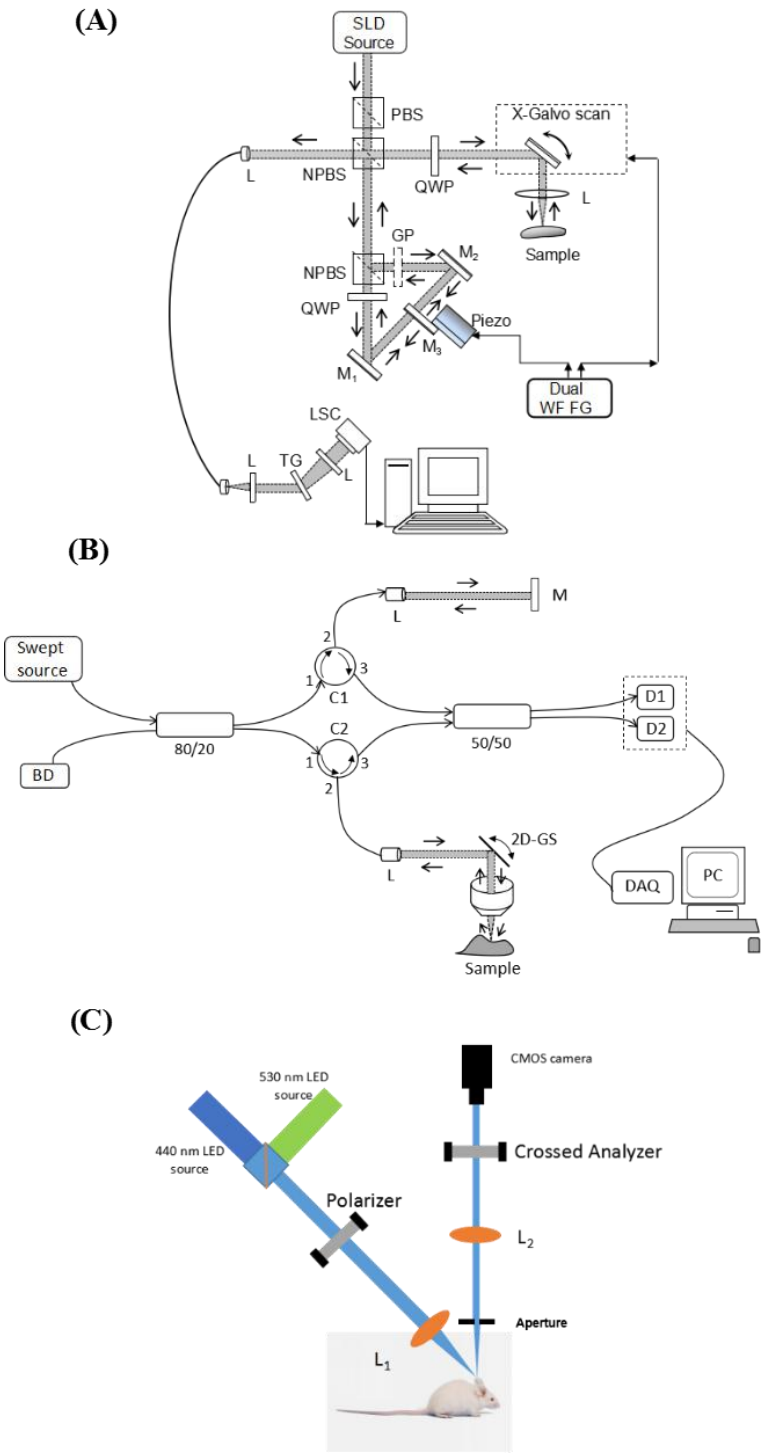

Figure 5.1 *Schematic of (A) PSOCT setup for measurement of cutaneous retardance. (B) Swept source based SVOCT setup and (C) CPI setup for imaging of microvasculature. SLD: Superluminescent diode, PBS: Polarizing beam splitter, NPBS: Non-polarizing beam splitter, QWP: Quarter waveplate, GP: Glass plate, L: Lens, M M_1 M_2 M_3: Mirrors, LSC: Line scan camera, TG: Transmission grating, WFFG: Wave form function generator, C1,C2: Circulators, 2D-GS: Two dimensional galvoscanner, D1,D2: Balanced photodetector, DAQ: Data acquisition card, BD: Beam dump, PC: Personal computer.*

5.2.4 Histology and trichrome staining

Histology was carried out to correlate the changes observed in retardance with the actual structural changes in the cutaneous tissue. Unirradiated (n =2) and irradiated mice of 5 Gy and 10 Gy exposure groups (n =2 for each group) were euthanized by cervical dislocation at 4^{th} week post irradiation. Cutaneous tissue area of 0.5 cm x 0.5 cm was excised from the back of each mice, fixed in formalin and processed for standard histological processing. This was then followed by Masson's trichrome staining for assessment of collagen fibers. Histological slides were observed under the optical microscope at 40 X magnification to look for changes in collagen layer, dermal papillae and epidermal thickness.

5.2.5 Statistical analysis

Data were analyzed and expressed as mean ± standard deviation (SD). Statistical comparison between means was carried out using one way ANOVA followed by Turkey and Fishers LSD test. $p<0.05$ were considered significant.

5.3 Results and discussion

5.3.1 Ionizing radiation induced alterations in skin

Visual scores were given to mice exposed to different doses on the basis of the overall changes observed in skin texture during day 1-3 post exposure. The mean visual scores assigned to mice skin exposed to 0.5, 2, 5, 10 and 20 Gy were 0, ~ 0.2 , ~0.5, ~1.25 and ~2.7 respectively, as shown in Fig. 5.2. Extensive skin ulceration was observed by day 2 in mice exposed to 20 Gy.

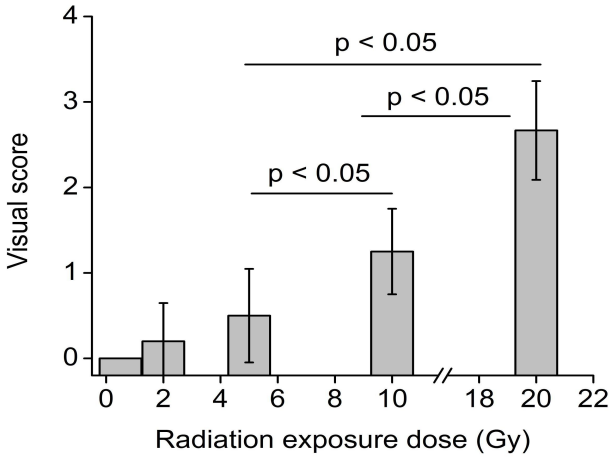

Figure 5.2 *Dose dependent visual scores on the basis of observed structural changes.*

Further, while the mice exposed to 5 and 10 Gy showed ~ 20 % and 50 % mortality, respectively within 30 days post exposure, mice exposed to 20 Gy showed ~90 % mortality within 7 days. Fig. 5.3 shows the trichrome stained histological sections of skin of unirradiated and irradiated mice. Disorganized collagen layer (red arrows), epidermal thinning (solid black arrows) and loss of dermal papillae (green arrows) are observed on day 28 post irradiation in mice exposed to 5 Gy (Fig. 5.3 B) and 10 Gy (Fig. 5.3 C) as compared to unirradiated mice skin (Fig. 5.3 A).

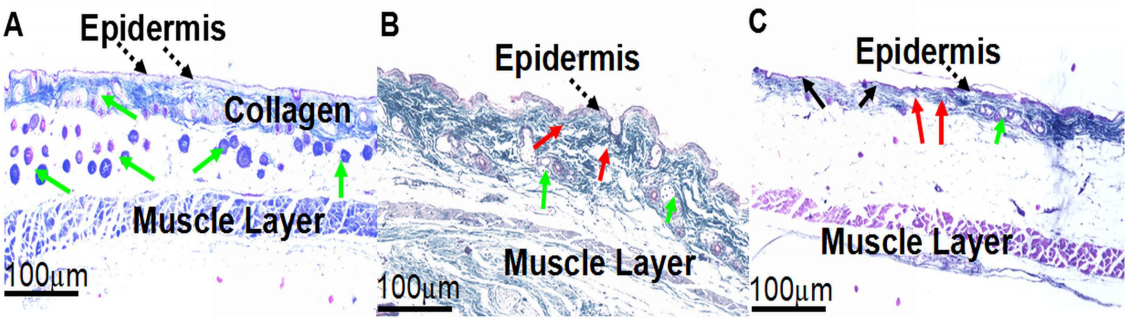

Figure 5.3 *Structural changes in mice exposed to different doses of Gamma radiation. Histomicrographs for skin of mice belonging to unirradiated (A), 5 Gy (B), 10 Gy (C) groups at 4th week post exposure. Compared to the skin of unirradiated mice (A), the destabilized collagen layer (red arrows), decrease in number of dermal papillae (green arrows) and epidermal thinning (solid black arrows) can be observed in skin of irradiated mice (B-C). The histological images are representative of two independent experiments carried out in four mice of each group.*

5.3.2 Ionizing radiation induced alterations in skin retardance

PSOCT setup was used to perform retardance measurements on cutaneous tissue of mice. In Fig. 5.4 (A-D), we show the retardance values for mice exposed to 0.5 (A), 2 (B), 5 (C) and 10 Gy (D) radiation dose at 1, 24, 48 and 72 hr post exposure. Representative PSOCT images of mice back skin before radiation exposure (with 5 Gy), and at different time points post irradiation are shown in Fig. 5.5. The retardance values were computed by taking average over multiple such images, for each irradiation dose. The retardance values have been normalized with respect to the pre-exposure values. The retardance values are seen to decrease significantly ($p < 0.05$) at 1 hr post exposure with the decrease being higher for higher radiation dose (Fig. 5.6A). The immediate decrease in retardance is attributed to the damage caused by a result of robust, but transient, production of reactive oxygen species (ROS) [172]. Since ROS generation post radiation exposure is dependent on the radiation dose, the retardance values show inverse relationship with the ionizing radiation dose [173]. Further, it is observed that the initial reduction in retardance at 1hr post exposure is followed by a partial recovery around 48 hr-72 hr. This is in conformation with the observations made by Maslennikova et al on collagen structure in rat tail tendons exposed to 2-10 Gy [162].

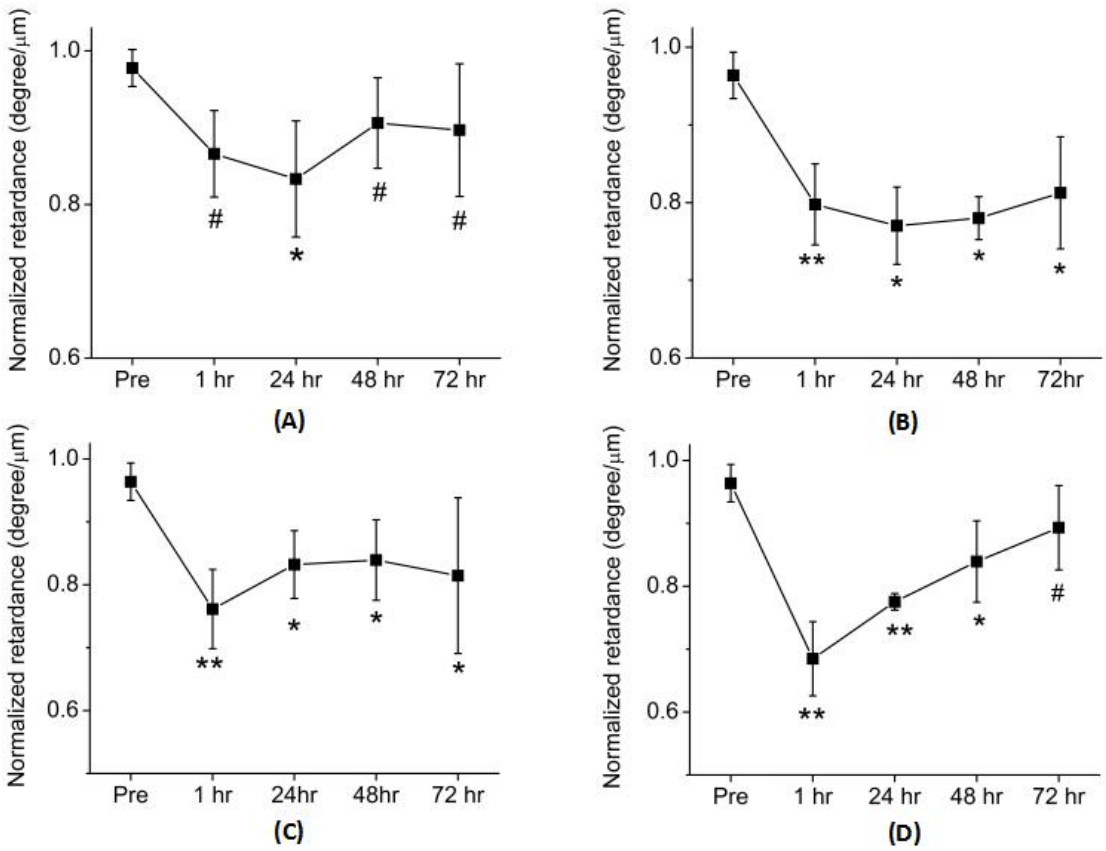

Figure 5.4 *Ionizing radiation induced alterations in retardance of mice cutaneous tissue. Retardance plots for 3 days post irradiation in mice exposed to 0.5 Gy (A), 2 Gy (B), 5 Gy (C) and 10 Gy (D), respectively. ** $p<0.05$ with respect to preceding and pre-exposure value, *$p<0.05$ with respect to pre-exposure value, # $p>0.05$ with respect to preceding and pre-exposure value (one way ANOVA followed by Fisher's test).*

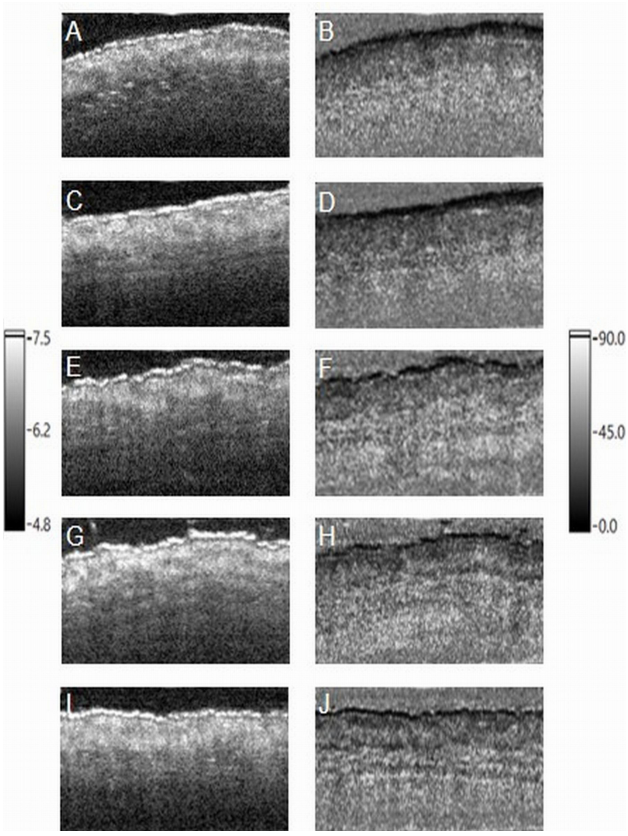

Figure 5.5 *Representative PSOCT images of mice back skin before radiation exposure (A, B), and at 1 hr (C, D), 24 hr (E, F), 48 hr (G, H) and 72 hr (I, J) post exposure with 5 Gy.*

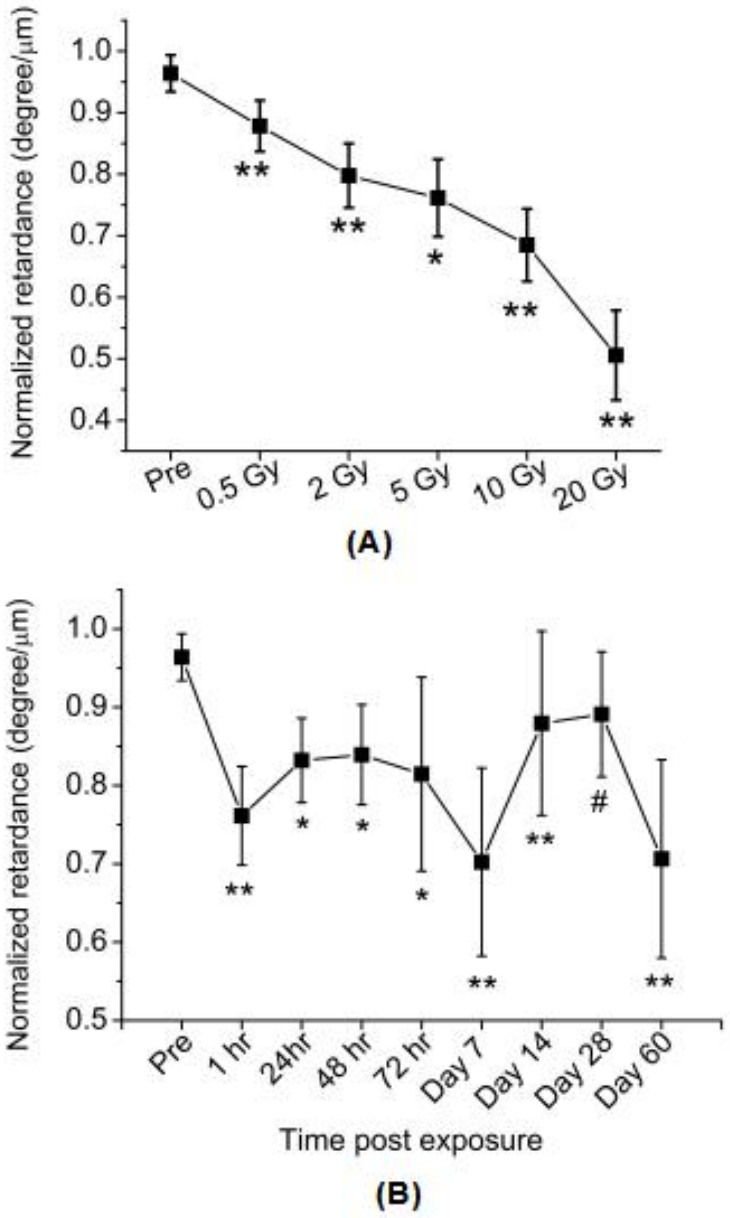

Figure 5.6 *(A): Dose dependent variation of retardance values 1 hr post irradiation. (B): Ionizing radiation induced changes in skin retardance assessed up to a period of 2months post irradiation for mice exposed to 5 Gy.** $p<0.05$ with respect to preceding and pre-exposure value, *$p<0.05$ with respect to pre-exposure value, # $p>0.05$ with respect to preceding and pre-exposure value (one way ANOVA followed by Fisher's test).*

While the acute effects of radiation exposure such as erythema and edema are known to arise within a week, the long term changes such as dermatitis, ulceration and necrosis take months to years to appear [164]. To observe the long term effects of ionizing radiation exposure on cutaneous tissue, retardance measurements were carried out for 2 months

post exposure in mice exposed to 5 Gy. In Fig. 5.6(B), we show the retardance values as a function of post exposure time. Following a partial recovery during the first 3 days, retardance is observed to decrease at day 7 post exposure. This is then followed by a second recovery phase around 14-28 days post exposure and a reduction phase at ~2 months post exposure. This oscillatory behaviour of tissue retardance may be attributed to the successive inflammatory waves associated with radiation exposure induced skin injury [156,174,175]. This can be understood considering the fact that oxidative stress continues days after irradiation because of propagation of free radicals [176].

5.3.3 Ionizing radiation induced alterations in microvasculature

Mice ear pinnae is a widely preferred model for assessment of vascular changes because of its less sensitivity to breathing induced motion artifacts as compared to the back of mice and higher transparency that allows repeated measurements on the same area [147,148]. Microvascular changes were assessed in mice ear pinnae using SVOCT and CPI setups.

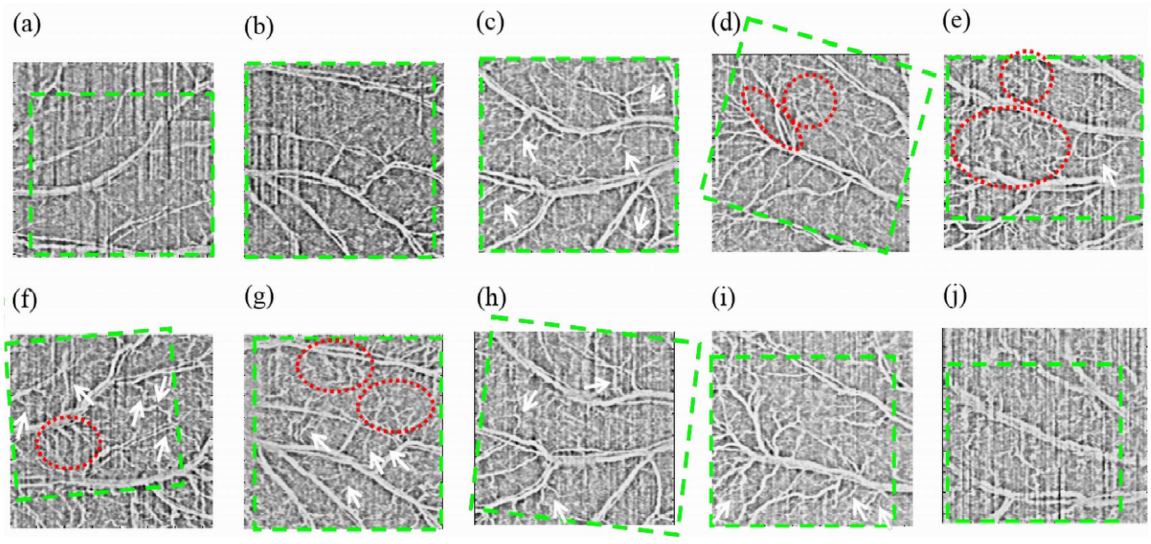

Figure 5.7 *Ionizing radiation induced alterations in ear pinnae microvasculature. En-face microvasculature of mice ear before exposure (top row) and 1 hr post exposure (bottom row) to 0.5 Gy (a, f), 2 Gy (b, g), 5 Gy (c, h), 10 Gy (d, i) and 20 Gy (e, j) respectively. Image size: 4. 5 mm (X) x 4.5 mm (Y).*

Fig. 5.7 shows the pre-exposure (top row) and 1 hr post exposure (bottom row) microvascular maps obtained using SVOCT for mice exposed to 0.5 Gy (a, f), 2 Gy (b, g), 5 Gy (c, h), 10 Gy (d, i) and 20 Gy (e, j) respectively. The region of interest common to images acquired at different time points is marked by green dashed squares. The vasculature that gets damaged due to radiation exposure is marked by white arrows and dashed red circles in the pre-exposure images (Fig. 5.7 a-e). These vascular features are not seen in the 1hr post exposure images (Fig. 5.7 f-j). Similarly, in the images taken at 1hr post exposure (Fig. 5.7 f-j), the white arrows and dashed red circles mark the vasculature which was not observed before exposure (Fig. 5.7 a-e). Significant appearance of new vasculature was observed for low dose exposure (0.5 and 2 Gy). This appearance of new microvasculature is in conformation with the angiogenesis promoting effects reported for low exposure dose [168]. An overall reorganization of the vasculature with disappearance of microvascular features in some regions and observation of new vascular features in other regions is observed for the intermediate doses of 5 Gy and 10 Gy. Loss of vasculature is more prominent for higher exposure dose of 20 Gy. This loss of vasculature can be attributed to the loss of endothelium, as observed by Goertz et al in mice ear exposed to 90 Gy [164].

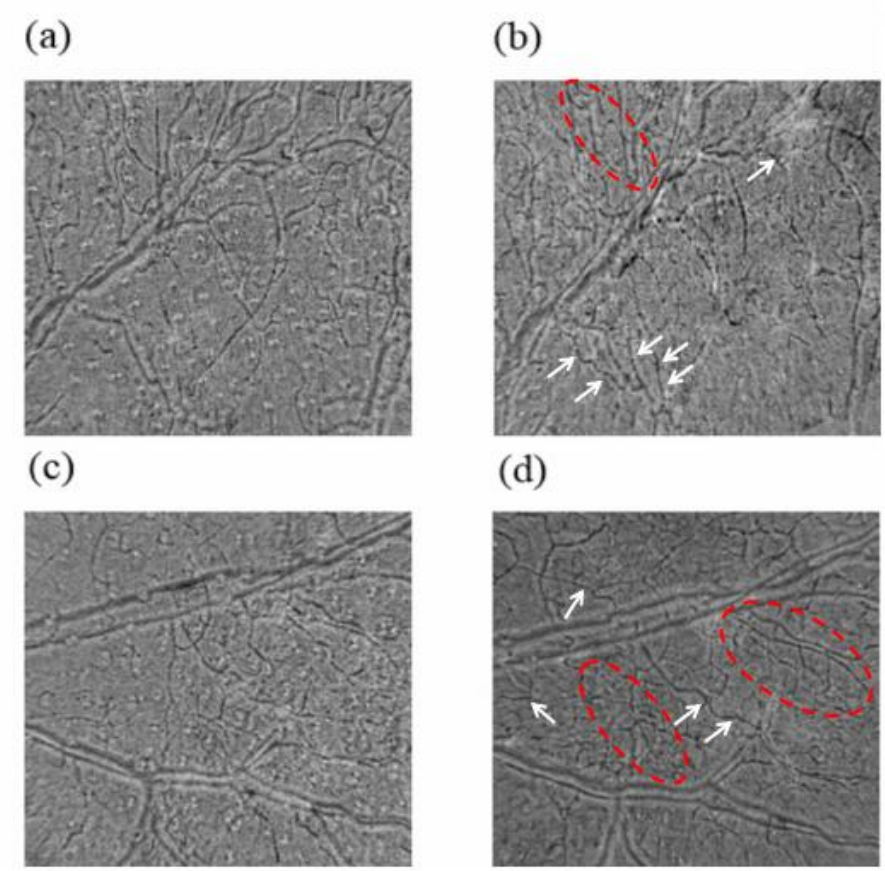

Figure 5.8 *First frames of video recorded with CPI system before exposure and after exposure to 0.5 Gy (a, b) and 2 Gy (c, d).*

CPI system was also used to monitor the effect of radiation exposure on microcirculation. In Fig. 5.8 (a, b), we show first frames of video recorded with CPI system before exposure and at 1 hr post exposure to 0.5 Gy. The corresponding frames for 2 Gy exposure are shown in Fig. 5.8 (c, d). The appearance of new vasculature, as marked by dashed arrows and red ovals in Fig. 5.8, accompanied by an observable increase in the flow velocity and diameter of some vessels may be attributed to the inflammation and the increased metabolic requirements of the tissue. Goertz et al demonstrated an increase in the arteriolar and venular diameters and blood flow velocity at 1 day post irradiation in mice ear exposed to 90 Gy (dose rate ~0.56 kGy/hr). These parameters were observed to remain elevated above the baseline value for a period of 1 year, which is attributed partly to the increased inflammation during this time period [164]. Increase in the tissue oxygen

saturation and the total hemoglobin content in the early phase after radiation exposure in mice exposed to 50 Gy beta radiation, as observed by Chin et al suggests the increased metabolic and oxygen requirements of the tissue [166]. Our observations on increased blood flow velocity and diameter of vessels are therefore in qualitative agreement with the results of these studies [164,166].

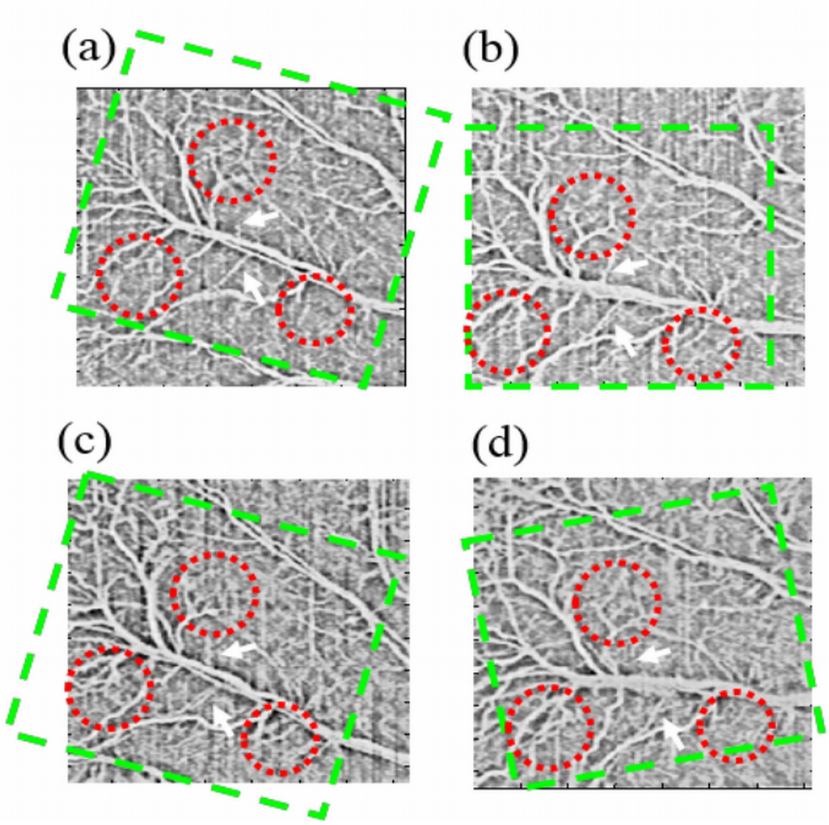

Figure 5.9 *En-face microvasculature of mice ear before exposure (a), at 1 hr (b), 24 hr (c) and day 7 (d) post exposure to 10 Gy. Image size: 4. 5 mm (X) x 4.5 mm (Y).*

In Fig. 5.9, we show the *en-face* view of mice ear microvasculature at different time points (pre-exposure, 1 hr, 24 hr and 7 day post exposure) for 10 Gy exposure. The white arrows and dashed red circles in these images indicate the regions with vascular alterations. As compared to the pre-exposure vascular arrangement, significant alterations in microvascular network were seen even at 1hr and 24 hr post exposure. However, by

day 7 post exposure, some of the pre-exposure features of microvasculature start to reappear.

5.4 Conclusions

PSOCT was used to observe dose dependent (0.5-20 Gy) changes in cutaneous tissue retardance. The changes induced by exposure to ionizing radiation were observed as early as 1 hr post irradiation. A wavy trend was observed in cutaneous tissue retardance during day 1 to 60 post exposure. SVOCT and CPI were used to observe dose dependent alterations in microcirculation. While appearance of new microvasculature was observed for low exposure doses (0.5 and 2 Gy), loss of microvasculature was observed for higher doses (10 and 20 Gy). The observations clearly indicate that these optical techniques could detect radiation dose dependent alterations in cutaneous tissue which could be of potential help in screening of radiation exposed population. However, it would be interesting to carry out such studies on larger population to firmly establish potential of these optical imaging techniques for monitoring of radiation dose and post exposure time dependent alterations in cutaneous tissue.

Chapter 6

Conclusions and Future Scope

6.1 Summary

The major objective of this thesis was to develop various functional extensions of OCT and use them for different biomedical imaging applications. A standard OCT system exploits the intrinsic variation in tissue refractive index to distinguish various tissue microstructures and provides a depth resolved image of tissue reflectivity. Apart from tissue reflectivity, by measuring change in other parameters of backscattered light like phase, polarization, etc, other functional characteristics of the sample like blood flow velocity, birefringence, etc can also be determined. This additional information may provide an insight into functional disturbances, which usually precede morphological changes and could be useful for early diagnosis of diseases. Several functional variants of OCT such as polarization sensitive OCT, Doppler OCT and speckle variance OCT were developed to provide functional information like birefringence, flow velocity and microvascular arrangement in the tissue.

We first developed a single detector based spectral domain PSOCT setup where each orthogonal polarization channel simultaneously sees all the pixels and hence full imaging range is available for each channel. The developed system makes use of a novel dual reference arm geometry such that an equal and opposite path length change is introduced between the orthogonal polarization beams. This helps in removal of complex conjugate artifact in a way that both the orthogonal polarization channels experience identical depth dependent sensitivity profile. The developed system was used for *ex-vivo* imaging of human oral mandibular tissues. Our results show that compared to the changes observed

in the epithelium thickness and the decay constant of A-scan intensity profile, a much larger degree of change was observed in the phase retardation for tissue sites progressing from normal to the malignant state. These results suggest that monitoring of tissue retardance can help in better differentiation of normal and cancerous oral tissue sites.

In addition to the retardance measurements, monitoring blood flow is an important requirement for assessment of tissue viability. Doppler OCT is an important functional extension of OCT that allows determination of absolute flow velocity. Single beam DOCT measurements provide access to the axial velocity component and prior information on the angle between the flow direction and the incident beam (Doppler angle) is required for retrieval of absolute flow velocity. This however is not possible for most biological tissues where tortuous vasculature is surrounded by turbid tissue matrix. This requires simultaneous probing of the same spatial location in the sample with multiple beams with different incidence angles. However, increasing the number of probe beams introduces the problem of cross-talk images which is of major concern for spectral domain systems that have limited imaging depth range.

As a step towards development of a three beam DOCT setup that allows unambiguous determination of flow velocity, we first developed a dual beam DOCT setup. This setup makes use of a beam displacer to provide two orthogonal linearly polarized beams that probe the sample simultaneously at two different incidence angles. The approach helps remove the cross-talk image and facilitates single detector-based spectral domain velocity measurement. After successfully demonstrating velocity measurements in a flow phantom, the setup was suitably modified for three beam based velocity measurements. Along with the use of beam displacer for removal of cross-talk image, the modified scheme uses galvoscanner based phase shifting for removal of complex conjugate mirror artifact. This scheme allows efficient utilization of the sensitivity and imaging range of the spectral

domain OCT system. Absolute velocity measurements were demonstrated in a flow phantom using the developed setup.

Apart from the flow velocity, arrangement of tissue microvasculature is an important parameter for several pathological conditions which involve microvascular alterations. While DOCT can also be used to generate microvascular maps, its dependence on Doppler angle and the high sensitivity of phase measurements to tissue motion results in incomplete noisy microvascular maps. We developed a swept source based speckle variance OCT system that utilizes the temporal fluctuations in the intensity of backscattered light to image the tissue microvasculature. The insensitivity of this technique to Doppler angle is an added advantage. The developed speckle variance OCT setup was used to monitor cutaneous microvasculature regeneration during healing of wound in diabetic mice. Structural and vascular changes were monitored in a punch wound in the ear pinna of diabetic mice. It was observed that the dermal thickness does not go back to its pre-punch value even at day 30 p.w. when the wound appears to be physically closed. The cartilage layer is also not completely formed. It may also be noted that the vasculature gets affected in a larger area surrounding the wound. The observation that the wound size as assessed by vascular images is larger than that assessed by structural images at all the time points is consistent with the reported literature. The results show that the developed speckle variance OCT system can be used to monitor vascular regeneration during wound healing.

In case of intentional/accidental leakage of ionizing radiation in the human environment, rapid non-invasive screening of population exposed to ionizing radiation is a critical requirement. Present methods for the detection of cutaneous radiation injury like visual examination, event recall by the subject, numerical dosimetry reconstruction, cytogenetic analysis and quantitative bio-dosimetry are not amenable to rapid screening of population exposed to radiation. This calls for development of optical imaging modalities that can

aid in rapid screening of radiation exposed population. We therefore used optical techniques to monitor radiation exposure induced cutaneous alterations in mice model. While the spectral domain polarization sensitive OCT was used to monitor changes in retardance in the dorsal skin, speckle variance OCT and cross polarization imaging setups were used to monitor microvascular alterations in the mice ear pinna. Radiation dose dependent changes were observed in tissue retardance and microvasculature as early as 1hr post radiation exposure. These results suggest that optical techniques may provide a useful tool for early and non-invasive screening of population exposed to radiation.

6.2 Future outlook

The present thesis work can be further extended in various directions. Fast axis orientation is an important parameter for complete determination of birefringent characteristic of tissue. However, determination of fast axis orientation requires phase sensitive measurements. In the developed spectral domain PSOCT, we made use of intensity measurements to retrieve the birefringence information of the sample. Efforts were also made to retrieve fast axis orientation through phase sensitive measurements. However, there appeared to be some offset in the phase values for the orthogonal polarization channels, possibly because of the equal and opposite phase shifting introduced in the orthogonal polarization channels for removal of complex conjugate artifact. Morover, the offset value was found to be varying randomly which limited our efforts for measurement of fast axis orientation. One can work towards devising scheme for determination of fast axis orientation of the tissue through phase sensitive measurements in the developed spectral domain PSOCT setup. Bulk tissue motion is an important issue in DOCT that corrupts the phase information and hence the flow velocity estimation. This is also one of the big hurdles towards clinical *in-vivo* utility of DOCT systems. Efforts can be made towards devising ways to minimize bulk tissue motion during *in-vivo* imaging. Furthermore, efforts can be made towards reducing imaging time

to allow real time 3D imaging of flow velocity and associated vasculature. Development of compact systems with handheld probes is an crucial requirement towards using OCT as a bedside monitoring modality and efforts can be made in this direction. These steps together will be instrumental in establishing clinical utility of DOCT systems.

Ina addition to the assessment of ionizing radiation exposure induced cutaneous effects using functional OCT, efforts can be made towards performing biochemical measurements and correlating the observations. Efforts can also be made to identify OCT signatures specific to radiation burns, which could later be used to differentiate radiation burns from thermal burns. A possible direction could also be to observe effects of localized radiation exposure and compare them with full body exposure effects. Studies on larger animal population as a function of exposure dose and post exposure time would be worthwhile to establish the use of OCT as a potential screening device.

It would also be interesting to work out schemes that allow integration of different functional variants of OCT that can provide single shot multi-functional information of the tissue in addition to the morphological information. Efforts can also be done towards devising schemes for integration of OCT with other adjunct imaging techniques like fluorescence microscopy, Raman spectroscopy, etc which will provide a complete comprehensive picture of the tissue with simultaneous morphological and biochemical information.

References

1. A. F. Fercher, W. Drexler, C. K. Hitzenberger and T. Lasser, "Optical coherence tomography-principles and applications," *Rep. Prog. Phys.* **66**, 239–303 (2003).
2. P. H. Tomlins and R. K. Wang, "Theory, developments and applications of optical coherence tomography," *J. Phys. D: Appl. Phys.* **38**, 2519–2535 (2005).
3. D. Huang, E. A. Swanson,C. P. Lin, J. S. Schuman, W. G. Stinson, W. Chang, M. R. Hee, T. Flotte, K. Gregory, C. A. Puliafito, and J. G. Fujimoto, "Optical coherence tomography," *Science* **254**, 1178-1181 (1991).
4. B. Bouma, and G. Tearney, (Eds.), "Handbook of Optical Coherence Tomography," *Marcel Dekker* (2002).
5. J. W. Goodman, "Statistical Optics," *John Wiley and Sons* (1985).
6. Y. K. Kim, Y. P. Kim, "High-speed time-domain optical coherence tomography with an imaging speed of ten frames per second with 2000 A-scan," *Optical Engineering* **49**, 055601-6 (2010).
7. A. M. Rollins, M. D. Kulkarni, S. Yazdanfar, R. Ung-arunyawee and J. A. Izatt, "In vivo video rate optical coherence tomography," *Optics Express* **3**, 219-229 (1998).
8. L. An, P. Li, G. Lan, D. Malchow and R. K. Wang, "High-resolution 1050 nm spectral domain retinal optical coherence tomography at 120 kHz A-scan rate with 6.1 mm imaging depth," *Biomed. Opt. Express* **4**, 245-259 (2013).
9. W. Wieser, B. R. Biedermann, T. Klein, C. M. Eigenwillig and R. Huber, "Multi-Megahertz OCT: High quality 3D imaging at 20 million A-scans and 4.5 GVoxels per second," *Opt. Express* **18**, 14685-14704 (2010).
10. B. Potsaid, B. Baumann, D. Huang, S. Barry, A. E. Cable, J. S. Schuman, J. S. Duker, and J. G. Fujimoto, "Ultrahigh speed 1050nm swept source / Fourier domain

OCT retinal and anterior segment imaging at 100,000 to 400,000 axial scans per second," *Opt. Express* **18**, 20029-20048 (2010).

11. L. An, P. Li, T. T. Shen, and R. Wang, "High speed spectral domain optical coherence tomography for retinal imaging at 500,000 A- lines per second," *Biomed. Opt. Express* **2**, 2770-2783 (2011).
12. R. K. Wang and J. B. Elder, "Propylene glycol as a contrasting agent for optical coherence tomography to image gastrointestinal tissues," *Laser. Surg. Med.* **30**, 201–208 (2002).
13. X. Wen et al., "In vivo skin optical clearing by glycerol solutions: mechanism," *J. Biophoton.* **3**, 44–52 (2010).
14. D. Zhu et al., "Imaging dermal blood flow through the intact rat skin with an optical clearing method," *J. Biomed. Optics* **15**, 026008 (2010).
15. R. K. Wang, X. Xu, V. V. Tuchin, and J. B. Elder, "Concurrent enhancement of imaging depth and contrast for optical coherence tomography by hyperosmotic agents," *J. Opt. Soc. Am. B* **18**, 948– 953 (2001).
16. R. Leitgeb, C. K. Hitzenberger, and A. F. Fercher, "Performance of Fourier domain vs. time domain optical coherence tomography," *Opt. Express* **11**, 889-894 (2003).
17. M. A. Choma, M. V. Sarunic, C. Uang, and J. A. Izatt, "Sensitivity advantage of swept source and Fourier domain optical coherence tomography," *Opt. Express* **11**, 2183-2189 (2003).
18. S. H. Yun, G. J. Tearney, B. E. Bouma, B. H. Park, and J. F. de Boer, "High-speed spectral-domain optical coherence tomography at 1.3 μm wavelength," *Opt. Express* **11**, 3598-3604 (2003).
19. R. K. Wang, "In vivo full range complex Fourier domain optical coherence tomography," *Appl. Phys. Letters* **90**, 054103 (2007).

20. S. H. Yun, G. J. Tearney, J. F. de Boer, and B. E. Bouma, "Removing the depth-degeneracy in optical frequency domain imaging with frequency shifting," *Opt. Express* **12**, 4822-1828 (2004).

21. A. H. Bachmann, R. A. Leitgeb, T. Lasser, "Heterodyne Fourier domain optical coherence tomography for full range probing with high axial resolution," *Opt. Express* **14**, 1487-1496 (2006).

22. R. A. Leitgeb, R. Michaely, T. Lasser, and S. Chandra Sekhar, "Complex ambiguity-free Fourier domain optical coherence tomography through transverse scanning," *Opt. Letters* **32**, 3453-3455 (2007).

23. A. G. Podoleanu, "Optical coherence tomography: review," *Brit. J. Radiology* **78**, 976-988 (2005).

24. E. A. Swanson, J. A. Izatt, M. R. Hee, D. Huang, C. P. Lin, J. S. Schuman, C. A. Puliafito and J. G. Fujimoto, "In-vivo retinal imaging by optical coherence tomography," *Opt. Lett.* **18**, 1864–66 (1993).

25. M. R. Hee, C. A. Puliafito, C. Wong, J. S. Duker, E. Reichel, J. S. Schuman, E. A. Swanson, J. G. Fujimoto, "Optical coherence tomography of macular holes," *Ophthalmology* **102**, 748 (1995).

26. A.Tao, J. Wang, Q. Chen, M. Shen, F. Lu, S. R. Dubovy, and M. A. Shousha, "Topographic Thickness of Bowman's Layer Determined by Ultra-High Resolution Spectral Domain–Optical Coherence Tomography," *Investigative Ophthalmology & Visual Science* **52**, 3901-3907 (2011).

27. D. Zhu, M. Shen, H. Jiang, M. Li, M. R. Wang, Y. Wang, L. Ge, J. Qu, and J. Wang, "Broadband superluminescent diode–based ultrahigh resolution optical coherence tomography for ophthalmic imaging," *J. Biomed. Optics* **16**, 126006 (2011).

28. R. A. Leitgeb, W. Drexler, A. Unterhuber, B. Hermann, T. Bajraszewski, T. Le, A. Stingl, and A. F. Fercher, “Ultrahigh resolution Fourier domain optical coherence tomography,” *Opt. Express* **12**, 2156-2165 (2004).

29. Z. Nadler et al, “Automated lamina cribrosa microstructural segmentation in optical coherence tomography scans of healthy and glaucomatous eyes,” *Biomed. Opt. Express* **4**, 2596-2608 (2013).

30. F. Wang, G. Shi, X. Li, J. Lu, Z. Ding, X. Sun, C. Jiang, Y. Zhang, "Comparison of Schlemm's canal's biological parameters in primary open-angle glaucoma and normal human eyes with swept source optical," *J. Biomed. Optics* **17**, 116008-7 (2012).

31. A. Maalej, W. Cheima, K. Asma, R. Riadh, G. Salem, “Optical Coherence Tomography for Diabetic Macular Edema: Early Diagnosis, Classification and Quantitative Assessment,” *J. Clinic. Experiment. Ophthalmol.* **S2**:004 (2012).

32. H. Ishikawa, D. M. Stein, G. Wollstein, S. Beaton, J. G. Fujimoto, and J. S. Schuman, “Macular Segmentation with Optical Coherence Tomography,” *Investigative Ophthalmology & Visual Science* **46**, 2012-2017 (2005).

33. P. L. Hsiung, L. Pantanowitz, A. D. Aguirre et al., “Ultrahigh-resolution and 3-dimensional optical coherence tomography ex vivo imaging of the large and small intestines,” *Gastrointest. Endosc.* **62**, 561 (2005).

34. Y. Chen, A. D. Aguirre, P. L. Hsiung et al., “Ultrahigh resolution optical coherence tomography of Barrett's esophagus: preliminary descriptive clinical study correlating images with histology,” *Endoscopy* **39**, 599 (2007).

35. G. J. Tearney, M. E. Brezinski, J. F. Southern, B. E. Bouma, S. A. Boppart, J. G. Fujimoto, “Optical biopsy in human gastrointestinal tissue using optical coherence tomography,” *Am. J. Gastroenterol.* **92**, 1800-4 (1997).

36. T. H. Tsai, J. G. Fujimoto and H. Mashimo, “Endoscopic Optical Coherence Tomography for Clinical Gastroenterology,” *Diagnostics* **4**, 57-93 (2014).

37. Z. Yaqoob, J. Wu, E. J. McDowell, X. Heng, C. Yang, “Methods and application areas of endoscopic optical coherence tomography,” *J. Biomed. Optics* **11**, 063001 (2006).

38. G. J. Tearney, M. Brezinski, B. Bouma, S. Boppart, C. Pitris, J. Southern and J. G. Fujimoto, “In vivo endoscopic optical biopsy with optical coherence tomography,” *Science* **276**, 2037–39 (1997).

39. C. K. Lee, T. T. Chi, C. T. Wu, M. T. Tsai, C. P. Chiang, and C. C. Yang, “Diagnosis of oral precancer with optical coherence tomography,” *Biomed. Opt. Express* **3**, 1632-1646 (2012).

40. M. T. Tsai, H. C. Lee, C. K. Lee, C. H. Yu, H. M. Chen, C. P. Chiang, C. C. Chang, Y. M. Wang, and C. C. Yang, “Effective indicators for diagnosis of oral cancer using optical coherence tomography,” *Opt. Express* **16**, 15847-15862 (2008).

41. Q. Tang, J. Wang, A. Frank et al., “Depth-resolved imaging of colon tumor using optical coherence tomography and fluorescence laminar optical tomography,” *Biomed. Opt. Express* **7**, 5218-5232 (2016).

42. X. Yao, Y. Gan, E. Chang, H. Hibshoosh, S. Feldman, and C. Hendon, “Visualization and Tissue Classification of Human Breast Cancer Images Using Ultrahigh-Resolution OCT,” *Lasers Surg. Med.* **49**, 258-269 (2017).

43. W. Gao, V. P. Zakharov, O. O. Myakinin, I. A. Bratchenko, D. N. Artemyev and D. V. Kornilin, “Medical images classification for skin cancer using quantitative image features with optical coherence tomography,” *Journal of Innovative Optical Health Sciences* **9**, 1650003 (2016).

44. M. Mogensen, L. Thrane, T. M. Jørgensen, P. E. Andersen, and G. B. E. Jemec, "OCT imaging of skin cancer and other dermatological diseases," *J. Biophoton.* **2**, 442-451 (2009).

45. L. P. Hariri, G. T. Bonnema, K. Schmidt, A. M. Winkler, V. Korde, K. D. Hatch, J. R. Davis, M. A. Brewer, J. K. Barton, "Laparoscopic optical coherence tomography imaging of human ovarian cancer," *Gynecologic Oncology* **114**, 188–194 (2009).

46. P. Motreff, S. Levesque, G. Souteyrand, L. Sarry, L. Ouchchane, B. Citron, J. Cassagnes, J. R. Lusson, "High-resolution coronary imaging by optical coherence tomography: Feasibility, pitfalls and artefact analysis," *Archives of Cardiovascular Disease* **103**, 215-226 (2010).

47. M. R. Movahed, V. Ram, R. Arsanjani, "Optimal visualization of five different stent layers during and after percutaneous coronary intervention for recurrent in-stent restenosis using optical coherence tomography (OCT)," *Cardiovascular Revascularization Medicine* **13**, 292-294 (2012).

48. S. D. Giattina et al, "Assessment of coronary plaque collagen with polarization sensitive optical coherence tomography (PS-OCT)," *International Journal of Cardiology* **107**, 400-409 (2006).

49. Y. Natsume, S. Nakashima, A. Sadr, Y. Shimada, J. Tagami, and Y. Sumi, "Estimation of lesion progress in artificial root caries by swept source optical coherence tomography in comparison to transverse microradiography," *J. Biomed. Optics* **16**, 071408 (2011).

50. Y. Shimada, A. Sadr, A. Nazari, H. Nakagawa, M. Otsuki, J. Tagami and Y. Sumi, "3D evaluation of composite resin restoration at practical training using swept-source optical coherence tomography (SS-OCT)," *Dental Materials Journal* **31**, 409–417 (2012).

51. D. P. Popescu, M. G. Sowa, M. D. Hewko, L. P. C. Smith, "Assessment of early demineralization in teeth using the signal attenuation in optical coherence tomography images," *J. Biomed. Optics* **13**, 054053 (2008).

52. L. S. A. de Melo et al, "Evaluation of enamel dental restoration interface by optical coherence tomography," *J. Biomed. Optics* **10**, 064027 (2005).

53. M. M. Mandurah, A. Sadr, T. A. Bakhsh, Y. Shimada, Y. Sumi, J. Tagami, "Characterization of transparent dentin in attrited teeth using optical coherence tomography ," *Lasers Med. Sci.* **30**, 1189–1196 (2015).

54. S. K. Debnath, M. P. Kothiyal, J. Schmit, and P. Hariharan, "Spectrally resolved phase-shifting interferometry of transparent thin films: sensitivity of thickness measurements," *Applied Optics* **45**, 8636-8640 (2006).

55. Y. Zhao, G. Schmidt, D. T. Moore, and J. D. Ellis, "Absolute thickness metrology with submicrometer accuracy using a low-coherence distance measuring interferometer," *Applied Optics* **54**, 7693-7700 (2015).

56. C. Koshimizu, T. Ohta, T. Matsudo, S. Tsuchitani, and M. Ito, "Simultaneous In situ Measurement of Silicon Substrate Temperature and Silicon Dioxide Film Thickness during Plasma Etching of Silicon Dioxide Using Low-Coherence Interferometry," *Japanese Journal of Applied Physics* **51**, 046201 (2012).

57. H. Maruyama, S. Inoue, T. Mitsuyama, M. Ohmi, and M. Haruna, "Low-coherence interferometer system for the simultaneous measurement of refractive index and thickness," *Applied Optics* **41**, 1315-1322 (2002).

58. A. Khomenko, G. L. Cloud, and M. Haq, "Application of low-coherence interferometry for in situ nondestructive evaluation of thin and thick multilayered transparent composites," *Optical Engineering* **54**, 125103 (2015).

59. D. Stifter, K. Wiesauer, M. Wurm, E. Schlotthauer, J. Kastner, M. Pircher, E. Gotzinger and C. K. Hitzenberger, "Investigation of polymer and polymer/fibre

composite materials with ptical coherence tomography," *Meas. Sci. Technol.* **19**, 074011 (2008).

60. J. P. Dunkers, R. S. Parnas, C. G. Zimba, R. C. Peterson, K. M. Flynn, J. G. Fujimoto, B. E. Bouma, "Optical coherence tomography of glass reinforced polymer composites," *Composites: Part A* **30**, 139–145 (1999).

61. F. Xu, H. E. Pudavar, P. N. Prasad, D. Dickensheets, "Confocal enhanced optical coherence tomography for nondestructive evaluation of paints and coatings," *Optics Letters* **24**, 1808-1810 (1999).

62. P. Antoniuk, M. R. Strąkowski, J. Pluciński, B. B. Kosmowski, "Non-destructive inspection of anti-corrosion protective coatings using optical coherent tomography," *Metrology and Measurement Systems* **XIX**, 365-372 (2012).

63. Y. Dong, S. Lawman, Y. Zheng, D. Williams, J. Zhang, Y. Shen, "Nondestructive analysis of automotive paints with spectral domain optical coherence tomography," *Applied Optics* **55**, 3695-3700 (2016).

64. C. S. Cheung, M. Spring, and H. Liang, "Ultra-high resolution Fourier domain optical coherence tomography for old master paintings," *Opt. Express* **23**, 10145-10157 (2015).

65. B. Baumann, "Polarization Sensitive Optical Coherence Tomography: A Review of Technology and Applications," *Appl. Sci.* **7**, 474 (2017).

66. C. K. Hitzenberger, E. Gotzinger, M. Sticker, M. Pircher, and A. F. Fercher, ''Measurement and imaging of birefringence and optic axis orientation by phase resolved polarization sensitive optical coherence tomography,'' *Opt. Exp.* **9**, 780–790 (2001).

67. C. E. Saxer, J. F. de Boer, B. H. Park, Y. Zhao, Z. Chen and J. S. Nelson, "High-speed fiber–based polarization-sensitive optical coherence tomography of in vivo human skin," *Optics Letters* **25**, 1355-1357 (2000).

68. M. Yamanari, S. Makita, V. D. Madjarova, T. Yatagai, and Y. Yasuno, "Fiber-based polarization-sensitive Fourier domain optical coherence tomography using B-scan-oriented polarization modulation method," *Opt. Express* **14**, 6502–6515 (2006).

69. E. Gotzinger, B. Baumann, M. Pircher, C. K. Hitzenberger, "Polarization maintaining fiber based ultra-high resolution spectral domain polarization sensitive optical coherence tomography," *Opt. Express* **17**, 22704-22717 (2009).

70. B. Baumann, E. Götzinger, M. Pircher, C. K. Hitzenberger, "Single camera based spectral domain polarization sensitive optical coherence tomography," *Opt. Express* **15**, 1054-1063 (2007).

71. M. Yamanari, S. Makita, and Y. Yasuno, "Polarization-sensitive swept-source optical coherence tomography with continuous source polarization modulation," *Opt. Express* **16**, 5892–5906 (2008).

72. Z. Lu, D. K. Kasaragod, and S. J. Matcher, "Method to calibrate phase fluctuation in polarization-sensitive swept-source optical coherence tomography," *J. Biomed. Optics* **16**, 070502 (2011).

73. D. P. Davé, T. Akkin, and T. E. Milner, "Polarization-maintaining fiber-based optical low-coherence reflectometer for characterization and ranging of birefringence," *Opt. Lett.* **28**, 1775-77 (2003).

74. M. K. Al-Qaisi and T. Akkin, "Swept-source polarization-sensitive optical coherence tomography based on polarization-maintaining fiber," *Optics Express* **18**, 3392-3403 (2010).

75. B. H. Park, C. Saxer, S. M. Srinivas, J. S. Nelson, J. F. de Boer, "In vivo burn depth determination by high-speed fiber-based polarization sensitive optical coherence tomography," *J. Biomed. Optics* **6**, 474-479 (2001).

76. J. T. Oh, S. W. Lee, Y. S. Kim, K. B. Suhr, and B. M. Kim, "Quantification of the wound healing using polarization-sensitive optical coherence tomography," *J. Biomed. Optics* **11**, 041124 (2006).

77. J. Strasswimmer, Mark C. Pierce, B. Hyle Park, Victor Neel, Johannes F. de Boer, "Polarization-sensitive optical coherence tomography of invasive basal cell carcinoma," *J. Biomed. Optics* **9**, 292 (2004).

78. H. M. Subhash, "Biophotonics Modalities for High-Resolution Imaging of Microcirculatory Tissue Beds Using Endogenous Contrast: A Review on Present Scenario and Prospects," *International Journal of Optics* 1-20 (2011).

79. Z. Chen, T. E. Milner, D. Dave, and J. S. Nelson, "Optical Doppler tomographic imaging of fluid flow velocity in highly scattering media," *Optics Letters* **22**, 64–66 (1997).

80. J. A. Izatt, M. D. Kulkarni, S. Yazdanfar, J. K. Barton, and A. J. Welch, "In vivo bidirectional color Doppler flow imaging of picoliter blood volumes using optical coherence tomography," *Optics Letters* **22**, 1439–1441 (1997).

81. R. A. Leitgeb, L. Schmetterer, C. K. Hitzenberger et al., "Real-time measurement of in vitro flow by Fourier-domain color Doppler optical coherence tomography," *Optics Letters* **29**, 171-173 (2004).

82. Z. Chen, T. E. Milner, S. Srinivas, X. Wang, A. Malekafzali, M. J. C. van Gemert, and J. S. Nelson, "Noninvasive imaging of in vivo blood flow velocity using optical Doppler tomography," *Opt. Lett.* **22**, 1119-1121 (1997).

83. Y. Zhao, Z. Chen, C. Saxer, S. Xiang, J. F. de Boer, and J. S. Nelson, "Phase-resolved optical coherence tomography and optical Doppler tomography for imaging blood flow in human skin with fast scanning speed and high velocity sensitivity," *Opt. Lett.* **25**, 114-116 (2000).

84. S. Xia, Y. Huang, S. Peng, Y. Wu, X. Tan, "Robust phase unwrapping for phase images in Fourier domain Doppler optical coherence tomography," *J. Biomed. Optics* **22**, 036014 (2017).

85. H. C. Hendargo, M. Zhao, N. Shepherd and J. A. Izatt, "Synthetic wavelength based phase unwrapping in spectral domain optical coherence tomography," *Opt. Exp.* **17**, 5039-5051 (2009).

86. V. J. Srinivasan, S. Sakadzic, I. Gorczynska, S. Ruvinskaya, W. Wu, J. G. Fujimoto, and D. A. Boas, "Quantitative cerebral blood flow with Optical Coherence Tomography," *Optics Express* **18**, 2477-2494 (2010).

87. O. Sakurada, C. Kennedy, J. Jehle, J. D. Brown, G. L. Carbin, and L. Sokoloff, "Measurement of local cerebral blood flow with iodo [14C] antipyrine," *Am. J. Physiol.* **234**, H59–H66 (1978).

88. Y. Zhao, Z. Chen, C. Saxer, Q. Shen, S.a Xiang, J. F. de Boer, and J. S. Nelson, "Doppler standard deviation imaging for clinical monitoring of in vivo human skin blood flow," *Opt. Lett.* **25**, 1358-1360 (2000).

89. Z. Zhi, W. Cepurna, E. Johnson, T. Shen, J. Morrison, and R. K. Wang, "Volumetric and quantitative imaging of retinal blood flow in rats with optical microangiography," *Biomed. Opt. Exp.* **2**, 579-591 (2011).

90. C. Yang, "Molecular Contrast Optical Coherence Tomography: A Review," *Photochem Photobiol*. **81**, 215–237 (2005).

91. K. D. Rao, M. A. Choma, S. Yazdanfar, A. M. Rollins, J. A. Izatt, "Molecular contrast in optical coherence tomography by use of a pump–probe technique," *Opt. Lett.* **28**, 340-342 (2003).

92. J. M. T. Schwartz, T. A. Meyer, C. A. Patil, C. L. Duvall, and M. C. Skala, "In vivo photothermal optical coherence tomography of gold nanorod contrast agents," *Biomed. Opt. Exp*. **3**, 2881-2895 (2012).

93. U. Morgner, W. Drexler, F. X. Kartner, X. D. Li, C. Pitris, E. P. Ippen, and J. G. Fujimoto, "Spectroscopic optical coherence tomography," *Opt. Lett.* **25**, 111-113 (2000).

94. Y. Jiang, I. V. Tomov, Y. Wang, and Z. Chen, "High-resolution second-harmonic optical coherence tomography of collagen in rat-tail tendon," *Appl. Phys. Lett.* **86**, 133901 (2005).

95. C. Xu, J. Ye, D. Marks, S. Boppart, "Near-infrared dyes as contrast-enhancing agents for spectroscopic optical coherence tomography," *Optics Letters* **29**, 1647 (2004).

96. B. H. Park, M. C. Pierce, B. Cense, S. H. Yun, M. Mujat, G. J. Tearney, B. E. Bouma, J. F. de Boer, "Real-time fiber-based multi-functional spectral domain optical coherence tomography at 1.3 μm, " *Opt. Exp.* **13**, 3931-3944 (2005).

97. B. Cense, M. Mujat, T. C. Chen, B. H. Park, J. F. de Boer, "Polarization-sensitive spectral-domain optical coherence tomography using a single line scan camera," *Opt. Express* **15**, 2421-2431 (2007).

98. H. Wang, M. K. Al-Qaisi, T. Akkin, "Polarization-maintaining fiber based polarization-sensitive optical coherence tomography in spectral domain," *Opt. Lett.* 35, 154-156 (2010).

99. C. Fan, Y. Wang and R. K. Wang, "Spectral domain polarization sensitive optical coherence tomography achieved by single camera detection," Opt. Express **15**, 7950-7961 (2007).

100. R. K. Wang, C. Fan, "Method and apparatus for localized polarization sensitive imaging," *US Patent* **US 2010/0182609 A1** (2010).

101. Z. Wang, Z. Yuan, H. Wang, and Y. Pan, "Increasing the imaging depth of spectral-domain OCT by using interpixel shift technique," *Opt. Express* **14**, 7014- 7023 (2006).

102. M. Zhao and J. A. Izatt, "Single-camera sequential-scan-based polarization-sensitive SDOCT for retinal imaging," *Opt. Lett.* **34**, 205-207 (2009).

103. S. Moon, S. W. Lee, Z. Chen, "Reference spectrum extraction and fixed-pattern noise removal in optical coherence tomography," *Opt. Express* **18**, 24395–24404 (2010).

104. B. Hofer, B. Povazay, B. Hermann, S. .M. Rey, V. Kajic, A. Tumlinson, K. Powell, G. Matz, W. Drexler, "Artefact reduction for cell migration visualization using spectral domain optical coherence tomography," *Journal of Biophotonics* **4**, 355–367 (2011).

105. Y. Yasuno, Y. Hong, S. Makita, M. Yamanari, M. Akiba, M. Miura, T. Yatagai, "In vivo high-contrast imaging of deep posterior eye by 1-μm swept source optical coherence tomography and scattering optical coherence angiography," *Opt. Express* **15**, 6121–6139 (2007).

106. P. K. Gupta, H. S. Patel, S. Ahlawat, "Light based techniques for improving health care: studies at RRCAT," *Proc. Natl. Acad. Sci. India Sect. A Phys. Sci.* **85**, 489 (2015).

107. L. An, R. K. Wang, "Use of a scanner to modulate spatial interferograms for in vivo full-range Fourier-domain optical coherence tomography," *Opt. Lett.* **32**, 3423–3425 (2007).

108. B. Gupta, A. Ariyawardana, N. W. Johnson, "Oral cancer in India continues in epidemic proportions: evidence base and policy initiatives," *Int. Dent. J.* **63**, 12–25 (2013).

109. O. K. Adegun, P. .H. Tomlins, E. Hagi-Pavli, G. McKenzie, K. Piper, D. L. Bader, F. Fortune, "Quantitative analysis of optical coherence tomography and histopathology images of normal and dysplastic oral mucosal tissues," *Lasers Med. Sci.* **27**, 795–804 (2012).

110. R. Wessels, D. M. De Bruin, D. J. Faber, T. G. Van Leeuwen, M. V. Beurden, T. J. Ruers, "Optical biopsy of epithelial cancers by optical coherence tomography (OCT)," *Lasers Med .Sci.* **29**, 1297–305 (2014).

111. K. Sokolov, R. Drezek, K. Gossage, R. R. Kortum, "Reflectance spectroscopy with polarized light: is it sensitive to cellular and nuclear morphology," *Opt. Express* **5**, 302–317 (1999).

112. J. Chung, W. Jung, M. J. Hammer-Wilson, P. W. Smith, Z. Chen, "Use of polar decomposition for the diagnosis of oral precancer," *Appl. Opt.* **46**, 3038–3045 (2007).

113. S. Manhas, M. K. Swami, H. S. Patel, A. Uppal, N. Ghosh, P. K. Gupta, "Polarized diffuse reflectance measurements on cancerous and noncancerous tissues," *J. Biophoton.* **2**, 581-587 (2009).

114. Y. Yoon, W. H. Jang, P. Xiao, B. Kim, T. Wang, Q. Li, J. .Y. Lee, E. Chung, K. H. Kim, "In vivo wide-field reflectance/fluorescence imaging and polarization-sensitive optical coherence tomography of human oral cavity with a forward-viewing probe," *Biomed. Opt. Express* **6**, 524-35 (2015).

115. A. M. Lee, L. Cahill, K. Liu, C. MacAulay, C. Poh, P. Lane, "Wide-field in vivo oral OCT imaging," *Biomed. Opt. Express* **6**, 2664–2674 (2015).

116. Y. Verma, M. Gautam, K. D. Rao, M. K. Swami, P. K. Gupta, "Imaging of human breast tissue using polarization sensitive optical coherence tomography," *Laser Physics* **21**, 2143–2148 (2011).

117. F. A. South, E. J. Chaney, M. Marjanovic, S. G. Adie, S. A. Boppart, "Differentiation of ex vivo human breast tissue using polarization sensitive optical coherence tomography," *Biomed. Opt. Express* **5**, 3417–3426 (2014).

118. Y. Yang, T. Wang, X. Wang, M. Sanders, M. Brewer, Q. Zhu, "Quantitative analysis of estimated scattering coefficient and phase retardation for ovarian tissue characterization," *Biomed. Opt. Express* **3**, 1548–1556 (2012).

119. F. Fahimipour, B. Houshmand, P. Alemi, M. Asnaashari, M. A. Tafti, F. Akhoundikharanagh et al, "The effect of He-Ne and Ga-AlAs lasers on the healing of oral mucosa in diabetic mice," *J. Photochem. Photobiol. B* **159**, 149–154 (2016).

120. M. T. Tsai, H. C. Lee, C. W. Lu, Y. M. Wang, C. K. Lee, C. C. Yang, C. P. Chiang, "Delineation of an oral cancer lesion with swept-source optical coherence tomography," *J. Biomed. Optics* **13**, 044012 (2008).

121. P. Friedl, K. Wolf, "Tumour-cell invasion and migration: diversity and escape mechanisms," *Nat. Rev. Cancer* **3**, 362–374 (2003).

122. C. K. Lee, M. T. Tsai, H. C. Lee, H. M. Chen, C. P. Chiang, Y. M. Wang, C. C. Yang, "Diagnosis of oral submucous fibrosis with optical coherence tomography," *J. Biomed. Optics* **14**, 054008 (2009).

123. P. P. Provenzano, K. W. Eliceiri, J. M. Campbell, D. R. Inman, J. G. White, P. J. Keely, "Collagen reorganization at the tumor-stromal interface facilitates local invasion," *BMC Med* **4**, 38 (2006).

124. T. Sekiguchi, M. Noguchi, K. Nakamori, G. Kohama, "Clinical significance of interstitial collagen deposition at the invading edge in oral cancer: Immunohistochemistry for type I collagen," *Int. J. Clin. Oncol.* **2**, 21–28 (1997).

125. Y.C. Ahn, W. Jung, Z. Chen, "Quantification of a three-dimensional velocity vector using spectral-domain Doppler optical coherence tomography," *Opt. Lett.* **32**, 1587 (2007).

126. C. Blatter, S. Coquoz, B. Grajciar, A.S.G. Singh, M. Bonesi, R.M. Werkmeister, L. Schmetterer, R.A. Leitgeb, "Dove prism based rotating dual beam bidirectional Doppler OCT ," *Biomed. Opt. Exp.* **4**, 1188 (2013).

127. C.J. Pedersen, D. Huang, M.A. Shure, A.M. Rollins, “Measurement of absolute flow velocity vector using dual-angle, delay-encoded Doppler optical coherence tomography,” *Opt. Lett.* **32**, 506 (2007).

128. H.M. Subhash, N. Choudhury, F. Chen, R.K. Wang, S.L. Jacques, A.L. Nuttall, “Depth-resolved dual-beamlet vibrometry based on Fourier domain low coherence interferometry,” *J. Biomed. Optics* **18**, 036003 (2013).

129. M. A. Choma, A. K. Ellerbee, C. Yang, T. L. Creazzo, J. A. Izatt, “Spectral-domain phase microscopy,” *Opt. Lett.* **30**, 1162 (2005).

130. N. V. Iftimia, D. X. Hammer, R. D. Ferguson, M. Mujat, D. Vu, A. A. Ferrante, “Dual-beam Fourier domain optical Doppler tomography of zebrafish,” *Opt. Express* **16**, 13624 (2008).

131. R. M. Werkmeister, N. Dragostinoff, M. Pircher, E. Gotzinger, C. K. Hitzenberger, R. A. Leitgeb, L. Schmetterer, “Bidirectional Doppler Fourier-domain optical coherence tomography for measurement of absolute flow velocities in human retinal vessels,” *Opt. Lett.* **33**, 2967–2969 (2008).

132. D. P. Dave, T. E. Milner, “Doppler-angle measurement in highly scattering media,” *Opt. Lett.* **25**, 1523–1525 (2000).

133. Y. Wang, B. A. Bower, J. A. Izatt, O. Tan, D. Huang, “In vivo total retinal blood flow measurement by Fourier domain Doppler optical coherence tomography,” *J. Biomed. Optics* **12**, 041215 (2007).

134. I. Grulkowski, J. J. Liu, B. Potsaid, V. Jayaraman, C. D. Lu, J. Jiang, A. E. Cable, J. S. Duker, J. G. Fujimoto, “Retinal, anterior segment and full eye imaging using ultrahigh speed swept source OCT with vertical-cavity surface emitting lasers,” *Biomed. Opt. Express* **3**, 2733–2751 (2012).

135. W. Trasischker, R. M. Werkmeister, S. Zotter, B. Baumann, T. Torzicky, M. Pircher, C. K. Hitzenberger, “In vitro and in vivo three-dimensional velocity vector

measurement by three-beam spectral-domain Doppler optical coherence tomography," *J. Biomed. Optics* **18**, 116010 (2013).

136. Y. Verma, P. Nandi, K. D. Rao, M. Sharma, P. K. Gupta, "Use of common path phase sensitive spectral domain optical coherence tomography for refractive index measurements," *App. Opt.* **50**, E7 (2011).
137. S. Kumar, Y. Verma, P. Sharma, R. Shrimali, P. K. Gupta, "Single detector-based absolute velocity measurement using spectral domain Doppler optical coherence tomography," *Appl. Phys. B* **117**, 395 (2014).
138. M. J.C. Machado, M. G. Watson, A. H. Devlin, M. A. J. Chaplain, S. R. Mcdougall and C. A. Mitchell, "Dynamics of angiogenesis during wound healing: a coupled in vivo and in silico study," *Microcirculation* **18**, 183–97 (2011).
139. B. J. Vakoc, S. H. Yun, J. F. de Boer, G. J. Tearney and B. E. Bouma, "Phase-resolved optical frequency domain imaging," *Opt. Express* **13**, 5483-93 (2005).
140. J. Lee, V. Srinivasan, H. Radhakrishnan and D. A. Boas, "Motion correction for phase-resolved dynamic optical coherence tomography imaging of rodent cerebral cortex," *Opt. Express* **19**, 21258–70 (2011).
141. A. Yen and I. M. Braverman, "Ultrastructure of the human dermal microcirculation:the horizontal plexus of the papillary dermis," *J. Invest. Dermatol.* **66**, 131–42 (1976).
142. J. Enfield, E. Jonathan, and M. Leahy, "In vivo imaging of the microcirculation of the volar forearm using correlation mapping optical coherence tomography (cmOCT)," *Biomed. Opt. Express* **2**, 1184-1193 (2011).
143. A. Mariampillai et al, "Speckle variance detection of microvasculature using swept-source optical coherence Tomography," *Opt. Letters* **33**, 1530-1532 (2008).
144. M. S. Mahmud, D. W. Cadotte, B. Vuong, C. Sun, T. W. H. Luk, A. Mariampillai, and V. X. D. Yang, "Review of speckle and phase variance optical coherence

tomography to visualize microvascular networks," *J. Biomed. Optics* **18**, 050901-13 (2013).

145. K. M. Poole, D. R. McCormack, C. A. Patil, C. L. Duvall and M. C. Skala, "Quantifying the vascular response to ischemia with speckle variance optical coherence tomography," *Biomed. Opt. Express* **5**, 4118–30 (2014).
146. K. M. Poole, J. M. Tucker-Schwartz, W. W. Sit, A. J. Walsh, C. L. Duvall and M. C. Skala, "Quantitative optical imaging of vascular response in vivo in a model of peripheral arterial disease," *Am. J. Physiol. Heart Circ. Physiol.* **305**, H1168–80 (2013).
147. Y. Jung, S. Dziennis, Z. Zhi, R. Reif, Y. Zheng, R. K. Wang, "Tracking Dynamic Microvascular Changes during Healing after Complete Biopsy Punch on the Mouse Pinna Using Optical Microangiography," *PLoS ONE* **8**, e57976 (2013).
148. S. Yousefi, J. Qin, S. Dziennis, and R. K. Wang, "Assessment of microcirculation dynamics during cutaneous wound healing phases in vivo using optical microangiography," *J. Biomed. Optics* **19**, 076015 (2014).
149. K. Sahu, M. Sharma, A. Dube and P. K. Gupta, "Topical antimicrobial photodynamic therapy improves angiogenesis in wounds of diabetic mice," *Lasers Med. Sci.* **30**, 1923 (2015).
150. P. Sharma, K. Sahu, P. K. Kushwaha, S. Kumar, M. K. Swami, J. Kumawat, H. S. Patel, S. Kher, P. K. Sahani, G. Haridas, P. K. Gupta, "Noninvasive assessment of cutaneous alterations in mice exposed to whole body gamma irradiation using optical imaging techniques," *Lasers Med. Sci.* **32**, 1535 (2017).
151. J. Fitzgerald, C. Rich, D. Burkhardt, J. Allen, A. S. Herzka and C. B. Little, "Evidence for articular cartilage regeneration in MRL/MpJ mice," *Osteoarthr. Cartil.* **16**, 1319 (2008).

152. D. M. Santos, A. M. Rita, I. Casanellas, A. B. Ova, I. M. Araujo, D. Power and G. Tiscornia, “Ear wound regeneration in the African spiny mouse acomys cahirinus,” *Regeneration* **3**, 52 (2016).

153. D. M. Jr Catarious, A. H. Baydush and C. E. Jr Floyd, “Characterization of difference of Gaussian filters in the detection of mammographic regions,” *Med. Phys.* **33**, 4104–14 (2006).

154. T. G. Levitskaia, S. A. Bryan, J. A. Creim, T. L. Curry, T. Luders, K. D. Thrall, J. M. Peterson, “Optical spectroscopy and multivariate analysis for biodosimetry and monitoring of radiation injury to the skin,” *Drug. Dev. Res.* **73**, 252–273 (2012).

155. E. C. Halperin, C. A. Perez, L. W. Brady, D. E. Wazer, “Perez and Brady’s principles and practice of radiation oncology,” *Lippincott Williams & Wilkins*, Philadelphia (2007).

156. J. L. Ryan, “Ionizing radiation: the good, the bad, and the ugly,” *J. Investig. Dermatol.* **132**, 985–993 (2012).

157. W. H. Jang, S. Shim, T. Wang, Y. Yoon, W. Jang, J. K. Myung, S. Park, K. H. Kim, “In vivo characterization of early-stage radiation skin injury in a mouse model by two-photon microscopy,” *Sci. Rep.* **6**, 19216 (2016).

158. E. Balli, U. Comelekoglu, E. Yalin, N. Yilmaz, S. Aslantas, F. Sogut, M. Berkoz, S. Yalin, “Exposure to gamma rays induces early alterations in skin in rodents: mechanical, biochemical and structural responses,” *Ecotoxicol. Environ. Saf.* **72**, 889–894 (2009).

159. M. Tzaphlidou, E. Kounadi, I. Leontiou, D. P. Matthopoulos, D. Glaros, “ Influence of low doses of gamma-irradiation on mouse skin collagen fibrils,” *Int. J. Radiat. Biol.* **71**, 109–115 (1997).

160. P. Sharma, Y. Verma, K. Sahu, S. Kumar, A. V. Varma, J. Kumawat, P. K. Gupta, "Human ex-vivo oral tissue imaging using spectral domain polarization sensitive optical coherence tomography," *Lasers Med. Sci.* **32**, 143-150 (2017).

161. K. Sahu, M. Sharma, P. Sharma, Y. Verma, K. D. Rao, H. Bansal, A. Dube, P. K. Gupta, "Effect of poly-L-lysine-chlorin P6-mediated antimicrobial photodynamic treatment on collagen restoration in bacteria-infected wounds," *Photomed. Laser Surg.* **32**, 23-29 (2014).

162. A. Maslennikova, M. Kochueva, N. Ignatieva, A. Vitkin, O. Zakharkina, V. Kamensky, E. Sergeeva, E. Kiseleva, V. Bagratashvili, "Effects of gamma irradiation on collagen damage and remodeling," *Int. J. Radiat. Biol.* **91**, 240 (2015).

163. S. V. Galvan, E. F. Lizarbe, M. Truchuelo, B. D. Ley, E. Grillo, V. Sanchez, L. R. Buceta, J. Paoli, S. Sancho, A. Montero, R. Hernanz, A. Ramos, P. Jaen and S. Gonzalez, "Dynamic skin changes of acute radiation dermatitis revealed by in vivo reflectance confocal microscopy," *Journal of the European Academy of Dermatology and Venereology* **27**, 1143-1150 (2013).

164. O. Goertz, C. Poettgen, A. Akbari, J. Kolbenschlag, S. Langer, M. Lehnhardt, M. Stuschke, L. von der Lohe, "New model for long-term investigations of cutaneous microcirculatory and inflammatory changes following irradiation," *J. Radiat. Res.* **56**, 456-461 (2015).

165. L. Chin, E. Korpela, A. Kim, D. Yohan, C. Niu, B. C. Wilson, S. K. Liu, "Diffuse optical spectroscopy for the quantitative assessment of acute ionizing radiation induced skin toxicity using a mouse model," *J. Vis. Exp.* **111**, 1–8 (2016).

166. M. S. Chin, B. B. Freniere, Y. C. Lo, J. H. Saleeby, S. P. Baker, H. M. Strom, R. A. Ignotz, J. F. Lalikos, T. J. Fitzgerald, "Hyperspectral imaging for early detection of oxygenation and perfusion changes in irradiated skin," *J. Biomed. Optics* **17**, 026010 (2012).

167. V. D. Thanik, C. C. Chang, R. A. Zoumalan, O. Z. Lerman, R. J. Jr Allen, P. D. Nguyen, S. M. Warren, S. R. Coleman, A. Hazen, "A novel mouse model of cutaneous radiation injury," *Plast. Reconstr. Surg.* **127**, 560–568 (2011).

168. I. S. Vala et al, "Low doses of ionizing radiation promote tumor growth and metastasis by enhancing angiogenesis," *PLoS ONE* **5**, e11222 (2010).

169. V. Nunia, G. Sancheti, P. K. Goyal, "Protection of Swiss albino mice against whole-body gamma irradiation by diltiazem," *Br. J. Radiol.* **80**, 77–84 (2007).

170. G. C. Jagetia, M. S. Baliga, K. J. Malagi, M. S. Kamath, "The evaluation of the radioprotective effect of Triphala (an ayurvedic rejuvenating drug) in the mice exposed to gamma-radiation," *Phytomedicine* **9**, 99–108 (2002).

171. K. Randall, J. E. Coggle, "Expression of transforming growth factor-β1 in mouse skin during the acute phase of radiation damage," *Int. J. Radiat. Biol.* **68**, 301 (1995).

172. J. P. Williams, W. H. McBride, "After the bomb drops: a new look at radiation-induced multiple organ dysfunction syndrome (MODS)," *Int. J. Radiat. Biol.* **87**, 851–868 (2011).

173. R. Ameziane-El-Hassani, M. Talbot, M. C. de Souza Dos Santos, A. A. Ghuzlan, D. Hartl, J. M. Bidart, X. D. Deken, F. Miot, I. Diallo, F. de Vathaire, M. Schlumberger, C. Dupuy, "NADPH oxidase DUOX1 promotes long-term persistence of oxidative stress after an exposure to irradiation," *Proc. Natl. Acad. Sci. U S A* **112**, 5051–5056 (2015).

174. E. Bey et al, " Emerging therapy for improving wound repair of severe radiation burns using local bone marrow-derived stem cell administrations," *Wound Repair Regen.* **18**, 50-58 (2010).

175. J. J. Lataillade et al, “New approach to radiation burn treatment by dosimetry-guided surgery combined with autologous mesenchymal stem cell therapy,” *Regen. Med.* **2**, 785–794 (2007).

176. M. Benderitter, M. Isoir, V. Buard et al, “Collapse of skin antioxidant status during the subacute period of cutaneous radiation syndrome: a case report,” *Radiat. Res.* **167**, 43–50 (2007).